PHOTOCHEMICAL AIR QUALITY MODELLING IN ARID REGIONS

by

© **Mohammed Mujtaba Shareef**

A thesis submitted to the school of Graduate Studies in partial fulfillment

of the requirements for the degree of

Doctor of Philosophy

Faculty of Engineering and Applied Science

Memorial University of Newfoundland

July 2017

St. John’s, NL, Canada

ABSTRACT

Despite continuous measures to control air pollution, large fractions of the population across the world are still exposed to potentially dangerous pollutant concentration levels. Research continues to increase in the area of air pollution with focus on different pollutants and regions. A particular emphasis is on the understanding of the formation of secondary pollutants as their relationships with primary pollutants are complex. One of the key factors that influences these complex relationships is the regional characteristics, such as temperature, humidity, and solar radiations. Arid regions are of particular concern as the characteristics, especially, extreme temperatures and dust storms, deteriorate air quality significantly. The study area chosen for this research is the Riyadh region in Saudi Arabia. Improving the air quality in this region requires further understanding of the formation of secondary pollutants, particularly ozone (O_3). Generally, Photochemical Air Quality Models (PAQM) are employed to study the formation of secondary pollutants in the atmosphere. This research configured high-resolution Community Multiscale Air Quality (CMAQ) model over the area to study the research objectives. This model could be utilized to study various strategies to mitigate photochemical smog formation in the region.

The regional characteristics have significant roles in atmospheric chemical mechanisms, and an effective mitigation plan is important for successful air quality management; hence getting a better understanding of the chemical mechanisms is pivotal. This thesis investigated various chemical mechanisms that are present in PAQM constraining with the observed data resulting in the identification of the most appropriate mechanism for arid

regions. The key chemical reactions and corresponding kinetics were also ascertained. The identified chemical mechanism will serve as a benchmark for any future implementation of PAQM in Riyadh as well as similar regions.

Conventionally, deterministic PAQMs are applied to evaluate the efficacy of a control strategy to achieve air quality standards. Uncertainties are inherent in any mathematical model, including PAQM, and are specific to regional characteristics. Ignoring model uncertainties might yield a false sense of precision about pollutant response to emission controls. Hence, such uncertainties must be identified and quantified for the selection of control policies. This research identified key factors influencing the O_3 precursor responsiveness and characterized the parametric uncertainties influencing the prediction of O_3 to precursor emissions.

Devising an appropriate mitigation plan also requires running PAQM for a number of scenarios, which is computationally challenging. To overcome this computational burden, an efficient Reduced Form Model (RFM) was developed. It characterizes the impact of uncertainties in model input parameters on O_3 response to not only precursor emissions (NO_x and VOCs) but also to dust emissions.

The development of an efficient RFM allowed the use of a probabilistic framework to study the impact of various emission mitigation and dust increase scenarios. This RFM enabled the understanding of the impact of various emission reductions on the formation of O_3. The newly incorporated dust parameter in the RFM revealed that the relationship of dust concentrations with O_3 formation is nonlinear. Initially, O_3 concentration decreased with the increase of dust and later increased.

The configured PAQM, the identified atmospheric chemical mechanism, and the developed RFM (incorporating the new dust parameter) would facilitate the responsible authorities in devising appropriate O_3 reduction strategies for the study area and similar regions.

The endeavour undertaken in this research to advance the understanding of PAQM in arid conditions opens up several avenues of further research. The developed RFM has a potential to be improved, such as adding more types of uncertainties (structural and meteorological) and further validating with comprehensive observed data. Additionally, the RFM could be integrated with economics and health uncertainty models to study the cost of mitigation plans and health impacts. Moreover, air chambers can be setup to get more insight into chemical kinetics under arid conditions especially the role of heterogeneous reactions of NO_x with dust particles.

ACKNOWLEDGEMENTS

All praise and thanks are to *God Almighty*, the most Gracious, the most Merciful for his blessings and guidance.

I would like to express my special appreciation and gratitude to my supervisor Dr. Tahir Husain for providing me with the opportunity to pursue my PhD. He has been a tremendous mentor for me. I would like to thank him for encouraging my research and allowing me to grow as a research scientist; and his advice on both my research and on my career has been priceless.

I would like to acknowledge Dr. Helen Zhang and Dr. Bing Chen for serving as my committee members. I would like to thank them for their insightful comments and suggestions to my research.

I would like to express my special thanks to Dr. Bader Alharbi from King Abdulaziz City for Science and Technology in Riyadh Saudi Arabia for sharing with me the necessary data and providing expert technical advice on my research.

I would like to acknowledge the Faculty of Engineering and Applied Sciences at Memorial University for providing research scholarships and sessional lectureships during the course of my PhD.

I would also like to acknowledge ACENET, the regional high performance computing consortium for universities in Atlantic Canada, for providing the computing resources, and their efficient technical personnel for providing timely support.

I have been blessed with my wife Masarath and my three children: Zaid, Haniya, and Haroon; whose love, support, and sacrifice made this doctorate possible. Zaid has been patient reviewing with me and challenging the thesis write-up. Haniya has been very caring waking up early with me especially during the weekends making sure I carry my breakfast to the University. The little lovely one, Haroon, would make every effort to stay awake late at night waiting for me to come home to get a good night kiss. I had ups and downs, and my wife was always with me, and I am greatly indebted to her for her understanding and encouragement without which this work would not have been possible. I would also to like thank my brothers and sisters who have been sources of encouragement and support. Finally, I thank all my friends for their company and advices.

TABLE OF CONTENTS

LIST OF TABLES

LIST OF FIGURES

NOMENCLATURE

Abbreviations

BFM	Brute Force Method
CB	Carbon Bond
DDM	Decoupled Direct Method
HDDM	Higher Order Decoupled Direct Method
NAAQS	National Ambient Air Quality Standards
NMB	Normalized Mean Bias
NME	Normalized mean Error
NO_x	$NO + NO_2$
O_3	Ozone
OC	Organic Compound
PAN	Peroxy acetyle nitrates
PAQM	Photochemical Air Quality Model
PM	Particulate Matter (PM_{10} or $PM_{2.5}$)
PM_{10}	Particulate Matter Less Than 10 Microns
$PM_{2.5}$	Particulate Matter Less Than 2.5 Microns
ppb	Parts Per Billion

ppm	Parts Per Million
ppt	Parts Per Trillion
RFM	Reduced Form Model
SOA	Secondary Organic Aerosol
US-EPA	United State Environmental Protection Agency
VOC	Volatile Organic Compound
CB	Carbon Bond
RACM	Regional Atmospheric Chemistry Mechanism
SAPRC	State Air Pollution Research Center
CMAQ	Community Multiscale Air Quality
CMAS	Community Modelling and Analysis System

Symbols

$C_i\,(x,t)$	Concentration of each species at location *x* and time *t*
u_j	j^{th} component of the fluid velocity
D_i	molecular diffusivity of species i the carrier fluid
P_i	rate of production of species i by chemical reaction
D_i	rate of destruction of species i by chemical reaction
E_i	emission rate of species i at location x and time t

$\widetilde{E}_0$	Base value of emission rate targeted for control
$\widetilde{E}_f$	Perturbed emission rate
ε_j	Fractional change in targeted emission rate E
φ_j	Fractional error in input parameter
$S_j^{(1)}$	First order sensitivity coefficient of pollutant concentration
$S_j^{(2)}$	Second order sensitivity coefficient of pollutant concentration
$S_{j,k}$	Cross sensitivities of uncertain parameter
ε_i	Fractional change in NO_x emissions
ω_i	Fractional change in aerosol emissions
$\varphi_{\varepsilon j}$	Fractional error due to emission ε in input parameter
$\varphi_{\omega j}$	Fractional error due to emission ω in input parameter
$S_{\varepsilon j}^{(1)}$	First order sensitivity of pollutant concentration to ε_i
$S_{\varepsilon j}^{(2)}$	Second order sensitivity of pollutant concentration to ε_i
$S_{\omega j}^{(2)}$	Second order sensitivity of pollutant concentration to ω_i

CHAPTER 1: INTRODUCTION

1.1 Background and Motivation

1.1.1 Air Pollution and Photochemical Smog

Air pollution is generally defined as the presence of any substances, solid, liquid, or gas, in the atmosphere in such a concentration that it may tend to be injurious to humans, animals, plants, property, and or the atmosphere itself. The topic of air pollution got worldwide attention after several major historic air pollution episodes such as the London smog of 1952 and later smog events in New York and Los Angeles (Seinfeld and Pandis, 2006). Subsequently, clean air acts in 1970, 1977, and 1980 were enacted by the United States (US) and other countries following the lead of the US. Since then, many studies have focused on investigating the impacts of air pollution on human health and the environment. The adverse effects on human health range from respiratory illnesses such as asthma (Brunekreef and Forsberg, 2005), cardiovascular diseases (Dockery, 2001; Atkinson et al., 2013), and premature mortality and lung cancer (Jerrett et al., 2009; Hart et al., 2011; Lepeule et al., 2012). In addition, air pollution damages crop yields (Grantz et al., 2003; Renaut et al., 2009; Feng and Kobayashi, 2009) and causes reduction in visibility (Malm et al., 1994). Air pollution is also known to affect heat transfer in the atmosphere thereby contributing to climate change (Furuta et al., 2005; Wang et al., 2013). A recent study showed that particulate matter (PM) in the air leads to over 3 million premature deaths each year worldwide predominantly in Asia (Lelieveld et al., 2015).

The U.S. Environmental Protection Agency (US-EPA) established the National Ambient Air Quality Standards (NAAQS) that require development of effective emission control strategies for air pollutants. Despite mitigation measures to control the air quality, a large portion of the population is exposed to potentially dangerous concentration levels (IARC, 2013). The locations that are of particular concern are arid regions where weather conditions, specifically extreme temperatures and dust storms, deteriorate air quality (Alharbi et al., 2015). Improving air quality in such regions requires further understanding on the formation of air pollution.

The formation of secondary air pollutants follows a complex phenomenon, the example of which is the formation of urban smog or photochemical smog, a topic of active research. The term photochemical smog was first used in the 1950s to describe the formation of ground level ozone (O_3) (Seinfeld and Pandis, 2006). The precursors known to form O_3 in the atmosphere are NO_2 and NO (together known as NO_x) and Volatile Organic Compounds (VOCs), thus in order to reduce O_3, these precursors must be controlled (Sillman and He, 2002; Seinfeld and Pandis, 2006). However, due to non-linear relationships with its precursors, the mitigation of O_3 is complex. Strategies to reduce O_3 demand thorough understanding of this complex process, and modelling atmospheric pollutants facilitates this understanding. Establishing the relationships among meteorology, chemical transformations, emissions of chemical species, and removal processes in the context of atmospheric pollutants is the fundamental goal of photochemical air quality modelling (PAQM) (Seinfeld and Pandis, 2006).

1.1.2 Photochemical Smog Chemical Kinetics in Arid Regions

The phenomenon of photochemical smog formation is highly dependent on the chemical transformation in the atmosphere resulting in the formation of secondary pollutants, one of which is O_3. Several chemical mechanisms were developed to understand the issues associated with urban and rural O_3 formation (Tonnesen and Luecken, 2001). A number of studies have compared various mechanisms in PAQM and demonstrated variations in model predictions. Factors such as temperature, urban and rural conditions, VOC/NO_x ratios, and concentrations of precursor pollutants were attributed to these variations (Gross and Stockwell, 2003; Faraji et al., 2008; Luecken et al., 2008).

To the best of the author's knowledge, there is currently limited research that studies the chemical mechanisms in the formation of photochemical smog considering the characteristics of arid regions. Arid regions are generally characterized by high temperatures, humidity, intense UV radiations, and dust storm conditions. These unique characteristics highly alter the chemical mechanisms particularly the kinetic terms. Experimental studies have shown heterogeneous reactions of NO_2 and HNO_2 with oxides and mineral dust, and this loss of NO_2 to dust potentially increases the formation of O_3, particularly in NO_x-limited regions (Underwood et al., 2001). Some studies have observed that O_3 is reduced up to 40% in the presence of Saharan dust (DeReus et al., 2000; Umann et al., 2005; Bonasoni et al., 2004), however, others reported no influence on the O_3 formation due to dust (Fairlie et al., 2010). As indicated, arid regions are prone to frequent dust storms, so excessive buildup of O_3 is expected, and thus, a detailed study in this regard will reveal the unique photochemistry in these regions. Another characteristic that promotes the formation of O_3 is UV radiation (Seinfeld and Pandis, 2006) which is generally higher in arid areas. In addition, scanty rainfall in these regions reduces the dust deposition, thus photochemical pollutants stay in the atmosphere for longer periods of time. This promotes further atmospheric reactions. Studying the chemical kinetics in such regions will provide interesting insight into photochemical smog formation. Table 1.1 summarizes the unique characteristics of these regions that affect the formation of photochemical smog.

Table 1.1 Unique Characteristics of Arid Regions

Factors affecting formation of photochemical smog	**Description**	**Arid region**	**Non-arid region**
Temperature and UV radiation	High values of temperature and UV radiation promotes the photochemical reactions	High	Not so high
Humidity	Humidity is also known to facilitate the reactions	Predominantly hot and humid	No
Dust	Dust interferes the photochemical cycle, thus effecting the formation of photochemical smog	Frequent dust storms	No
Precipitation	Less precipitation enables the pollutants to stay in atmosphere reacting for longer time, while high precipitation scavenges by wet deposition	Scanty	Medium to high

1.1.3 Uncertainty and Response Models

The chemical and physical processes in PAQM introduce significant uncertainties in model predictions, and the complexity of these uncertainties further increases in the formation of secondary pollutants (Lin et al., 1998). These uncertainties are generally characterized by studying the responses to fixed levels of emission changes, called response modelling. Several studies conducted the Monte Carlo analysis for various uncertain parameter settings by sampling parameter values either using random or stratified sampling techniques (Bergin et al., 1999; Moore and Londergan, 2001; Hanna et al., 2001). Since PAQM is computationally intensive, this type of uncertainty analysis particularly for regulatory purpose is not practical and this necessitates the need for developing an appropriate response model.

Sensitivity analysis, which is to assess the impact of perturbation in input parameter on predicted concentrations, has been proved to be a sophisticated and computationally efficient way to predict O_3 responses to flexible amounts of emissions changes (Yang et al., 1997; Cohan et al., 2005). The two most widely used methods of response modelling techniques to probe relationships between concentrations and emissions in photochemical models are the brute-force (BFM) and the decoupled direct method (DDM) (Cohan and Napelenok, 2011). Several studies have developed and validated reduced form models (RFMs) using BFM and DDM techniques considering different kinds of uncertainties. In particular, a study by Pinder et al., (2009) introduced an RFM for O_3 concentration using DDM sensitivity coefficients by jointly considering both parametric and structural uncertainties, and another study (Tian et al., 2010) extended that approach by incorporating emission uncertainty. Yet another study (Digar and Cohan, 2010) used an analytical approach to develop two RFMs; a continuum RFM and a discrete RFM. Recently a research

(Foley et al., 2014) developed and evaluated two RFMs for rapidly calculating pollutant mitigation potential considering sources, location, and precursor emission type. These RFMs have been developed and validated for several regions (elaborated in Section 2.2); however, to the best of the author's knowledge, no published literature so far has discussed the parametric sensitivity or developed an RFM in arid regions. Due to different conditions in these regions, study in this direction is expected to yield interesting results.

1.2 Research Objectives

Based on the above discussion and gap in scientific knowledge, the main goal of this research is to study the formation of secondary pollutants in the atmosphere in the context of arid regions. The specific objectives of this research are as follows:

- To setup a PAQM in an arid region to develop basic concept on the formation of secondary pollutants and study the photochemical smog formation.
- To study the effect of arid weather conditions on the chemical mechanisms in the formation of photochemical smog.
- To identify key photolysis and chemical reactions responsible in the formation of O_3 and compute corresponding sensitivity coefficients of their reaction rates.
- To develop a continuum RFM based on the DDM for efficiently representing air pollutant responsiveness to emission controls in arid regions under parametric uncertainties, including dust.

- To evaluate the abilities of the developed RFM to represent O_3 concentration responses using probability framework.

1.3 Structure of the Thesis

This study is organized into seven chapters; a brief description of each one is as follows:

Chapter 1 presents the motivation and scientific basis for embarking on this research followed by its objectives. The basic concepts and related up-to-date literature of PAQM, chemical mechanisms, and air quality response modelling with an emphasis on arid regions are elaborated in *Chapter 2*. The focus of *Chapter 3* is the data collection and analyses for the purpose of developing and validating the objectives of this research. *Chapter 4* describes the setup and configuration of meteorological model (WRF), emissions model (SMOKE), and PAQM (CMAQ) for subsequent base case run. The result of the base case run is then compared with the field-collected data. *Chapter 5* investigates the effect of various chemical mechanisms in PAQM and identifies the most appropriate mechanism and corresponding chemical kinetics for arid regions. *Chapter 6* describes the development and validation of an RFM for an arid region. In addition to employing the RFM in a probabilistic framework to study the emission reduction scenarios, it also investigates the role of mineral dust in the formation of O_3. *Chapter 7* concludes the study with recommendations for future work. Figure 1.1 illustrates the schematics of the thesis structure.

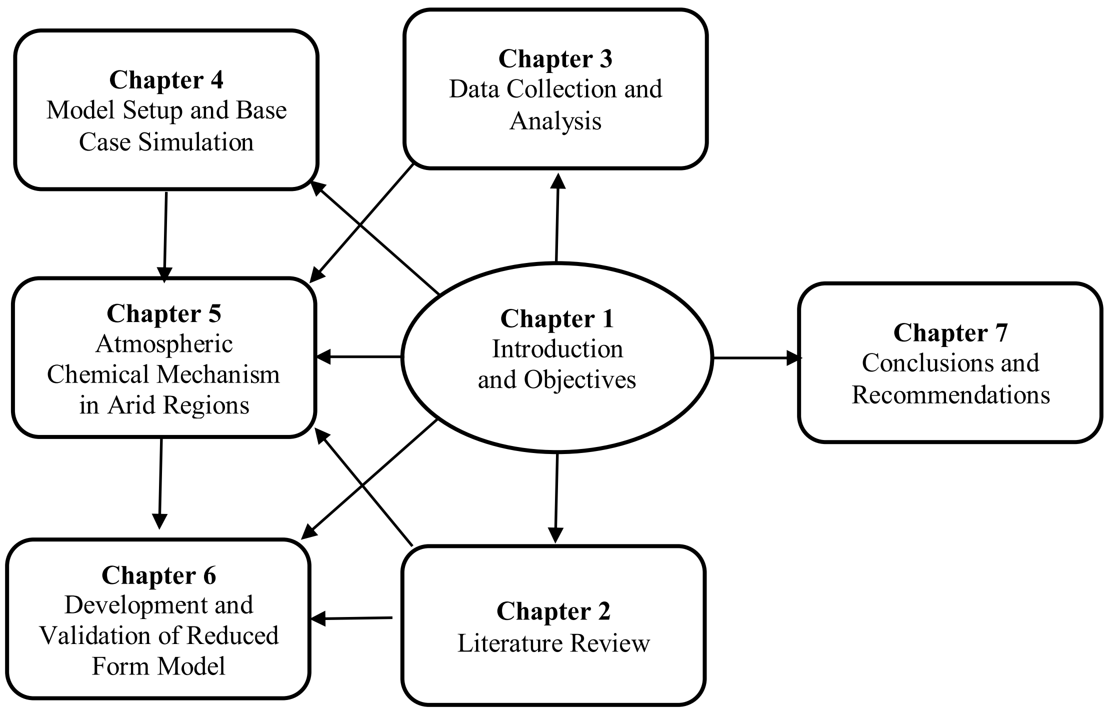

Figure 1.1 Structure of the Thesis

CHAPTER 2: LITERATURE REVIEW

2.1 Photochemical Smog

Photochemical smog is the result of a complex chemical reaction of sunlight, nitrogen oxides, and volatile organic compounds (VOCs) in the atmosphere resulting in the formation of a number of secondary pollutants, many of which are hazardous. The major constituents of photochemical smog are Ozone (O_3), VOCs, oxides of nitrogen, sulfur, peroxyacetyl nitrates (PAN), carbon monoxide, and secondary particulate matter. The formation of these components is described and explained in the following sections.

2.1.1 Formation of O_3

Four equations (2.1 - 2.4) summarize the formation of O_3 in the atmosphere (Seinfeld and Pandis, 2006).

$$O \ + \ O_2 + M \overset{1}{\rightarrow} O_3 + M \tag{2.1}$$

$$NO_2 + h\vartheta \overset{2}{\rightarrow} NO + O \tag{2.2}$$

$$NO \ + \ O_3 + M \overset{3}{\rightarrow} NO_2 + O_2 \tag{2.3}$$

$$O \ + \ NO_2 \overset{4}{\rightarrow} NO + O_2 \tag{2.4}$$

$$\begin{aligned} O_3 + h\vartheta &\overset{4a}{\rightarrow} O + O_2 \qquad \lambda > 315\, nm \\ &\overset{4b}{\rightarrow} O(1_D) + O_2 \ \ \lambda < 315\, nm \end{aligned} \tag{2.5}$$

$$O(1D) + M \overset{5}{\rightarrow} O + M \tag{2.6}$$

$$O\ (1D) + H_2O \overset{6}{\rightarrow} 2OH \tag{2.7}$$

$$CO\ +\ OH\ \overset{7}{\rightarrow} CO_2 + H^- \tag{2.8}$$

$$RH\ +\ OH + NO \overset{8}{\rightarrow} RCHO + HO_2 + NO_2 \tag{2.9}$$

The oxygen atom (*O*), which reacts with O_2 to form O_3, is produced due to the breakup of NO_2 in the presence of sunlight (Eq. 2.1 & 2.2). This produced O_3 is destroyed by the exact reverse process (Eq. 2.3). However, the reaction of hydrocarbons (R) with an *OH* radical (Eq. 2.4) increases the production of NO_2 interfering in the O_3 formation-destruction cycle. The aforementioned reaction sequences involving NO_x ($NO + NO_2$) and VOCs finally result in the buildup of tropospheric O_3. It is customary to invoke an approximation to the highly reactive species such as *O*, called pseudo-steady state approximation (PSSA) and assume that the rate of formation is exactly equal to the rate of disappearance. Applying PSSA, we can obtain the following Eqs. 2.10, 2.11, 2.12, and 2.13 for steady state concentrations of O, O_3, OH, and HO_2 respectively. The rate equation for NO_2, NO, HCHO are given in Eqs. 2.14, 2.15, and 2.16 respectively.

$$[O]_{ss} = \frac{k_1\,[NO_2]}{k_2[O_2][M]} \tag{2.10}$$

$$[O_3]_{ss} = \frac{k_1\,[NO_2]}{k_3[NO]} \tag{2.11}$$

$$[OH]_{ss} = \frac{2k_{4a}\,[HCHO]}{k_7[NO_2]} \tag{2.12}$$

$$[\mathrm{HO_2}]_{ss} = 2k_{4a}\left\{1 + \frac{k_5[\mathrm{HCHO}]}{k_7[\mathrm{NO_2}]}\right\}[\mathrm{HCHO}]/k_6[\mathrm{NO}] \tag{2.13}$$

$$\frac{d[\mathrm{NO_2}]}{dt} = \frac{2k_{4a}k_5[\mathrm{HCHO}]^2}{k_7[\mathrm{NO_2}]} \tag{2.14}$$

$$\frac{d[\mathrm{NO}]}{dt} = -2k_{4a}\left\{1 + \frac{k_5[\mathrm{HCHO}]}{k_7[\mathrm{NO_2}]}\right\}[\mathrm{HCHO}] \tag{2.15}$$

$$\frac{d[\mathrm{HCHO}]}{dt} = -\left\{k_{4a} + k_{4b} + 2k_{4a}\frac{k_5[\mathrm{HCHO}]}{k_7[\mathrm{NO_2}]}\right\}[\mathrm{HCHO}] \tag{2.16}$$

Hence, NO, NO_2, O, OH, HO2, and HCHO are usually regarded as major precursors of O_3, and to control the O_3 pollution it is necessary to reduce anthropogenic emissions producing these pre-cursors (Atkinson, 2000; Jenkin and Clemitshaw, 2000; Sillman and He, 2002; Seinfeld and Pandis, 2006). The rate of production and destruction of these precursors are largely dependent on the local conditions. Due to the nonlinear O_3-precursors relationship, reducing NO_x emissions does not always result in a decrease of O_3 concentrations in the atmosphere. In regions where O_3 decreases with NO_x reductions, other factors like VOC concentrations, source and time of emissions, and meteorology have been shown to play a major role.

Thus, a complex nonlinear O_3-NO_x-VOC relationship governs the buildup of O_3 in the troposphere. Strategies to reduce O_3 demand thorough understanding of this complex process and selection of appropriate rate constants in the air quality modelling facilitates this understanding.

2.1.2 Formation of PAN

The compound PAN was first identified as a constituent of photochemical smog in the 1950s, the general formula of which is $RC(O)OONO_2$. PAN is highly toxic to plants in addition to being damaging to the human respiratory system. The formation of PAN follows the following steps (Seinfeld and Pandis, 2006).

$$RCHO + OH \rightarrow RCO + H_2O \tag{2.17}$$

$$RCO + O_2 \rightarrow RC(O)O_2 \tag{2.18}$$

$$RC(O)O_2 + NO_2 \rightarrow CH_3C(O)O_2NO_2 + M \tag{2.19}$$

The OH radical can react with aldehydes to produce an acyl radical and water (Eq. 2.5), which then reacts with oxygen to form a peroxyacyl radical (Eq. 2.6). This peroxyacyl radical, in the presence of NO_2, forms PAN (Eq. 2.7). Thus, quantities of OH radical, organic compounds and NO_2 in the atmosphere controls the formation of PAN.

2.1.3 Secondary Organic Aerosols

The type of organic carbon (OC), which is directly emitted from sources (such as industrial), is called primary OC, and the type that is formed due to the photochemical oxidation of hydrocarbons in the atmosphere is known as secondary organic aerosol (SOA). SOA can account up to 30-60% of total organic aerosol mass at certain locations during summer (Lim and Turpin, 2002; Yu et al., 2004) and is an important constituent of photochemical smog. OC is also known for its mutagenic and carcinogenic properties, it is mainly a scattering medium and exerts negative climate forcing influence (Houghton et al., 2001).

2.2 Photochemical Smog Formation in Arid Regions

It is evident from the discussion in the preceding section that the chemical kinetics in PAQMs for the production of secondary pollutants is dependent on location. To the best of author's knowledge, there is no published literature that discusses the chemical kinetics and formation of urban smog in an arid region, particularly Saudi Arabia. Arid regions are characterized as having extreme temperatures and humidity, and frequent dust storms, in addition to intense UV radiations and lack of precipitation. An example of such a location is the city of Riyadh in Saudi Arabia. Recent studies show the declining trend of air quality in this region (Meo et al., 2013; Rushdi et al., 2013; Alharbi et al., 2014) and Riyadh is reported to be in the top 10 cities in the World with problems of urban smog (DW, 2015). The formation of urban smog in Riyadh could be attributed to the characteristics of arid regions, presence of PM, formation of O_3, and SOA, as well as, dust storms.

During summer, the climate conditions in Riyadh city are very hot and dry while winters are cold. The temperature can reach as high as 50ºC during the peak of summer (July and August), and relative humidity can go beyond 50%. The average UV radiation in

Riyadh was reported close to 300 Wh/m^2, and was observed to be higher in other regional cities (Elani, 2007).

PM and dust in the atmosphere play an important role in the formation of smog. The concentrations of PM reported by Alharbi et al., 2015 are shown in Figure 2.1. The concentrations are in general high, particularly in the summer due to dust storms. These dust storms are frequent occurrences in Riyadh, mostly occurring in the summer (further discussed in Chapter 3). The impact of dust storms on aerosol optical properties for Saudi Arabia was studied and it was found that dust storm events significantly change the optical properties of aerosol (Maghrabi et al., 2011; Alharbi et al., 2013; Alharbi et al., 2015) suggesting the presence of high ionic concentrations in the atmosphere. These factors play an important role in the formation of photochemical smog.

O_3 and SOA are important constituents in photochemical smog. As described in Chapter 3, the data analyzed as part of this research showed significant concentrations of O_3 in Riyadh. This highlights the importance of studying O_3 photochemistry since O_3 follows a unique trend in urban and rural areas. The secondary organic carbon (SOC) concentrations, an indicator of SOA, was estimated (Alharbi et al. 2016) in Riyadh. Its spatial distribution is illustrated in Figure 2.3. The concentrations were higher than some cities in Europe and Asia (Grivas et al., 2012; Lonati et al., 2007; Ho et al., 2006).

Another unique characteristic of arid regions is the negligible precipitation, which causes insignificant wet deposition. The city of Riyadh receives a scanty rainfall and this enables the pollutants including the constituent of photochemical smog to stay in the air for longer periods, thus causing more harm. The presence of significant amounts of O_3, SOA, and particulates in Riyadh (Shareef et al., 2016; Alharbi et al., 2015), in addition to its arid region characteristics, emphasizes the need to study the chemistry of photochemical smog in arid regions, in general, and Riyadh as a specific case.

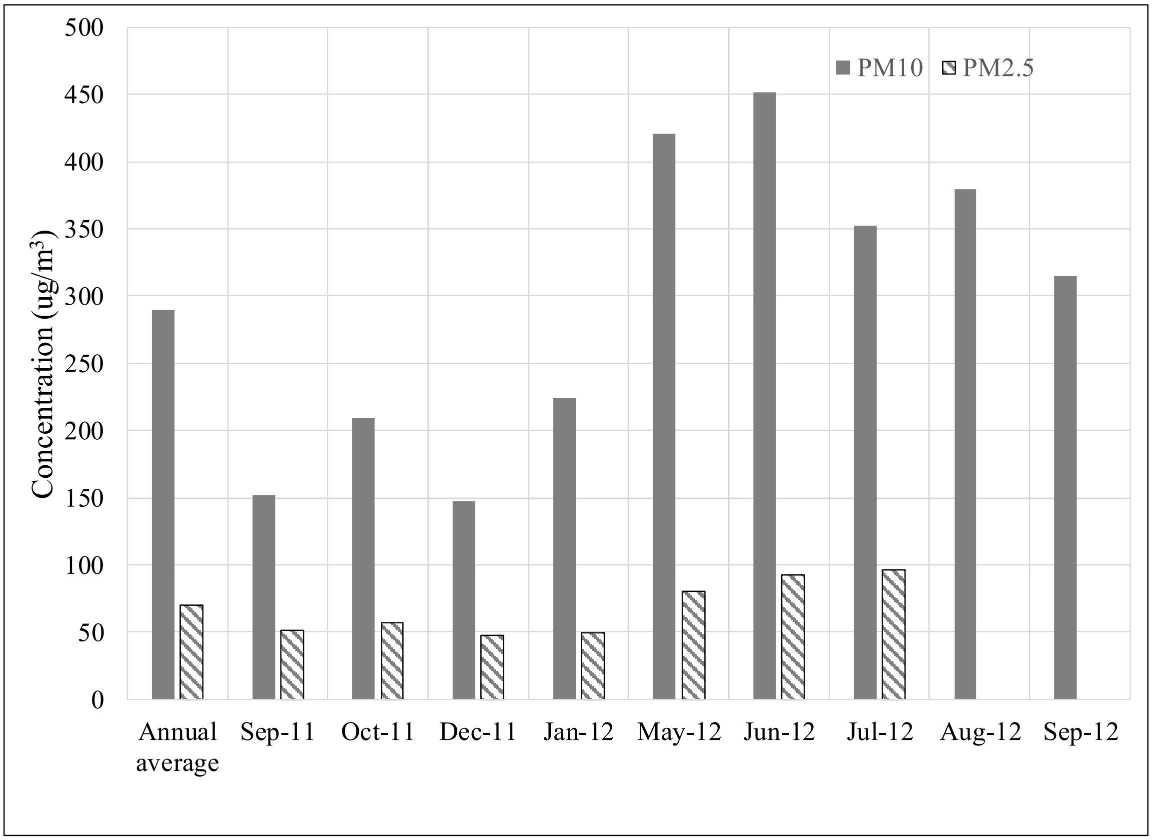

Figure 2.1 Annual and Monthly Average PM_{10} and $PM_{2.5}$ Concentrations in Riyadh (Alharbi et al., 2015)

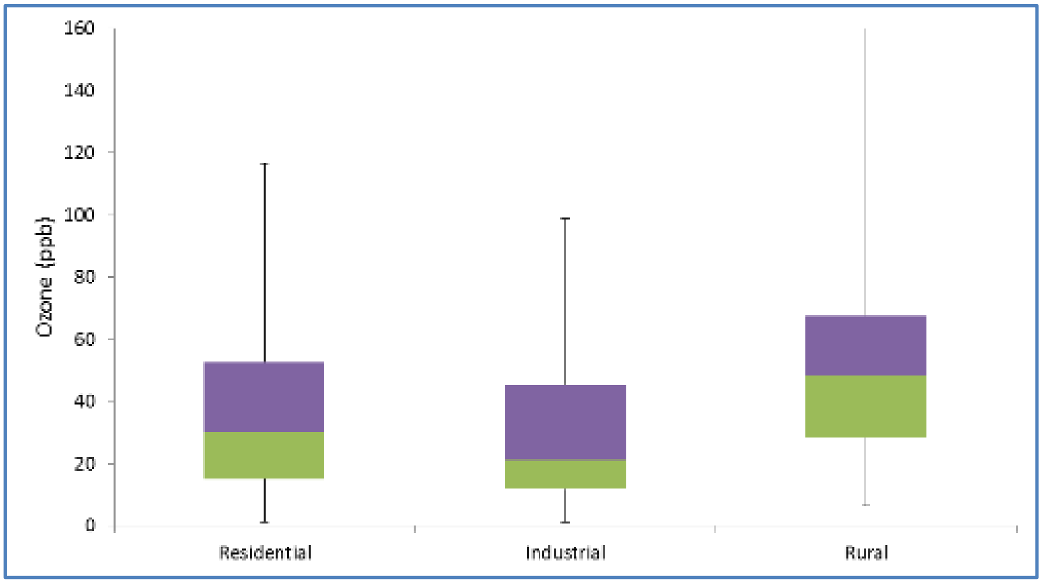

Figure 2.2 O_3 Concentrations at Different Locations in Riyadh City (Shareef, et al., 2015)

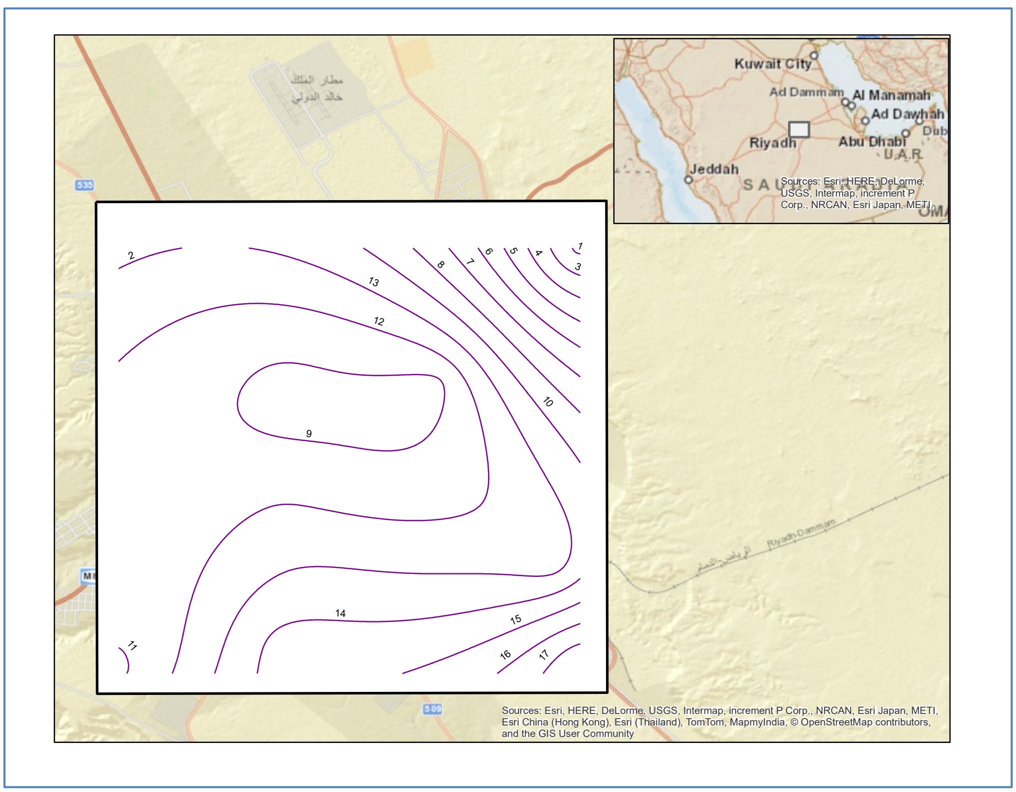

Figure 2.3 Spatial Distribution of Estimated SOC ($\mu g/m^3$) in Riyadh City (Alharbi et al., 2016)

The unique characteristics of arid regions discussed above highly alter the chemical mechanisms, particularly the dust conditions. Experimental studies have showed heterogeneous reactions of NO_2 and HNO_2 on oxides and mineral dust as illustrated in Eq. 2.20 - 2.23 (Underwood et al. 2001).

$$2NO_2\ (g) + H_2O\ (a) \rightarrow HONO\ (g) + HNO_3\ (a) \qquad (2.20)$$

$$MO + 2HNO_3 \rightarrow M\ (NO_3)_2 + H_2O \qquad (2.21)$$

$$NO_2(g) \rightarrow NO_2(a) \qquad (2.22)$$

$$2NO_2(g) \rightarrow NO_3\ (a) + NO(g) \qquad (2.23)$$

Hence, the loss of NO_x to dust can influence the O_3 levels, particularly in NO_x limited areas. Some studies have observed that O_3 is reduced up to 40% in the presence of Saharan dust (DeReus et al., 2000; Umann et al., 2005; Bonasoni et al., 2004), however, others reported no influence on the O_3 formation due to dust (Fairlie et al., 2010). Studies have also suggested connections between increases in reaction rates and humidity. Recently, a research (Zhang et al., 2015) studied the chemistry of inorganic aerosol formation and proposed a new heterogeneous chemistry in PAQM. This heterogeneous chemistry is shown to be highly dependent on weather conditions, especially humidity. The research, however, did not study the effect on the formation of O_3. Based on the preceding discussions, the current research will employ PAQM to examine the mechanisms of chemical formation of photochemical smog in arid conditions. Running PAQM with the appropriate chemical kinetics would help in proposing appropriate abatement strategies.

2.3 Photochemical Air Quality Modelling

In a typical air pollution system, PAQMs establish mathematical linkages from sources to receptors by incorporating the transport mechanism in the atmosphere. Primarily, two types of PAQMs are used: Lagrangian trajectory models that simulate changes in the chemical composition of a given air parcel as it is advected in the atmosphere and Eulerian models, which describe the concentration in an array of fixed computational cells (Seinfeld and Pandis, 2006). Eulerian PAQMs are widely used to develop optimal emission control strategies that are both environmentally protective and cost effective and to advance the understanding of atmospheric science (Dennis et al. 2010). Eulerian based known PAQMs have also been used extensively to predict changes in secondary pollutant concentrations such as O_3 with respect to various precursor emission control strategies (Derwent and Davies, 1994; Collins et al., 1997; Harley et al., 1997; Godowitch et al., 2008). Eulerian models are computationally efficient, incorporates extensive chemistry and the predictions are proven to be more reliable (El-Harbawi, 2013).

The rate of change in pollutant concentrations is governed by the following advection-diffusion equation (Seinfeld and Pandis, 2006).

$$\frac{\partial c_i}{\partial t} = \underbrace{-\frac{\partial y}{\partial x_i} u_j c_i}_{\text{Advection}} + \underbrace{D_i \frac{\partial^2 c_i}{\partial x_j \partial x_j}}_{\text{Diffusion}} + \underbrace{P_i(c_1 \dots\dots\dots c_N, T)}_{\text{Chemical Production Reactions}} - \underbrace{D_i(c_1 \dots\dots\dots c_N, T)}_{\text{Chemical Destruction Reactions}} + \underbrace{E_i(x, t)}_{\text{Emissions}} \quad (2.24)$$

i = 1, 2, …, N

c_i = concentration of each species at i

u_j = j[th] component of the fluid velocity

D_i = molecular diffusivity of species i the carrier fluid

P_i = rate of production of species i by chemical reaction

D_i = rate of destruction of species i by chemical reaction

E_i = emission rate of species i at location x and time t

The concentration of a pollutant at a given location and time is the factor of advection, diffusion, chemical reactions forming the pollutant, chemical reactions destroying the pollutants and the emissions coming from various sources. The focus of the current study is the chemical reactions, which forms and destroys the pollutants especially that present in photochemical smog. Chemical reactions taking place in the atmosphere could be either photolysis i.e. disintegration of compound under solar radiation and the reactions between various compounds by chemical kinetics. These are discussed in the following sections.

2.3.1 Chemical Mechanisms in PAQMs

A study by Byun (Byun and Schere, 2006) identified three primary mechanisms that were originally developed to address issues associated with urban O_3 formation and acidic deposition; these mechanisms are the Carbon Bond (CB) (Gery et al., 1989), Regional Acid Deposition Model (RADM) (Stockwell et al. 1990) and State Air Pollution Research Center (SAPRC) (Carter, 2000). These are briefly described below. The number of species and reactions of various mechanisms are summarized in Table 2.1 and discussed in the following sections.

Table 2.1 Number of Species and Reactions in Different Chemical Mechanisms

Sno.	Chemical Mechanism	Species	Reactions
1	cb05e51	148 (Aerosol=25; Gas=123)	343
2	cb05tucl	107 (Aerosol=24; Gas=83)	235
3	saprc07tc	186 (Aerosol=25; Gas=161)	741
4	saprc07tb	186 (Aerosol=25; Gas=161)	457
5	saprc07tic	231 (Aerosol=33; Gas=198)	928
6	racm2	156(Aerosol=22; Gas=134)	400

2.3.1.1 Carbon Bond Lumped Mechanisms

The original CB mechanism CB04 (Gery et al., 1989) was based on simple Arrhenius law rate constant forms that were derived from more complex temperature and pressure rate constants. CB04 is a lumped structure that is the fourth in a series of carbon-bond mechanisms, included 36 species, and 96 reactions of which 12 were photolytic. Subsequent changes were made by adding rate constants for the formation and decomposition of PAN and a termination reaction between the XO2 and XO2N operators and the HO2 radical. Another study (Carter and Atkinson, 1996; Carter, 1996) enhanced this mechanism by updating the isoprene chemistry. An additional study (Yarwood et al., 2005) proposed a major update to CB04 in terms of kinetic and photolysis and extended the inorganic reaction set. This update was named CB05, and it included 52 chemical species. The model performance using the CB05 mechanism was shown to be more precise in the results for O_3 and OCs at high-altitude and rural areas (Sarwar et al., 2008). CB05 was further improved to include toluene chemistry, CB05-TU, and this was proven to have better accuracy in predicting the O_3 formation rate (Whitten et al., 2010). CB mechanisms have been widely used in several studies to develop reduced form models (Digar et al., 2011; Foley et al., 2014; Foley et al., 2015) and to study O_3 and meteorological sensitivities (Appel et al., 2010; Li et al., 2011). CB05 was also used to study the oxidation of reactive VOCs and other processes (Dunker et al., 2014).

2.3.1.2 RADM2/RACM2 Mechanisms

RADM2 is a lumped species mechanism that uses a reactivity-based weighting scheme to account for the lumping of chemical compounds into surrogate species. It was built on the RADM1 (Stockwell, 1986), by including higher classes of alkenes and isoprene, more detailed aromatic chemistry, and the treatment of peroxy radical reactions (Stockwell et al., 1990). A further improvement in the photo-oxidation of isoprene was done by Zimmermann and Poppe (1996). The base mechanism included 57 model species and 158 reactions, 21 of which are photolytic. RADM2 was later updated to Regional Atmospheric Chemistry Mechanism (RACM) (Stockwell et al. 1997) and recently to RACM2 (Goliff et al., 2013). Some recent studies have used these RADM2/RACM2 mechanisms to model air quality (Zhang et al., 2015; Baro et al., 2015).

2.3.1.3 SAPRC Mechanisms

SAPRC99 is a detailed variable lumped parameter chemical mechanism containing 72 model species and 214 reactions, of which 30 are photolytic (Carter, 2000) It covers mechanism for gas-state atmospheric reactions of VOCs and NO_x in urban and regional atmospheres, the details of which are documented elsewhere (Carter, 1999). SAPRC99 was later updated to SAPRC07 to reflect the new kinetic and mechanistic data and to incorporate new data on several types of VOCs (Carter, 2010).

2.3.2 Comparison of Chemical Mechanisms

The chemical mechanisms discussed in the previous sections share the common concept of reaction rates and products, however, differ in terms of rate constants, photolysis (due to change in pressure and temperature), and treatment of condensed organic chemistry. The radicals: hydroxyl radical (OH), hydrogen peroxide (H_2O_2), and PAN play important role in the formation and destruction of O_3. Hence, understanding the formation and destruction of these compounds along with their reaction rates are important (formation equations discussed in Section 2.1). Table 2.2 to Table 2.5 compare the reactions and rate constants for O_3, OH, H_2O_2 and PAN for various chemical mechanisms respectively.

The chemical reactions producing and destroying O_3 are shown in Table 2.2. Primarily O_3 is formed by reaction shown by Eq. 2.1. The reaction rates differ in the three mechanisms and dependent on temperature. O_3 is also formed by the reactions with various radicals (acetyle, peroxy acyl, aromatic and acrolein) and is only captured by SAPRC07. As shown in the Table 2.4, formation of H_2O_2 in CB05 and SAPRC07 is similar except for the additional reaction OH + OH = H_2O_2 in CB05, however, it also has an additional destruction reaction (H_2O_2 + O = OH + HO_2). RACM2 produces additional H_2O_2 because of the reactions of O_3 with different organic compounds, such as alkenes. Although the reaction rates differ (RACM2 reaction rate being the highest), the formation mechanisms of the three mechanisms in PAN are similar.

Table 2.2 Chemical Reactions and Rates Describing the Formation and Destruction of O_3 in Various Mechanisms

Reactions	Reaction Rates		
	RACM2	CB05	SAPRC07
Formation			
O3P + O_2 + M = O_3	5.74E-34*(T/300)(-2.6)	6.0E-34*(T/300)(-2.4)	5.68e-34*(T/300)(-2.60)
Acetyl Peroxy Radicals $MECO_3$ + HO_2 = O_3 + other compounds	-	-	5.20e-13*exp(980/T)
Higher peroxy acyl Radicals RCO_3 + HO_2 = O_3 + other compounds	-		5.20e-13*exp(980/T)
Peroxyacyl radical formed from Aromatic Aldehydes $BZCO_3$ + HO_2 = O_3 + other compounds	-	-	5.20e-13*exp(980/T)
Methacrolein and other acroleins. $MACO_3$ + HO_2 = O_3 + other compounds	-	-	5.20e-13*exp(980/T)
Destruction			
O_3 + NO = NO_2	1.4E-12*exp(-1310./T)	3.0E-12*exp(-1500.0/T)	3.00e-12*exp(-1500/T)
O_3 + NO_2 = NO_3	1.4E-13*exp(-2470./T)	1.2E-13*exp(-2450/T)	1.40e-13*exp(-2470/T)
O_3 = O1D	1.0/<O_3O1D_NASA06>	1.0/<O_3_O1D_IUPAC04>	1.0/<O_3O1D_06>
O_3 = O_3P	1.0/<O_3O_3P_NASA06>	1.0/<O_3_O_3P_IUPAC04>	1.0/<O_3O_3P_06>
OH + O_3 = HO_2	1.7E-12*exp(-940./T)	1.7E-12*exp(-940/T)	1.70e-12*exp(-940/T)
HO_2 + O_3 = OH	1.0E-14*exp(-490./T)	1.0E-14*exp(-490/T)	2.03e-16*(T/300)(4.57)*exp(693/T)

Table 2.3 Chemical Reactions and Rates Describing the Formation and Destruction of OH in Various Mechanisms

Reactions	Reaction Rates		
	RACM2	CB05	SAPRC07
Formation			
$O1D + H_2O = 2*OH$	2.14E-10	2.2E-10	$1.63e-10*exp^{(60/T)}$
$O_3 + HO_2 = OH + 2O_2$	$1.0E-14*exp^{(-490./T)}$	$1.0E-14*exp^{(-490/T)}$	$2.03e-16*(T/300)^{(4.57)}*exp^{(693/T)}$
$NO + HO_2 = NO_2 + OH$	$3.45E-12*exp^{(270./T)}$	$3.5E-12*exp^{(250/T)}$	$3.60e-12*exp^{(270/T)}$
$NO_3 + HO_2 = 0.8*OH + 0.8*NO_2 + 0.2*HNO_3$	4.0E-12	-	4.00e-12
Destruction			
$O_3 + OH = HO_2$	1.7E-12*exp(-940./T)	$1.7E-12*exp^{(-940/T)}$	$1.70e-12*exp^{(-940/T)}$
$H_2 + OH = HO_2$	$7.70E-12*exp^{(-2100./T)}$	5.5E-12*exp(-2000./T)	$7.70e-12*exp^{(-2100/T)}$
$H_2O_2 + OH = HO_2$	$2.9E-12*exp^{(-160./T)}$	$2.9E-12*exp^{(-160/T)}$	1.80e-12
$HONO + OH = NO_2$	$2.5E-12*exp^{(260./T)}$	$1.8E-11*exp^{(-390/T)}$	$2.50e-12*exp^{(260/T)}$
$NO_2 + OH = HNO_3$	$k_0=1.51E-30*(T/300)^{(-3.0)}$	$k_0=2.0E-30*(T/300)^{(-3.0)}$,	$k_0=3.2e-30*(T/300)^{(-4.50)}$
$HNO_3 + OH = NO_3$	$k_0=2.4E-14*exp^{(460/T)}$,	$k_0=2.4E-14*exp^{(460/T)}$	$k_0=2.40e-14*exp^{(460/T)}$
$NO_3 + OH = HO_2 + NO_2$	2.0E-11	2.2E-11	2.00e-11
$CH_4 + OH = MO_2$	$1.85E-12*exp^{(-1690./T)}$	2.45E-12*exp(-1775/T)	1.85e-12*exp(-1690/T)
$NO + OH = HONO$	$k_0=7.0E-31*(T/300)^{(-2.6)}$	$k_0=7.0E-31*(T/300)^{(-2.6)}$,	$k_0=7.00e-31*(T/300)^{(-2.60)}$,

Table 2.4 Chemical Reactions and Rates Describing the Formation and Destruction of H_2O_2 in Various Mechanisms

Reactions	Reaction Rates		
	RACM2	CB05	SAPRC07
Formation			
$HO_2 + HO_2 = H_2O_2$	k_1=2.2E-13exp$^{(600./T)}$	k_1=2.3E-13*exp$^{(600/T)}$	k_1=2.20e-13*exp$^{(600/T}$
$HO_2 + HO_2 + H_2O = H_2O_2$	k_1=3.08E-34$^{(2800./T)}$	k_1=3.22E-34*exp$^{(2800/T)}$	k_1=3.08e-34*exp$^{(2800/T)}$
$OH + OH = H_2O_2$	-	k_0=6.9E-31*(T/300)$^{(-1.0)}$	-
OLT + O_3 = H_2O_2 + other compounds	4.33E-15*exp$^{(-1800.0/T)}$	-	-
DIEN + O_3 = H_2O_2 + other compounds	1.34E-14*exp$^{(-2283.0/T)}$	-	-
ISO + O_3= H_2O_2 + other compounds	7.86E-15*exp$^{(-1913./T)}$	-	-
API + O_3 = H_2O_2 + other compounds	5.0E-16*exp$^{(-530./T)}$	-	-
LIM + O_3 = H_2O_2 + other compounds	2.95E-15*exp$^{(-783./T)}$	-	-
Destruction			
H_2O_2 = 2OH	1.0/<H_2O_2_RACM2>	1.0/<H_2O_2_IUPAC10>	1.0/<H_2O_2>
H_2O_2 + O = OH + HO_2		1.4E-12*exp$^{(-2000./T)}$	
H_2O_2 + OH = HO_2	2.9E-12*exp$^{(-160./T)}$		1.80e-12
OLT + O2 = H_2O_2 + other compounds	4.33E-15*exp$^{(-1800.0/T)}$	-	-
DIEN + O_2 = H_2O_2 + other compounds	1.34E-14*exp$^{(-2283.0/T)}$	-	-
ISO + O_2 = H_2O_2 + other compounds	7.86E-15*exp$^{(-1913./T)}$	-	-
API + O_2 = H_2O_2 + other compounds	5.0E-16*exp$^{(-530./T)}$	-	-
LIM + O_2 = H_2O_2 + other compounds	2.95E-15*exp$^{(-783./T)}$	-	-

Table 2.5 Chemical Reactions and Rates Describing the Formation and Destruction of PAN in Various Mechanisms

Reactions	Reaction Rates		
	RACM2	CB05	SAPRC07
Formation			
$C_2O_3 + NO_2 = PAN$	-	k_0=4.9E-3*exp$^{(-12100/T)}$	-
$MECO_3 + NO_2 = PAN$	-		k_0=2.70e-28*(T/300)$^{(-7.10)}$
$ACO_3 + NO_2 = PAN$	k_0=9.7E-29*(T/300)$^{(-5.6)}$		
Destruction			
$PAN = C_2O_3 + NO_2$	-	k_0=4.9E-3*exp$^{(-12100/T)}$	
$PAN = MECO_3 + NO_2$	-	-	k_0=4.90e-03*exp$^{(-12100/T)}$
$PAN = ACO_3 + NO_2$	9.00E-29*exp$^{(14000/T)}$	-	-
$PAN = 0.6*NO_2 + 0.6*C_2O_3 + 0.4*NO_3 + 0.4*MEO_2$	-	1.0/<PAN_IUPAC10>	
$PAN = 0.6*MECO_3 + 0.6*NO_2 + 0.4*MEO_2 + 0.4*CO_2 + 0.4*NO_3$	-	-	1.0/<PAN>
$PAN + HO = XO_2 + NO_3 + HCHO$	4.0E-14	-	-

The reverses of the same mechanisms destroy PAN; additionally, it is also destroyed with the formation of NO_2, NO_3 and other compounds. In RACM2, PAN reacts with OH to form NO_3 and other organic compounds.

Several studies have compared these mechanisms and found large variations among model predictions due to various reactions and rates. In particular, a 2003 study (Jimenez et al. 2003) reported considerable variation in model prediction when using CB04 and SAPRC99, particularly variations in reactive species such as HO_2 and NO_3. A comparison between RADM2 and its update showed large species and process differences in organic speciation in urban and rural conditions (Gross and Stockwell, 2003). Tonnesen and Luecken (2001) studied the differences between the two mechanisms, CB04 and SAPRC99, and observed that differences in production and propagation of HO_2 and hydroxyl radicals (OH) (together known as HO_x), and organic peroxy radicals' effects on O_3 formation. Both the studies by Byun and Faraji (Byun and Schere, 2006; Faraji et al., 2008), using air quality models with versions of CB04 and SAPRC99 over southeast Texas, often predicted more O_3 with the SAPRC99 model. Luecken et al., (2008) also reports higher concentration of O_3 using SAPRC99. The predicted O_3 concentrations are similar for most of the United States, but statistically significant differences occur in many urban areas and central US. They also note that the difference in O_3 predictions depends on location, the VOC/NOx ratio, and concentrations of precursor pollutants. Another study compared the atmospheric composition using CB05TU and RACM2 and reported a large variation in the prediction of chemical species (Sarwar et al., 2013).

2.3.3 PAQM Computational Model and Response Modelling

A detailed analysis of the state-of-the-art computational models for PAQM is presented elsewhere (El-Harbawi, 2013). Among the various photochemical models, Model-3 is widely used to study the formation of secondary pollutants. Also known as CMAQ (community multiscale air quality), it is a 3D, grid-based air quality model developed by the US-EPA. It simulates O_3 and photochemical oxidants, PM, and deposition of pollutants such as acids, toxic pollutant, and nitrogen species. CMAQ is an active, open-source project that continuously enhances the accuracy and efficiency of the photochemical modelling by taking advantage of state of the art multi-processor computing techniques. It is maintained by Community Modelling & Analysis System (CMAS), the details can be found at their website (Community Modelling and Analysis System (CMAS), 2016). The core programs, relationship among various components and dependencies on external programs of CMAQ are elaborated in Chapter 4.

Several recent studies have used CMAQ to study the atmospheric chemistry (Sarwar et al., 2008; Cohan et al., 2010; Sarwar et al., 2013), evaluate uncertainty (Simon et al., 2013; Foley et al., 2015), study haze pollution (Wang et al., 2012), biomass burning (Huang et al., 2013), and health impacts (Arunachalam et al., 2011). CMAQ has been used extensively in all aspects of this research.

The primary inputs to an air quality model are meteorology, pollutant emissions, and chemical mechanism as depicted in Figure 2.4.

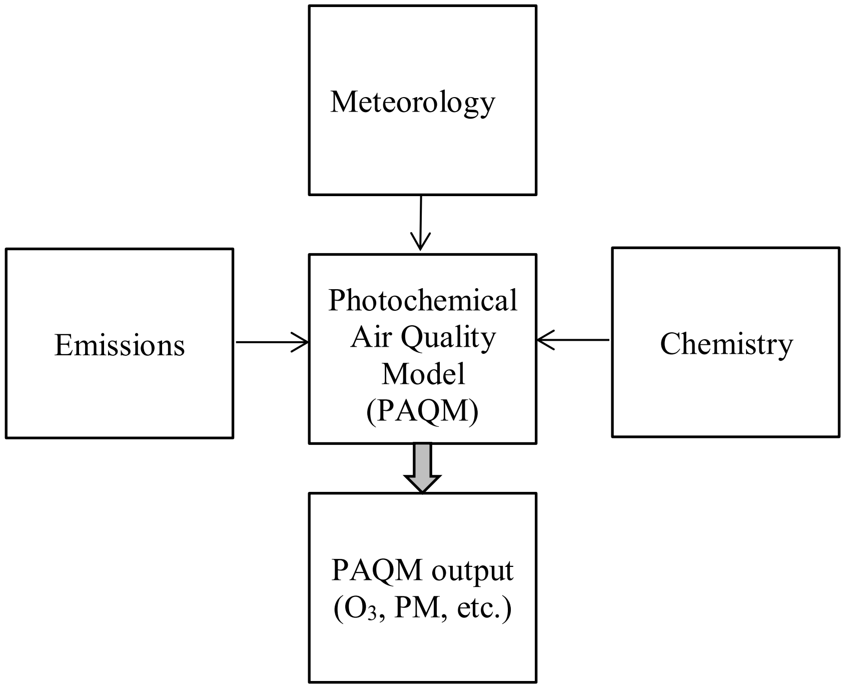

Figure 2.4 Air Pollution System

The meteorology and emissions input to an air quality model are produced by mathematical models based on complex nonlinear representation of physical processes in the environment. The chemical transformations of pollutants are governed by complex chemical phenomenon in the atmosphere. These chemical and physical processes introduce significant uncertainties in model predictions. The first source of this uncertainty is related to parameters (input emission parameters, reaction rate constants and boundary conditions) and the second is structural uncertainty (errors due to model assumptions and formulations). The complexity of these uncertainties further increases for secondary pollutants (such as O_3) which form from nonlinear interactions of precursor compounds (Lin et al., 1998). These uncertainties are generally characterized by studying the responses to fixed levels of emission changes, called response modelling. This following section describes air quality response modelling techniques.

The primary measure of an air quality model is the accuracy of simulated concentration relative to ambient observations (Dennis et al., 2010). Response modelling characterizes the responsiveness of concentration to emissions. This sensitivity modelling of pollutant responsiveness to various emitters is particularly useful to demonstrate an attainment plan and apportion the origin of pollutant concentrations.

2.3.4 Response Modelling Techniques

The most widely used methods of response modelling techniques to probe relationships between concentrations and emissions in photochemical models are brute-force, decoupled direct method, adjoint and source apportionment. Two of these most widely used methods (brute-force and direct decoupled method) as presented in (Cohan and Napelenok, 2011) are summarized below.

2.3.4.1 Brute-Force Methods

The brute-force or finite difference method (BFM) computes differences between the concentrations in simulations with base and perturbed rates of emissions or other parameters with the rest of the conditions being held constant. The primary advantage to this approach is that it can be easily implemented into any photochemical model, without the need for extensive programming. In this method, it is typically assumed that the rate of concentration changes per emission change can be linearly interpolated or extrapolated to predict the impacts of emission changes that are smaller or larger than the level explicitly modelled. Suppose concentrations $C_i(x,t)$ are simulated under the base and perturbed scenarios as $\{\tilde{E}_{(i,0)}(x,t)\}$ and $\{\tilde{E}_{(i,f)}(x,t)\}$ where $\tilde{E}_f$ differs from $\tilde{E}_0$ by a fraction of Δf, the following equations can be formulated.

$$\tilde{E}_f \equiv (1+\Delta f)\tilde{E}_0 \tag{2.25}$$

$$C_0 \equiv C(\tilde{E}_0) \tag{2.26}$$

$$C_f \equiv C(\tilde{E}_f) \tag{2.27}$$

Ignoring the notations for the species (I =1,…,N), position (x= (x, y, z)), and time (t) the concentrations $C\epsilon$ under any other emission level $E\epsilon$ could then be approximated by linearly scaling the difference in concentrations between the base and perturbed simulations:

$$E_\epsilon \equiv (1+\Delta\in)E_0 \tag{2.28}$$

$$C_\epsilon \approx C_0 + \frac{\Delta\in}{\Delta f}(C_f - C_0) \tag{2.29}$$

For pollutants such as O_3, which has a nonlinear response to emission rates, the accuracy of Eq. 2.29 will tend to degrade as the fractional perturbation of interest ($\Delta\epsilon$) differs more sharply from the explicitly modelled perturbation. Sometimes the central difference method is applied to improve the accuracy of brute-force activities as shown in Eq. 2.30.

$$C_{\epsilon} \approx C_0 + \frac{\Delta\epsilon}{2\Delta f}(C_f - C_{-f}) \quad (2.30)$$

where C_{-f} are the concentrations under emission level $\widetilde{E}_{-f}$. This approach, however, doubles the required number of perturbation simulations thus requiring more computational time. BFM, though simple to apply, suffers from limitations. It requires computationally burdensome number of model simulations when several input perturbations are of interest. It has been shown to be susceptible to numerical instability due to model discontinuities and round-off errors (Napelenok et al., 2006; Hakami et al., 2007; Henze et al., 2007). Furthermore, the impacts of perturbations in multiple emission components will be strictly additive for a nonlinear concentration-emission response. One approach to represent the joint impacts of simultaneous emission perturbations is response surface modelling. Brute-force modelling is conducted for a matrix of perturbation scenarios, each representing different levels of perturbations in emission components. Statistical analysis is then applied on the results to create a response surface that estimates concentrations for any combination of perturbations in the emission components (Hill et al., 2009; US EPA, 2006). Response surface modelling, a meta-model built upon multi BFM simulations was applied to characterize the nonlinear response of O_3 to precursor emissions in China (Xing et al. 2011). BFM was applied with varying degrees of emission perturbations, e.g., from small (e.g., 10-30%) (Vautard et al., 2005; Wang et al., 2012) to moderate (e.g., 30-50%) (Pun et al. 2008) and large perturbations (e.g., 100% reduction, i.e., the source category is completely eliminated or zeroed out) (Burr and Zhang, 2011; Wang et al., 2012). BFM, along with other methods, was applied to assess trans-boundary O_3 contribution in South

Korea and it was found that BFM overestimates the concentrations (Choi et al., 2014). Another study (Yarwood et al., 2013) showed that BFM is more accurate in winter than summer, and is more accurate in urban locations verses rural ones. Still, BFM was successfully applied to a single source facility to distinguish the impacts of primary (emitted) and secondary (formed) pollutants (Baker and Kelly, 2014). Due to its simplicity and ability to capture indirect effects associated with the interactions between PM species and their precursors, BFM was applied to study the impact of emission inventories on source apportionment of fine particles and O_3. A study by Zhang et al., (2014) used CMAQ with BFM to assess the impact of updated emission inventories of fine particles and O_3 over the southeastern US.

2.3.4.2 Decoupled Direct Method

Several attempts have been made to embed the differencing numerous brute-force simulations by computing pollutant sensitivities directly within a photochemical model. The Coupled direct method and Green's function method, though, have been found to be unstable and impractical to use in comprehensive photochemical models (Yang et al., 1997). However, the decoupled direct method (DDM) developed by (Dunker, 1984) and an adjoint sensitivity analysis developed by Elbern et al., (1997) have been shown to steadily and efficiently compute sensitivity relationships and have been widely implemented in various models (Hakami et al., 2007; Henze et al., 2007).

The basic concept of DDM is that it operates by tracking sensitivity coefficients of all concentrations to specified model inputs or parameters, utilizing equations derived from those representing the concentrations in the underlying model to evolve sensitivities. The atmospheric diffusion equation (ADE) representing the transport and reactions of chemical compounds in photochemical models can be written in simplified form as:

$$\frac{\partial C}{\partial t} = -\nabla(uC) + \nabla(K\nabla C) + R + E + \cdots \tag{2.31}$$

In the above equation, u(x, t) is the wind field, K(x, t) is the turbulent diffusivity tensor, $R_i(x, t)$ is the net rate of chemical production, $E_i(x, t)$ is the emission rate, and the ellipsoids denote other processes that are represented by the model. ADE is solved by the operator splitting and is subject to initial and boundary conditions that are described in another study (Mcrae et al., 1982).

Suppose that we are interested in how the concentrations vary with perturbations in targeted model inputs or parameters $P_j(x, t)$, which may be perturbed from their unperturbed values P_j by scaling the factors $\in_j$ (similar to Eq. 2.26):

$$p_j = \in_j P_j = (1 + \Delta\in_j)P_j \tag{2.32}$$

Since our interest here is in sensitivities to emission, note that each parameter p_j is equivalent to an emission component $\widetilde{E}$ in the same notation used as in the previous section. Semi-normalized sensitivity coefficients $S_{i,j}^{(1)}(x, t)$ of concentration responses to p_j are developed by scaling non-normalized local sensitivity coefficients $(\frac{\partial C}{\partial P_j})$ by the unperturbed value P_j of the parameter:

$$S_j^{(1)} = P_j \frac{\partial C}{\partial P_j} = P_j \frac{\partial C}{\partial(\epsilon_i P_j)} = \frac{\partial C}{\partial \epsilon_j} \tag{2.33}$$

This semi-normalization simplifies calculations by placing sensitivity coefficients into the same units as concentrations. For sensitivity to emission rates, DDM computes the evolution of $S_j^{(1)}$ by substituting Eq. 2.33 into Eq. 2.31, yielding Eq. 2.34 (Hakami et al., 2003; Yang et al., 1997).

$$\frac{\partial S_j^{(1)}}{\partial t} = -\nabla\left(uS_j^{(1)}\right) + \nabla\left(K\nabla S_j^{(1)}\right) + F_i S_j^{(1)} + \widetilde{E}_j + \cdots \tag{2.34}$$

In the equation above, F is the Jacobian matrix ($F_{ik} = \frac{\partial R_i}{\partial C_k}$) and $\widetilde{E}_j$ is the base level emission inventory component represented by the sensitivity parameter p_j.

The process sensitivities in DDM approach are updated separately from, and after concentrations. Eq. 2.34 has been implemented into the air quality models by different approaches. Computational efficiency was seen when a variation of DDM-3D factorizes the Jacobian Matrix only once per every advection time step (Yang et al., 1997), while applying the original formulation of Dunker (1984) and maximizes the accuracy and consistency of sensitivity results. Several implementations of both DDM (Dunker et al., 2002; Koo et al., 2007) and DDM-3D (Hakami et al., 2003; Cohan et al., 2005; Koo et al., 2007; Napelenok et al., 2008) have been validated for computationally efficient and consistent results relative to BFM.

The accuracy degrades, though, with linear scaling of the local first-order DDM with large nonlinear perturbations. In order to address this degradation, a 2003 study (Hakami et al., 2003) extended DDM to HDDM to compute the second-order or even higher sensitivity coefficients. Second-order self-sensitivity coefficients $S_{i,j}^{(2)} = \frac{\partial^2 C}{\partial \epsilon_j^2}$ represent the curvature of concentration response to a single parameter, whereas cross-sensitivity coefficients $S_{j,k}^{(2)} = \frac{\partial^2 C}{\partial \epsilon_j \partial \epsilon_k}$ characterize how sensitivity of concentrations to parameters changes as another parameter is varied.

That same study (Hakami et al., 2003) additionally demonstrated the consistency of HDDM and BF finite differencing in estimating second order local sensitivities. It was also shown that expanding the Taylor series, incorporating first and second order HDDM coefficients, reliably predicted O_3 response to large perturbations (over 50%) to multiple parameters.

$$C_{\epsilon_j,\epsilon_k} \approx C_o + \Delta\epsilon_j\, S_j^{(1)} + \Delta\epsilon_k\, S_k^{(1)} + \frac{\Delta\epsilon_j^2}{2} S_j^{(2)} + \frac{\Delta\epsilon_k^2}{2} S_k^{(2)} + \Delta\epsilon_j\, \Delta\epsilon_k\, S_{j,k}^{(2)} + \mathrm{HOT} \qquad (2.35)$$

In Eq. 2.35 $C_{\epsilon_j,\epsilon_k}$ denotes concentrations when parameters P_j and P_k are perturbed by fractions $\Delta\epsilon_j$ and $\Delta\epsilon_k$, respectively. Although, higher order terms (HOT) have been neglected in the equation. Several studies applied Eq. 2.35 with HDDM to predict O_3 (Cohan et al., 2005; Jin et al., 2008; Kim et al., 2009; Xiao et al., 2010), however, only a few have applied it to other pollutant, such as particulate matter (Zhang and Russell, 2010). DDM has also been applied to study the response of pollutant concentrations to emission changes. A study by Cohan et al. (2006) considered the control of cost, the focus of Tagaris et al., (2010) was health effects, and Liao et al. (2007) studied climate change, all, by applying DDM sensitivities. HDDM coefficients were applied to generate isopleth of O_3 response to simultaneous changes in VOC and NO_x emissions (Hakami et al., 2004). Inverse modelling of emission inventories was done using HDDM, top down analysis (Hu et al., 2009), iterative inverse modelling (Mendoza-Dominguez and Russell, 2000), and Kalman filter inversion Napelenok et al. (2008). Reactions and uncertainties were studied by applying DDM sensitivity to reaction rate constants (Gao et al., 1996; Cohan et al., 2010). Yarwood et al., (2013) demonstrated the feasibility of applying HDDM to calculate first and second order sensitivity of O_3 at continental scale. HDDM method was reported favourable when compared to other methods because of trans-boundary O_3 study (Choi et al., 2014). A study by Digar and Cohan (2010) used an analytical approach to develop two reduced form models; continuum RFM and discrete RFM. Both models demonstrated a high level of accuracy in predicting O_3 and inorganic PM. They emphasized the assessment of the model in different regions and modified it to study meteorological uncertainties.

As discussed in this chapter, both methods of air quality response modelling have been applied extensively to study the sensitivity of various parameters under different conditions. However, no published study has yet applied those photochemical models or studied for secondary pollutants, that form from nonlinear interactions of precursor compounds, in an arid region, particularly Saudi Arabia. The declining air quality, unique characteristics of this location (as discussed in Section 2.2), and a need to find an optimal solution necessitates such a study in this region.

CHAPTER 3: DATA COLLECTION AND ANALYSIS

3.1 Site Selection and Air Quality Parameters

As Riyadh City in Saudi Arabia is categorized as arid, it was selected to collect air quality data for developing and validating the objectives of this research. The city was divided into 16 grids (as shown in Figure 3.1), and various air quality parameters (including primary and secondary pollutants) were collected from the center of each grid for a period of one year. The grids were mainly classified as industrial (predominantly industries in the area) and residential (largely residential areas) as shown in Table 3.1. This effort generated a large amount of in-situ and laboratory analyzed data (meteorological and air quality) including primary and secondary pollutants that are listed in Table 3.2. The following sections present the data collection and analyses methodology and the results of the analyses.

3.2 Data Collection Methodology

3.2.1 In-situ Parameters

Two mobile stations were employed to collect the samples from various locations at different times. Each sampling was performed in each grid for 24 hours at a flow rate of 16.67 lpm (1 m^3/h) on quartz microfiber filter discs (47 mm) using PQ-100 particulate samplers with PM_{10} inlet (BGI Incorp. USA) and the air inlet was located 2.5 m above ground level. Prior to every sampling, the filters were baked at 300–550°C for at least 4 h to remove any trace of organics. After sampling, the filters were packed in petri dishes covered with aluminum foil to protect them from sunlight.

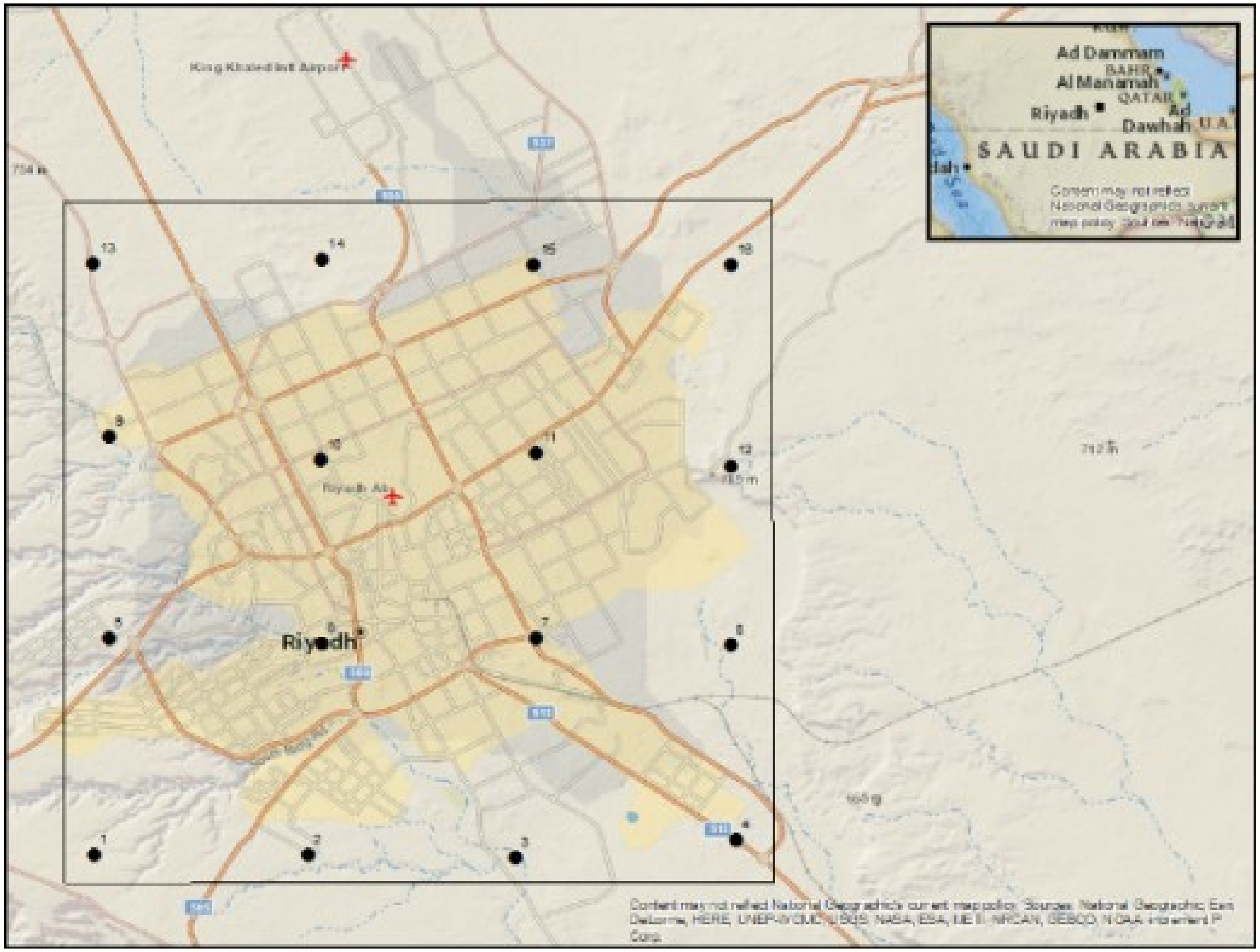

Figure 3.1 Data Collection Locations

Table 3.1 Description of Grids

Grid No.	General Classification	Type
1	Semi background area (semirural area)	Outskirts
2	Residential and some small scale industrial area (suburban area)	Residential
3	Moderately populated residential area with car salvage yards and some agricultural farms (suburban area)	Residential
4	Industrial area (urban area)	Industrial
5	Residential densely populated area (urban area)	Residential
6	Commercial, industrial and residential very densely populated area with city sewage wastewater treatment plants (urban area)	Residential
7	Industrial and residential area with a cement factory situated in this area with continual stone crushing operations activities (urban area)	Industrial
8	Semi industrial area with commercial train route passing through (suburban area)	Industrial
9	Residential area mostly covered with agricultural land (suburban area)	Residential
10	Residential area (urban area)	Residential
11	Residential and semi industrial area with number of automobile workshops (urban area)	Industrial
12	This area is considered residential area with number of automobile workshops (suburban area)	Residential
13	Semi background/residential area (semirural area)	Residential
14	Residential area with extended construction activities (suburban area)	Residential
15	Residential area (suburban area)	Residential
16	Semi background with small populated residential area and large non Agricultural vacant land (semirural area)	Residential

Table 3.2 Meteorology and Air Quality Parameters that were Collected

Type	Parameters
Meteorology	Wind speed, Wind direction, Atmospheric temperature, Relative Humidity, Solar radiation, Atmospheric pressure
Onsite criteria pollutants	Ozone (O_3), Particulate Matter (PM_{10}, $PM_{2.5}$), Carbon Monoxide (CO), Nitrogen Oxides (NO, NO_2, NO_x), Sulfur dioxide (SO_2), TS, THC, Non-CH_4, CH_4
Particulate matter ions and metals	Cations (NH_4^+, Ca^{2+}, Mg^{2+}, Na^+, K^+), Anions (Cl^-, NO_3^-, SO_4^{--}), Metals (As, Co, Te, Mo, V, Ni, Cr, Cu, Cd, Li, Pb, Zn, Mn, B, K, Na, Mg, Fe, Al)
Carbon	Elemental and organic carbons (EC and OC)

Filters were conditioned in a desiccator at constant temperature ($23\text{-}25^0C$) and relative humidity (40-50%) before and after every sampling and the initial and final weight of each filter disk was recorded to determine particulate mass collected over the period of sampling time while not in use, the filter disks were stored at a temperature of -1°C

Apart from PQ-100 particulate samplers, both mobile stations were equipped with a TEOM-1400a (Thermo Fisher Scientific, Inc.) and an ambient Particulate Monitor attached with an Automatic Cartridge Collection Unit (ACCU) for particulate collection on quartz microfiber filter discs (47 mm). In one station, the monitor was fitted with a PM_{10} inlet while in the other station the monitor was fitted with a $PM_{2.5}$ inlet. The total flow rate in the system was 16.67 lpm/min and this flow was bifurcated in two channels. The channel, which went to the TEOM unit, maintained 3.0 lpm/min and the other channel to the ACCU unit maintained 13.67 lpm/min. The $PM_{2.5}$ samples collected from the ACCU unit and the PQ-100 sampler were utilized for the analysis of ionic concentration, in this research. For the analysis of elemental concentrations, only the PM_{10} samples collected with the PQ-100 samplers were utilized. Table 3.3 summarizes the methodology used to collect each of the pollutants.

Table 3.3 Methodologies used in Sampling

Sample	Methodology
NO, NO_2, NO_x and O_3	NO, NO_2 and NO_x: CO-Dual Beam based on chemiluminescence with lowest detectable limit was 1 ppb. O_3: O_3-UV photometer with a lowest detectable limit of 04 ppb
Particulates	PQ-100 particulate samplers equipped with TEOM-1400a ambient particulate monitor
Ionic Analysis	Anions: Shimadzu Ion-Chromatography system with CDD-6A conductivity detector and Shim pack IC- A1 column Cations: Shim pack IC- C3(100mm x 4.6mmID) column was used and Oxalic acid (3.0 mM)
Silica Analysis	Silicomolybdate method (# 8185) by DR/4000 Spectrophotometer (Program # 3350)
Elemental Analysis	USEPA Compendium Method IO-3.1

3.2.2 Sample Extraction and Analysis

Water soluble ionic components (NH_4^+, Ca^{2+}, Mg^{2+}, Na^+, K^+, Cl^-, NO_3^-, SO_4^{2-} and Silica) associated with sampled particulate were determined by an aqueous extraction method. Each sample filter disc was cut into pieces and taken into a polypropylene tube (50ml capacity) separately containing 20 ml of de-ionized water. The tubes containing the samples were sonicated for an hour, initially for 30 minutes and interrupted for an hour to settle down the filter fragments, then sonication again for another 30 minutes. After sonication, the samples were subjected to centrifugation at 3,000 rpm in order to settle the particles and then the supernatant extract was finally filtered through an Acrodisc (0.45µm) with a disposable syringe.

3.2.2.1 Ionic Analysis

Anions (Cl^- NO_3^- and SO_4^{2-}) were analyzed using Shimadzu Ion-Chromatography system with a CDD-6A conductivity detector and Shim pack IC- A1 column. Mobile phase containing 2.5mM Phthalic acid and 2.4mM Tris- (hydroxymethyl) aminomethane was used with a flow rate of 1.5ml/min at a temperature of 40°C. The instrument was calibrated with a Dionex anion standard (Dionex Seven Anion standard #057590, Thermo Fisher Sci, USA). Each sample was analyzed thrice and average concentration value was recorded.

For cations (NH_4^+ K^+ Mg^{2+} Na^+ and Ca^{++}), a Shim pack IC- C3(100mm x 4.6mmID) column was used and Oxalic acid (3.0 mM) mobile phase with flow rate of 1.0ml/min at a temperature of 40°C was applied. Calibration was done with a Dionex Standard (Dionex Six Cation Standard #046070, Thermo Fisher Sci, USA).

3.2.2.2 Analysis of Silica

Analysis of Silica was performed by utilizing a 5 ml the of same aqueous extract which was prepared for ionic analysis following the Silicomolybdate method (#8185) by DR/4000 Spectrophotometer (Program # 3350) as recommended by HACH Co., USA.

3.2.2.3 Elemental Analysis

Microwave assisted acid extraction was performed following the USEPA Compendium Method IO-3.1 and using advanced composite vessels in the MDS 2100 microwave digestion system (CEM Crop, UK). The extracting acid was prepared in a 1-liter volumetric flask, combined in order by mixing 500 mL of deionized distilled water, 55.5 mL of concentrated nitric acid, and 167.5 mL of concentrated hydrochloric acid that was cooled and diluted to 1 liter with deionized distilled water. After cutting the filter papers into small pieces, 20 mL of the extracting acid was added. The microwave digestion system was programmed to 50% power, 30-psi pressure for 30 minutes of digestion. Aliquot of digested samples was filtered by Acrodisc syringe filters (0.2 μm). Blank samples were also run simultaneously. Analyses of elements were carried out following the Compendium Method IO-3.4. The targeted elemental analysis was finally performed by using ICP-OES (Optima-2000DV, Perkin Elmer,USA). Calibration of the elements was performed using the ICP Multi Elemental Standard solution VI CertiPUR (Merck Co.) as reference material. Every sample was estimated thrice and the mean concentration was calculated.

3.3 Data Analysis

3.3.1 Meteorological Conditions

The temperature pattern observed at all three locations were similar. The minimum and maximum temperatures were approximately 25ºC and 50ºC respectively. The wind-rose diagrams from the modelled data at residential, industrial, and rural locations are shown in

Figure 3.2. The winds have a generic pattern of coming from northeast at three locations, however, at residential location winds are also coming from southwest. The maximum wind speeds were 10.9 m/s, 11.9 m/s, and 11.1 m/s in the residential, industrial, and rural locations respectively. The winds usually remained in the range of 2.5-4.5 m/s, 4.5-6.5 m/s, and 2.5-4.5 m/s in the residential, industrial, and rural sites. The relative humidity values were in the range of 25-35% at all three locations.

3.3.2 Particulates and Chemical Composition

A total of 185 PM_{10} samples were collected over a period of a year, and these collected samples were analyzed for various metals and ions. Table 3.4 presents the summary of the statistics of PM_{10}, metals, and ions of samples collected in summer (April to September) and winter (October to March) and the average for the whole year. Annual PM_{10} concentrations were in the range of 39.71- 1 803 $\mu g/m^3$ with a mean and standard deviation of 289.24 ± 228.5 $\mu g/m^3$. The average monthly variation of PM_{10} and annual average are shown in Figure 3.3. The annual average PM_{10} concentration was over 3 times higher than the ambient air quality limits (80 $\mu g/m^3$) recommended by PME, the country's environmental regulatory authority standards (PME, 2011). The average PM_{10} value is slightly higher than the values reported in 2006-2007 (Rushdi et al., 2013) in Riyadh.

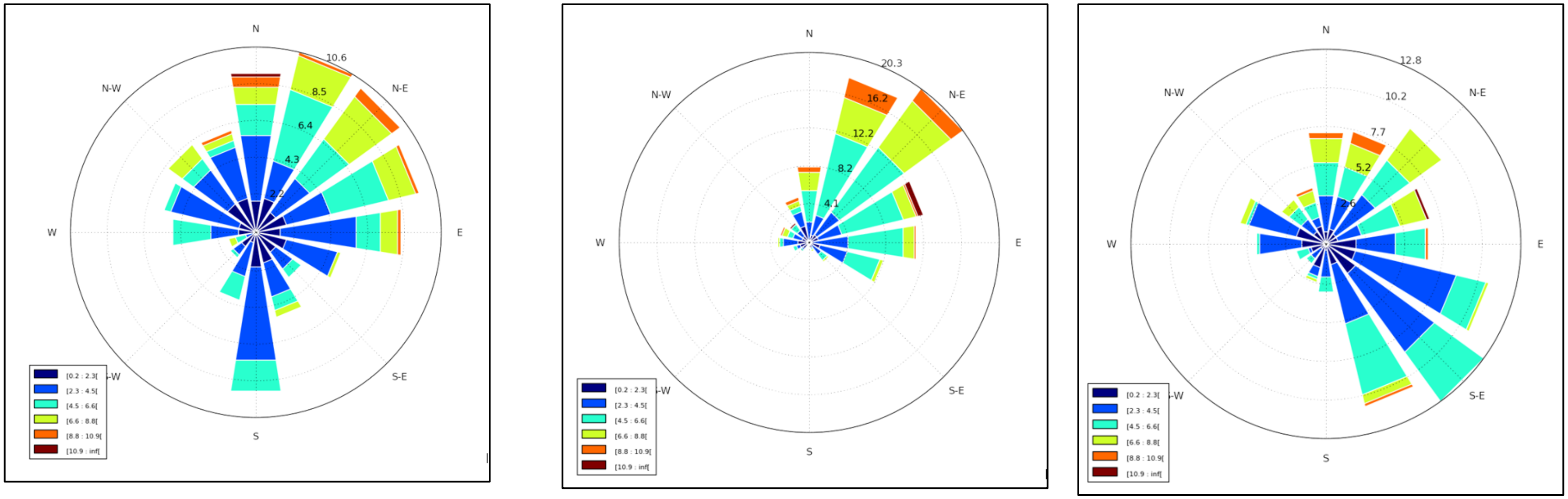

Figure 3.2 Wind Rose Diagrams (winds coming from) at Residential, Industrial and Rural Locations for July 2012.

Table 3.4 Summary Statistics of PM_{10} and Chemical Components

	Summer				Winter				Annual			
	Min	Max	Average	SD	Min	Max	Average	SD	Min	Max	Average	SD
PM_{10}	69.98	1 803.47	359.18	271.52	39.71	468.44	195.39	93.47	39.71	1 803.47	289.24	228.85
Al	0.38	80.03	9.79	11.54	0.67	14.43	3.27	2.87	0.38	80.03	7.01	9.49
As	0.02	0.04	0.02	0.01	0.01	0.07	0.04	0.03	0.01	0.07	0.04	0.02
B	0.00	2.00	0.16	0.27	0.03	1.36	0.12	0.22	0.00	2.00	0.14	0.25
Ca	0.07	276.78	57.35	51.31	0.14	71.87	13.59	19.23	0.07	276.78	38.66	46.15
Cd	0.00	0.72	0.15	0.18	0.00	0.12	0.05	0.05	0.00	0.72	0.09	0.13
Co	0.00	0.04	0.01	0.01	0.01	0.07	0.04	0.02	0.00	0.07	0.03	0.02
Cr	0.02	0.43	0.10	0.06	0.02	0.95	0.15	0.14	0.02	0.95	0.13	0.11
Cu	0.00	0.61	0.07	0.09	0.00	0.46	0.13	0.10	0.00	0.61	0.10	0.10
Fe	0.18	71.43	9.58	10.34	0.18	12.95	2.04	2.70	0.18	71.43	6.36	8.84
K	0.27	11.61	1.69	1.72	0.26	2.63	0.86	0.48	0.26	11.61	1.34	1.40
Li	0.00	0.77	0.03	0.08	0.00	3.08	0.35	0.56	0.00	3.08	0.17	0.40
Mg	0.42	48.37	6.88	7.42	0.58	10.13	2.57	1.88	0.42	48.37	5.04	6.12
Mn	0.00	1.44	0.18	0.21	0.00	0.35	0.09	0.06	0.00	1.44	0.14	0.17
Mo	0.00	0.12	0.03	0.03	0.00	0.53	0.08	0.10	0.00	0.53	0.06	0.08
Na	0.25	16.18	3.57	2.73	0.67	7.16	2.19	1.39	0.25	16.18	2.97	2.35
Ni	0.00	0.21	0.04	0.03	0.00	0.13	0.06	0.03	0.00	0.21	0.05	0.04
Pb	0.00	0.80	0.06	0.14	0.00	0.38	0.06	0.06	0.00	0.80	0.06	0.11
Te	0.00	0.06	0.02	0.01	0.00	0.05	0.02	0.01	0.00	0.06	0.02	0.01
V	0.00	0.20	0.03	0.03	0.01	0.10	0.05	0.02	0.00	0.20	0.04	0.03
Zn	0.00	1.22	0.12	0.24	0.00	0.75	0.06	0.11	0.00	1.22	0.09	0.18
pH	5.43	8.80	6.95	0.53	6.67	7.35	6.98	0.16	5.43	8.80	6.96	0.46
EC	41.00	227.00	99.02	36.63	73.00	261.00	157.49	38.12	41.00	261.00	115.01	45.23
TDS	26.24	145.28	63.37	23.44	46.72	203.68	103.67	29.98	26.24	203.68	74.39	31.05
NH_4^+	0.64	11.56	3.80	2.84	0.00	13.05	4.25	3.50	0.00	13.05	3.99	3.13
Ca^{2+}	2.16	31.02	9.67	6.52	0.02	12.21	3.21	3.04	0.02	31.02	6.84	6.16
Mg^{2+}	0.15	0.58	0.31	0.14	0.00	0.34	0.13	0.13	0.00	0.58	0.21	0.16
Na^+	0.07	3.53	1.40	0.95	0.67	6.75	2.75	1.49	0.07	6.75	2.40	1.49
K^+	0.01	3.33	1.04	0.80	0.05	4.81	0.83	0.81	0.01	4.81	0.94	0.80
Cl^-	0.25	27.05	5.88	4.70	0.55	83.26	11.45	10.99	0.25	83.26	8.36	8.56
NO_3^-	0.02	21.02	3.96	3.37	0.03	33.88	5.80	5.18	0.02	33.88	4.72	4.30
SO_4^{--}	3.62	38.87	9.83	5.17	1.90	25.80	9.34	5.06	1.90	38.87	9.63	5.12
Silica	1.60	37.01	11.37	6.21	0.42	20.75	7.45	4.49	0.42	37.01	9.69	5.86

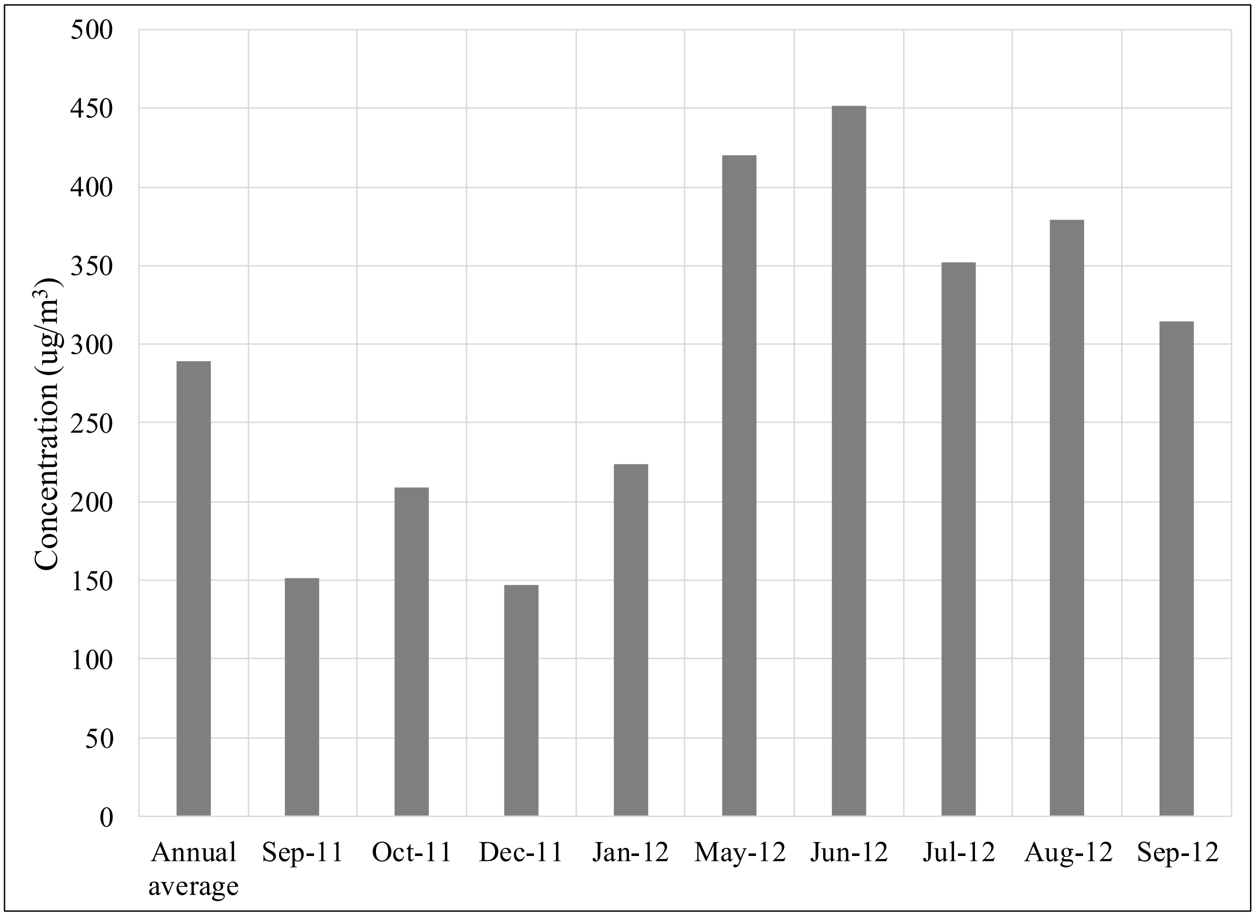

Figure 3.3 Overall Annual and Monthly Mean PM_{10} Concentrations

Also, these PM_{10} values are greater than any other city in the region such as Jeddah, Saudi Arabia (87 µg/m^3 in 2011) (Khodeir et al., 2012), Al-Mirfa, UAE (157 µg/m^3 in 2009) (Al Katheeri et al., 2012), Tehran, Iran (100 µg/m^3 in 2010) (Givehchi et al., 2013), Beirut, Lebanon (103 µg/m^3 in 2007) (Saliba and Massoud, 2010), and Kuwait, Kuwait (93 µg/m^3 in 2008)(Brown et al., 2008). However, Ahvaz, Iran reported a much larger average value of 1072 µg/m^3 (Shahsavani et al., 2012).

Table 3.4 also presents the concentrations of metals and ions with average and standard deviations. The average metal and soluble ionic concentrations in PM_{10} were about 21.5%

and 16.2% respectively. In PM_{10}, over 90% of the metals were Ca, Al, Fe, and Mg, and 70% of total ions were constituted of SO_4^{2-}, Cl^-, and NH_4^+. This indicates that the substantial part of the PM_{10} is composed of metals of crustal origin and secondary inorganic compounds such as sulfate, chloride and ammonium. High quantities of chloride are generally found in coastal city air because of their vicinity to the sea, however, this is found in high concentrations in Riyadh city which is about 400 km away from the sea.

The sea has negligible contribution to PM_{10} pollutants in Riyadh as was shown in Beijing (Wang, et al., 2005). A major cause for this presence of chloride in the air could be calcium chloride, which is used for maintaining unpaved roads and for fortifying road bases for new construction activities. Construction activities were also high during the sampling period. Moreover, chloride is also found predominantly near motor workshops (Sulaiman et al., 2005), Riyadh has several such workshops in the vicinity of the city, further increasing chloride pollution. Coal burning, which is traditionally used for outdoor activities in Riyadh, could be another contributing reason for the high concentration of chloride in the atmosphere.

3.3.2.1 Temporal Variation

3.3.2.1.1 Summer vs. Winter

Figure 3.4 presents PM_{10} comparison for different scenarios including summer and winter. As observed in the figure, PM_{10} concentration was about 84% higher in summer than in winter; this is in line with other studies (Contini et al., 2010; Shahsavani et al., 2012;

Rushdi et al., 2013). This higher concentration is attributed to dust storms that occur mostly during summer, thus increasing the PM_{10} concentration. On the other hand, the rain in winter, although relatively small, dampens PM_{10} concentrations, thus reducing the concentration in winter when compared to summer.

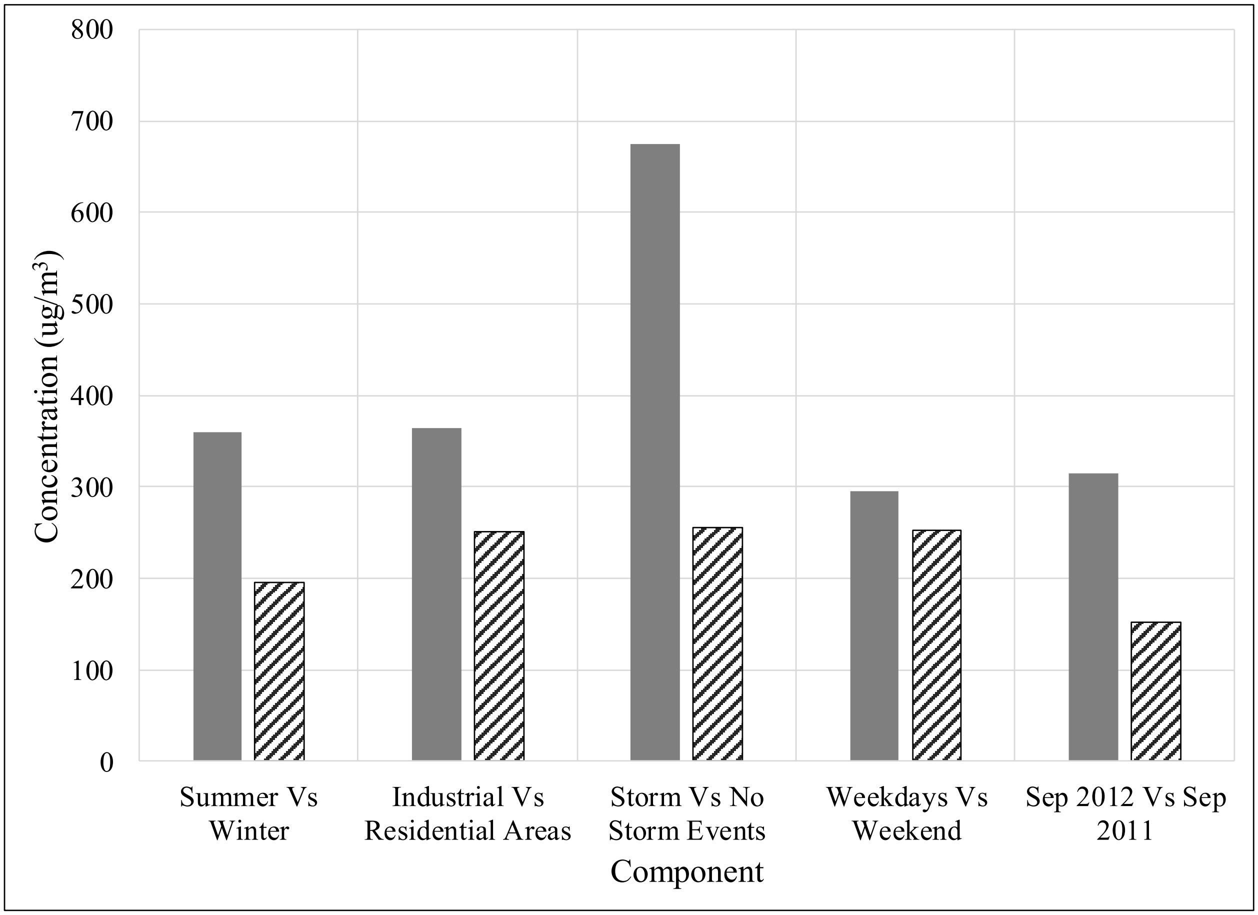

Figure 3.4 Comparison of PM_{10} Concentrations under Different Scenarios

The significant source of PM_{10} in summer, as mentioned above is mainly because of dust storms, this fact is substantiated by increase in the crustal matter species, such as Fe, Mn, Ti, Ca^{2+}, and Mg^{2+}, during summer by several folds (as illustrated in Figure 3.5). The concentrations of SO_4^{2-}, K^+, and NH_4^+ did not show any significant seasonal change.

However, Na^+, Cl^-, and NO_3^- showed higher average concentration in winter. These ions have an opposite trend with respect to the PM_{10} concentration and crustal species. Increased construction and outdoor activities in the city is the reason for high concentration of sodium and chloride in winter.

Other studies (Querol et al., 2004; Wang et al., 2005) also reported NO_3^- as having higher concentrations in the winter, and this pattern is generally attributed to low thermal stability of NO_3^- in summer (Contini et al., 2010). Other noteworthy metals that increased concentration in summer are Cd, Zn, B, and Na. This can be attributed to anthropogenic activities, which generally increase in summer. In winter, Li was found to have concentrations 12 times that of summer, and its cause requires further investigation.

3.3.2.1.2 Weekday vs. Weekend

Out of 185 days of sampling, 25 were Fridays (Friday is weekend in Saudi Arabia). A decrease of 17% of the PM_{10} concentration (Figure 3.3) was observed during the weekends. Similar trends were reported by Contini et al., (2010) (decrease of 19%) and by Morawska et al., (2002) (decrease of 70%). This indicates the presence of anthropogenic contributions particularly vehicular traffic during the weekdays. The average metallic and ionic concentrations of weekdays and weekends were also compared as illustrated in Figure 3.6. Generally, Na^+, K^+, NO_3^- and SO_4^{2-} were higher during weekdays indicating that the source of these ions is human activity.

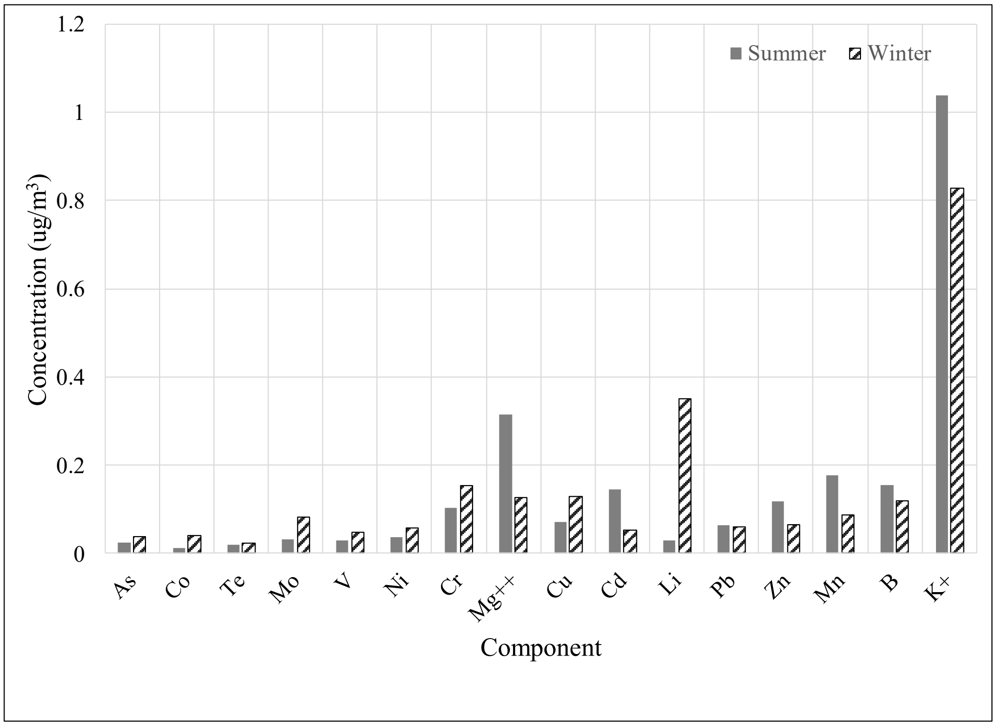

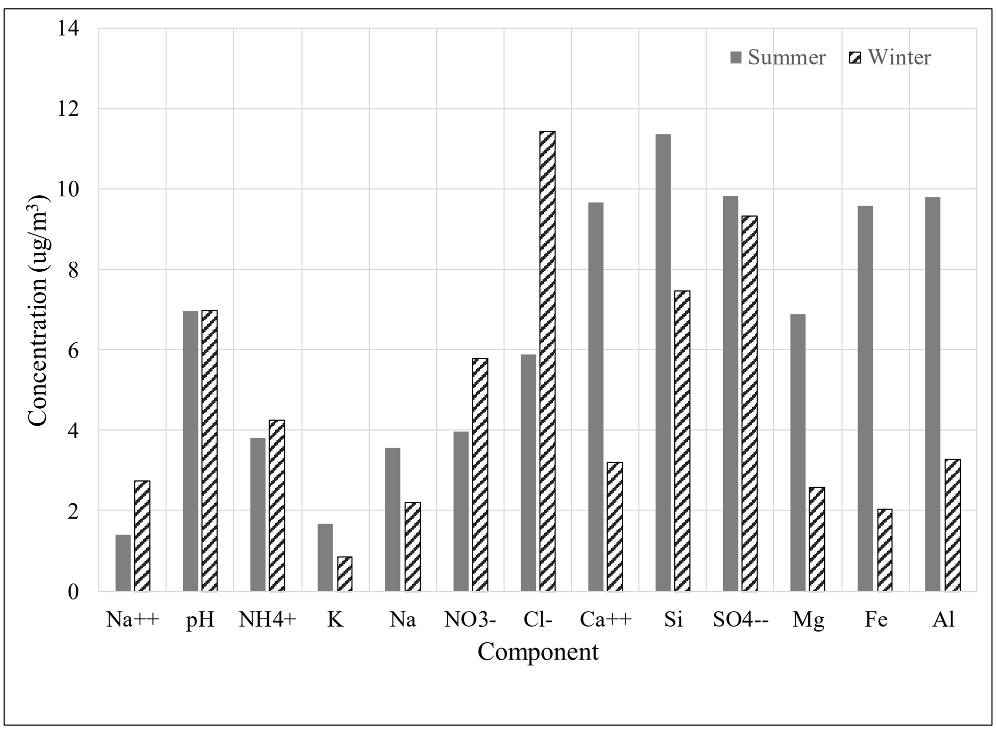

Figure 3.5 Temporal Comparison (Summer vs. Winter) a) Metals and Ions with Concentration < 1.4 b) Metals and Ions with Concentration >1.4

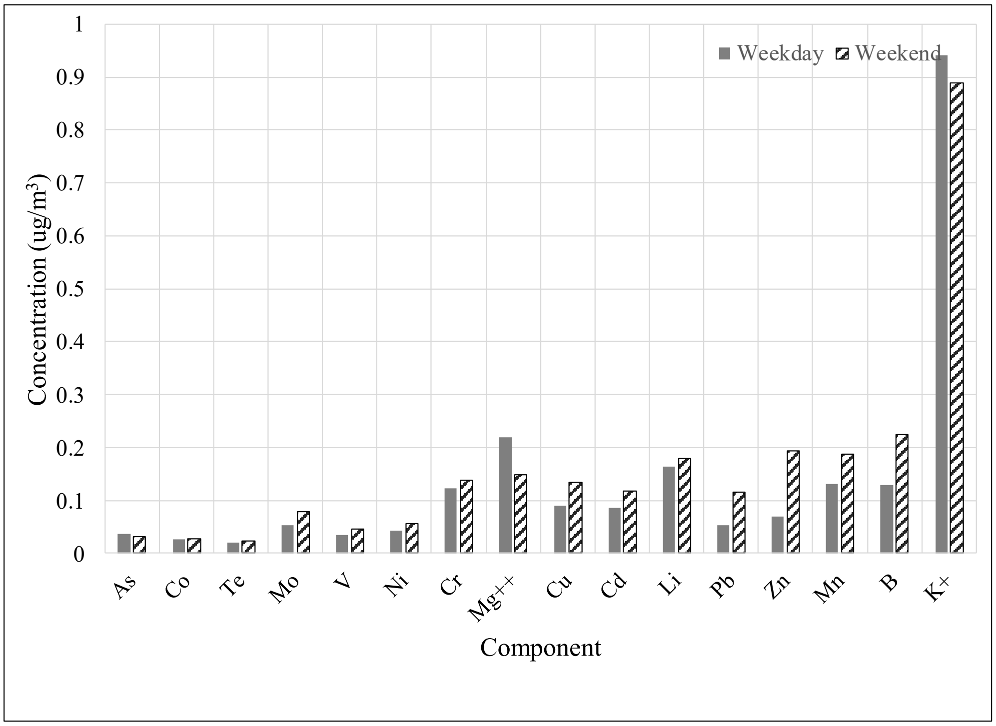

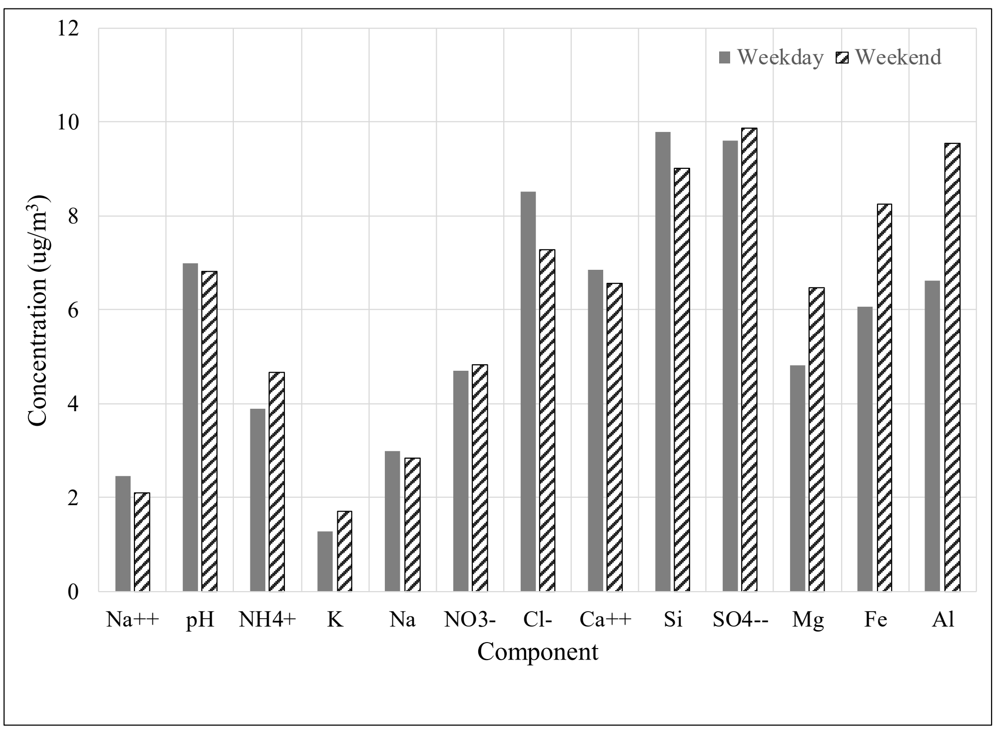

Figure 3.6 Temporal Comparison (Weekday vs. Weekend) a) Metals and Ions with Concentration < 1.4 b) Metals and Ions with Concentration >1.4

3.3.2.1.3 September 2012 vs. September 2011

To get an understanding of the state of air quality over a period of one year, the average concentration of PM_{10} of September 2011 and September 2012 were compared (Figure 3.3). It is evident from the figure that PM_{10} concentrations in 2012 were twice (207% increase) that of 2011. This shows that the PM_{10} concentration increased tremendously over a year. In addition to increase in dust storm events, emissions from vehicles and a surge in construction activities could be the primary reasons for this increase. A similar increase in concentrations was also reported by Rushdi et al., (2013).

It was observed that the concentrations of NO_3^{2-}, Mg, Fe, and Al also increased in 2012 (Figure 3.7). The increase in NO_3^{2-} is primarily considered to be from vehicular exhaust. This could be attributed to an increase in traffic over the year because the city is expanding at a rapid pace. Mg, Fe, and Al are crustal elements and their increase could be attributed to increasing events of dust storms. Interestingly, NH_4^{2+}, V, Cr, Cu, Li, Pb, and K^+ decreased in 2012. The increasing events of dust storms may be the reason for this as they increase the crustal elements and subdue other elements.

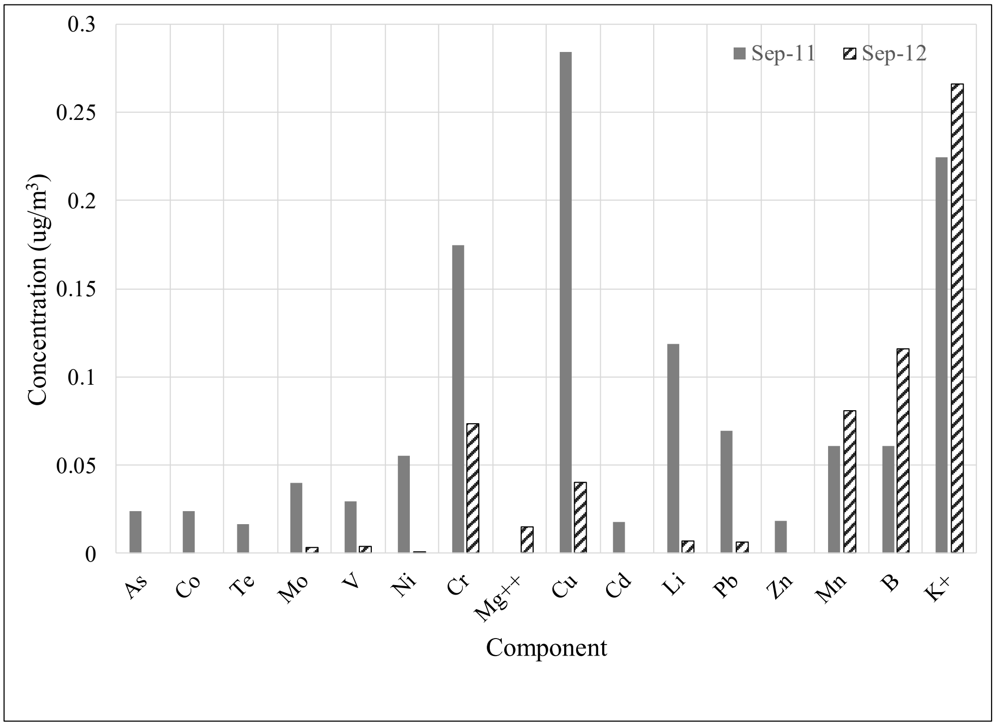

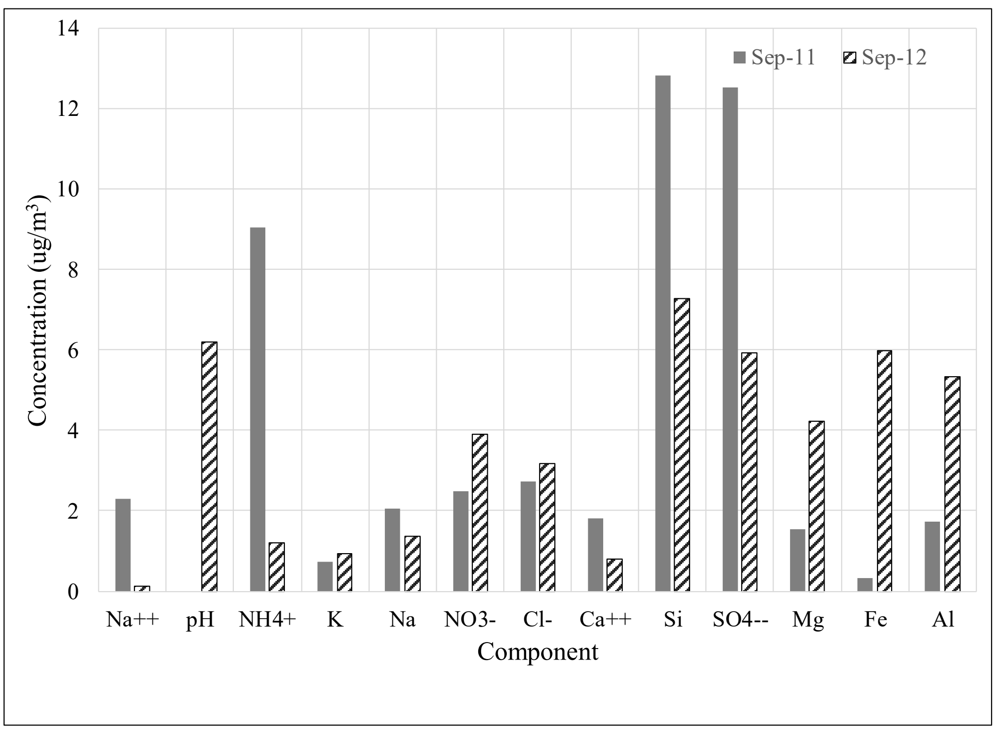

Figure 3.7 Temporal Comparison (Sep 2011 vs. Sep 2012) a) Metals and Ions with Concentration < 0.8 b) Metals and Ions with Concentration > 0.8

3.3.2.1.4 Dust Storm vs. No Dust Storm Days

During study, 15 dust storm events were reported, all of which occurred in the summer. Figure 3.3 presents a comparison between storm and no storm days, and the storm days are double the PM_{10} concentration (over 200% increase). All the ionic concentrations increased during storm days with an exception of NO_3^{2-}, as illustrated in Figure 3.8. Crustal elements such as Al, Fe, Mg, Ca increased significantly during the storms, and this pattern was also reported by other studies (Shen et al., 2009; Shahsavani et al., 2012). The NO_3^{2-} concentrations were not affected by the dust storms, indicating a continuous source, which can be automobile emissions.

3.3.2.2 Spatial Variation

3.3.2.2.1 Industrial vs. Residential Locations

The average of the samples from industrial and residential areas, 35 samples and 71 samples, respectively, were compared to see the variation of PM_{10} concentrations and its composition. The PM_{10} concentrations comparison is shown in Figure 3.3 and the comparison between PM_{10} compositions, metals and ions, is presented in Figure 3.9.

The industrial area was 60% higher in PM_{10} concentrations, showing that industries are major contributors to PM_{10} concentrations. The metals Zn, Mn, B, Mg, Fe, and Al, and the ions K^+, SO_4^{2-}, and Cl^- were higher at industrial locations.

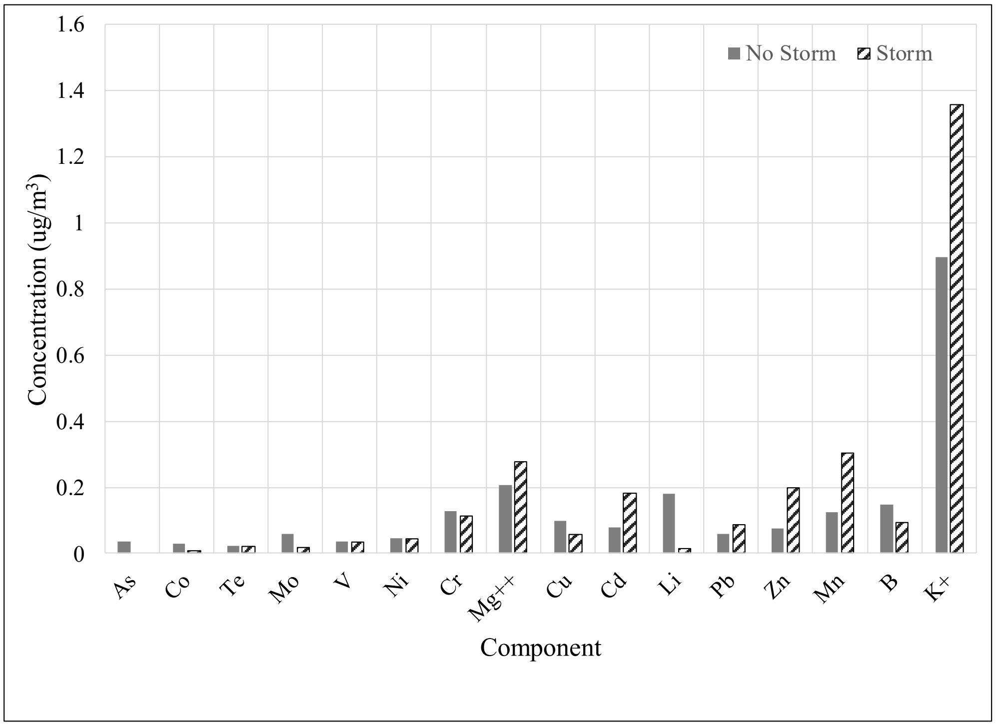

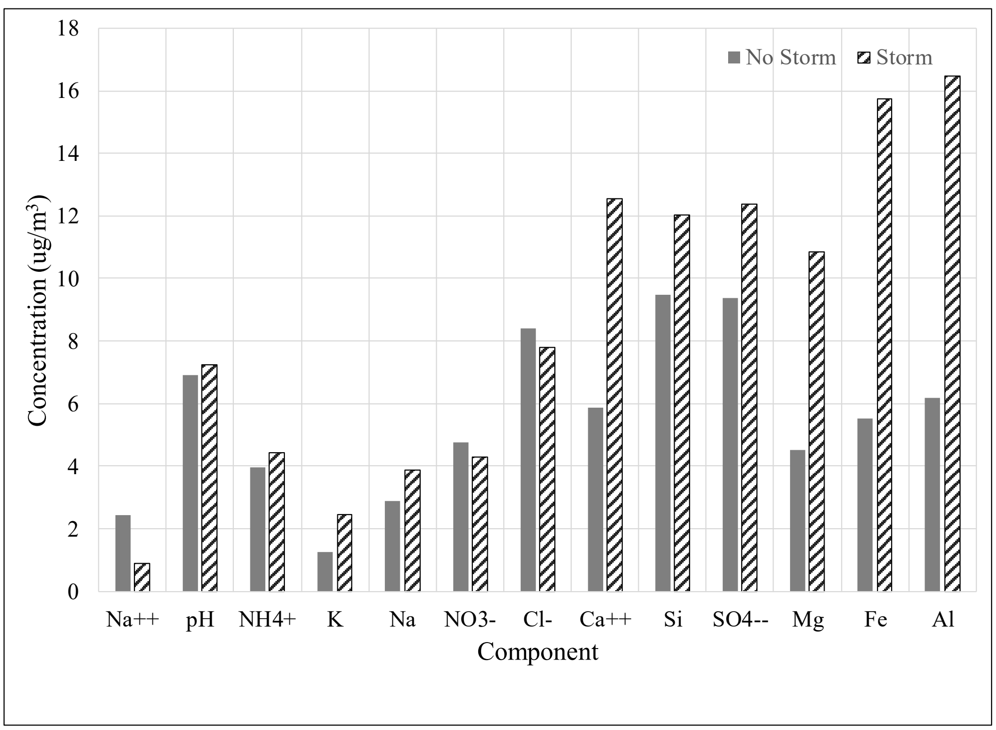

Figure 3.8 Temporal Comparison (Dust storm vs. Normal) a) Metals and Ions with Concentration < 1.4 b) Metals and Ions with Concentration >1.4

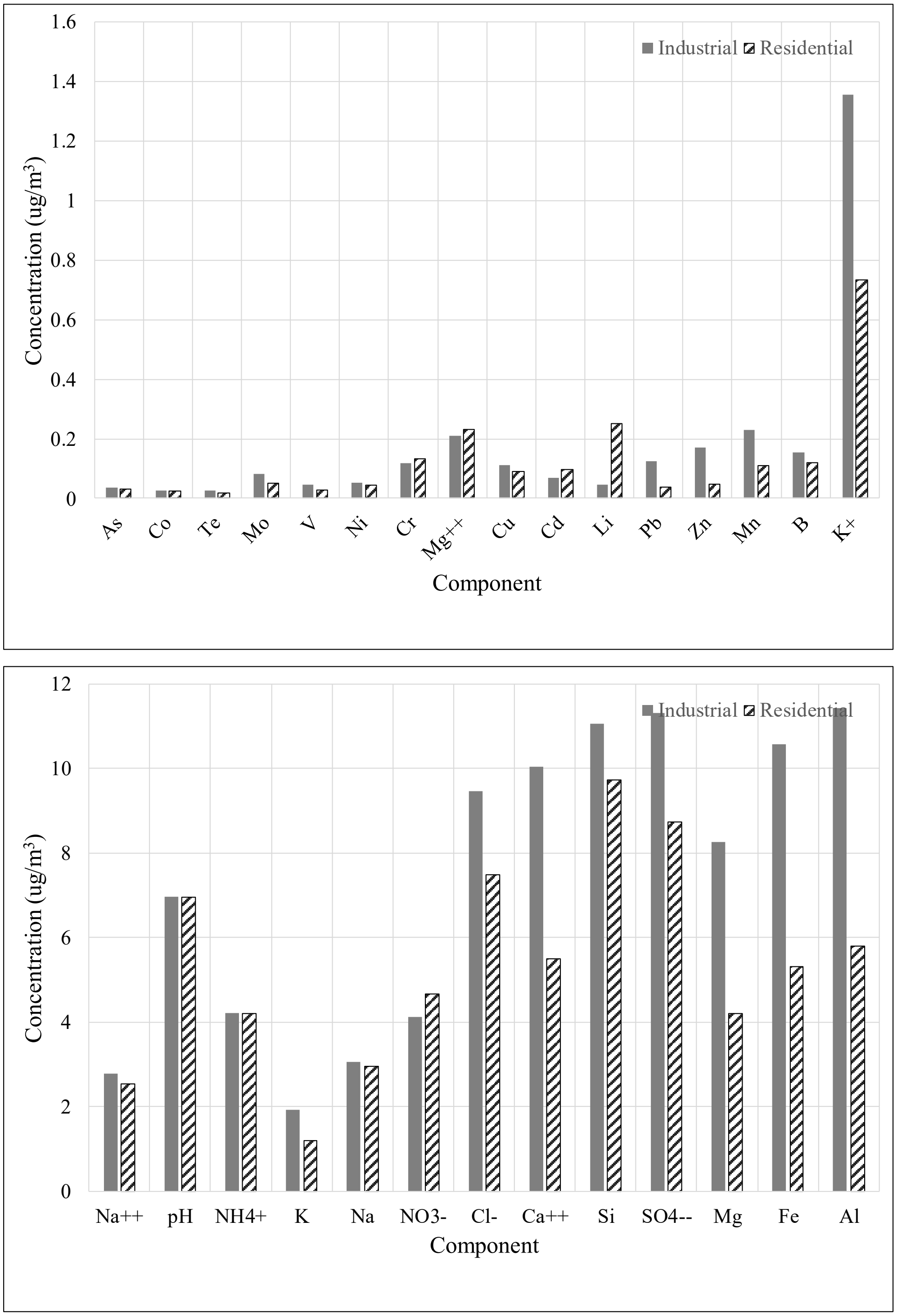

Figure 3.9 Spatial Comparison (Industrial vs. Residential Locations) a) Metals and Ions with Concentration < 1.4 b) Metals and Ions with Concentration >1.4

This increase could be because Riyadh is a metropolitan city and has cement plants, power plants, and a petroleum refinery that generate emissions. The concentration of NO_3^- is higher in the residential areas demonstrating that these are from automobile emissions.

3.3.2.3 Bivariate Analysis

Bivariate correlations were performed among metals, cations, and anions. The correlation coefficients (r) were calculated after establishing the statistical significance of the data as shown in Table 3.5. These coefficients allow obtaining information about the possible common sources. Strong correlations ($r>0.9$) existed between Al, Fe, Mg, K and Mn. This suggests a common origin for these species: the crustal mineral aerosol, as also reported by another study (Contini et al., 2010). Similar strong relationships were found between As, Co, Cd and Li. These metals are most likely of anthropogenic origin, which may be from certain industries in the city. The second level of correlation ($r>0.8$) were found between the heavy metals As, V and Ni, again suggesting their origin could be industries. Strong correlation also existed between V and Te that indicates the presence of the compound vanadium ditelluride in the atmosphere. Vanadium is generally emitted from oil combustion and can be ascribed to the automobile emissions.

Table 3.5 Correlation Coefficients (r) among Metals

	As	**Co**	**Te**	**V**	**Ni**	**Cu**	**Cd**	**Li**	**Mn**	**B**	**K**	**Na**	**Mg**	**Fe**	**Al**
As	1	**0.994**	**0.895**	**0.8187**	0.763	-0.1724	**0.9702**	**0.9727**	0.4433	0.5887	0.2005	0.5049	0.0513	0.0381	0.0903
Co		1	0.6946	0.5546	0.6056	0.2481	0.0703	0.7447	0.0841	0.0489	0.1645	0.4997	0.1856	0.2591	0.2008
Te			1	0.6782	0.6485	-0.1498	0.0385	0.2363	0.4061	0.1775	0.2783	0.1836	0.319	0.3224	0.3132
V				1	**0.8046**	0.2018	0.0397	0.4126	0.6787	0.0866	0.6061	0.0596	0.5772	0.4822	0.5803
Ni					1	0.3284	0.0553	0.6049	0.5526	0.2498	0.4634	0.1511	0.45	0.3428	0.444
Cu						1	0.2685	-0.0211	0.0918	0.1302	-0.1011	-0.1002	0.1744	-0.2885	-0.1837
Cd							1	-0.3389	0.3271	0.512	0.3255	-0.017	0.3046	0.3577	0.337
Li								1	-0.074	0.1653	-0.0014	-0.0622	-0.0336	-0.0229	-0.0136
Mn									1	-0.0628	**0.9569**	0.3545	**0.9745**	**0.9419**	**0.976**
B										1	-0.0023	0.0204	-0.0235	0.0483	-0.0105
K											1	0.4892	**0.9672**	**0.9381**	**0.9726**
Na												1	0.4011	0.3932	0.396
Mg													1	**0.9725**	**0.9894**
Fe														1	**0.9802**
Al															1

To determine the possible chemical forms of the components that might exist in the atmosphere, bivariate correlations were made among cations and anions (Table 3.6). This method was also used by similar studies (Contini et al., 2010; Shahsavani et al., 2012). Correlation between Ca^{2+} and SO_4^{2-} suggests an origin of calcium sulfate, primarily from cement industries. NO_3^- and Cl^- too have a good correlation indicating a possible common origin. These correlations indicate the presence of various chemical compounds that possibly exist in the atmosphere. Examples of such compounds could be $CaSO_4$ (r=0.64 between Ca^{2+} and SO_4^{2-}), $(NH_4)_2SO_4$, (r=0.40 between NH_4^+ and SO_4^{2-}) and to a certain extent KCl, and KSO_4 (r=0.3).

Table 3.6 Correlation Coefficients (r) among Ions

	NO_3^-	Cl^-	SO_4^{2-}
Mg^{2+}	-0.0384	-0.2795	0.2135
K^+	0.1527	0.3442	0.3166
Na^+	0.3221	**0.4839**	0.0373
NH_4^+	0.2592	**0.3312**	**0.4015**
Ca^{2+}	0.1595	-0.0682	**0.6398**

3.3.2.4 Indicators for Various Scenarios

Ratios of ions have been used in many studies to identify possible indicators for relative importance of various sources in the atmosphere (Wang et al., 2005; Shahsavani et al., 2012). To determine the possible indicators, the average of the ionic ratios for all the ions have been calculated for scenarios; industrial vs. residential, storm period vs. no storm period and summer vs. winter. The ratios that had the highest difference between the means were then determined and are presented in Table 3.7.

Table 3.7 Ionic Ratios for Different Scenarios

	SO_4^{2-}/NO_3^-		K^+/Mg^{2+}		Cl^-/NO_3^-	
	Mean	Range	Mean	Range	Mean	Range
Industrial area	5.53	0.75 - 54.30	45.81	1.61 -170.2	4.04	0.61 - 29.47
Residential area	4.50	0.34 - 96.63	2.37	0.99 – 4.73	2.70	0-24 - 34.19
	SO_4^{2-}/Na^+		NO_3^-/Na^+		Ca^{2+}/K^+	
Dust storm days	15.86	15.07- 16.6	7.36	5.36 – 9.49	9.27	5.38 – 13.62
No dust storm days	7.24	0.82- 68.49	3.74	0.01 – 67.42	7.77	0.01 – 25.07
	Ca^{2+}/Na^+		SO_4^{2-}/K^+		SO_4^{2-}/Na^+	
Summer	16.48	2.26 - 75.11	31.26	3.0 - 1167.3	19.57	0.45 - 985.2
Winter	1.39	0.004 – 3.49	17.51	1.43 -128.8	6.89	0.01 -22.4

In case of spatial comparison of industrial and residential location, it was found that the ratios SO_4^{2-}/NO_3^-, K^+/Mg^{2+}, and Cl^-/NO_3^- have the highest differences. The mass ratio of SO_4^{2-}/NO_3^- has been used as an indicator of the relative importance of stationary vs. mobile sources of sulfur and nitrogen in the atmosphere (Arimoto et al., 1996; Yao et al., 2002; Xiao and Liu, 2004). Predominance of sulfate over nitrate in this case can be attributed to the emissions from the stationary sources i.e. industries. With the existence of refinery, power plants and cement factory in the industrial area, the emissions of sulfate and chlorides are obvious. Dominance of nitrate over sulfate can be inferred for the residential areas where the emissions from the automobiles are more.

The ratios for the dust storm days versus no storm days have been evaluated and it was found that SO_4^{2-}/Na^+, NO_3^-/Na^+ and Ca^{2+}/K^+ exhibited highest difference. The ratio Ca^{2+}/Na^+ was also identified to be dust storm indicator by Rushdi et al., (2013) and Shahsavani et al., (2012). It is evident that dust storms increase tremendously the Ca^{++} concentration in the atmosphere.

In order to determine the seasonal identifier, the ratios of ions were calculated for summer and winter. Ca^{2+}/Na^+, SO_4^{2-}/K^+, and SO_4^{2-}/Na^+ have the highest difference; this is almost similar to the dust storm identifiers as the dust storms occur mostly in summer season. The presence of sulfate as indicator can be ascribed probably to the increasing industrial activity in summer season.

3.3.3 O_3 and NO_x

3.3.3.1 O_3 and NO_2 Concentrations Compared to Standards

The prescribed 1-hour and 8-hour PME standards for O_3 were 120 ppb and 80 ppb respectively, and 1-hour standard for NO_2 was 350 ppb. In order to study the spread of the data, hourly O_3 and NO_2 concentrations are presented as boxplots in Figure 3.10.

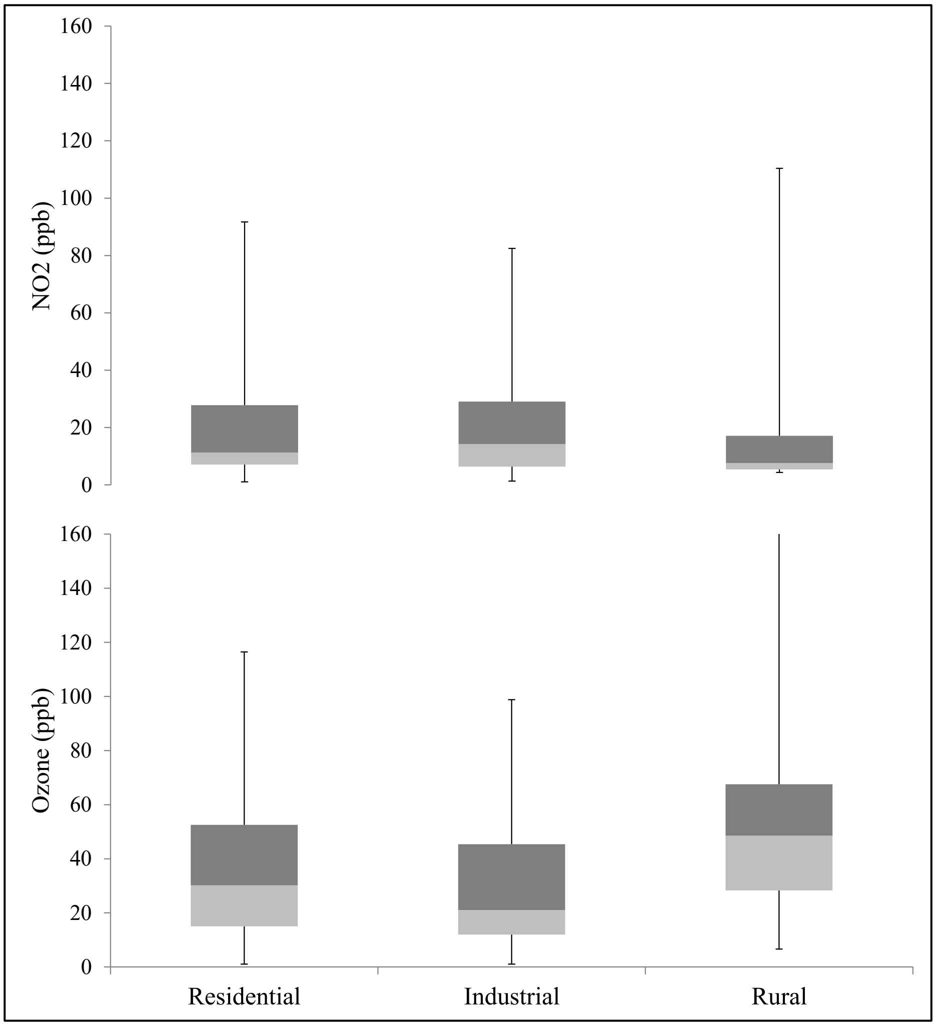

Figure 3.10 Boxplots of O_3 and NO_2 Concentration at Residential, Industrial, and Rural Locations

As shown in the figure, 75 percentile O_3 concentrations (ppb) were in the range of 60-75, 30-55, and 20-40 for rural, residential, and industrial locations respectively. O_3 concentrations were observed as relatively high in the rural location followed by the residential and then the industrial locations.

For NO_2, the 75 percentile concentrations (ppb) were in the range of 20-35, 15-30, and 10-15 for the industrial, residential, and rural locations respectively, as shown in Figure

3.10. Higher concentrations of NO_2 in the industrial locations relative to other locations imply that there are industrial emissions of NO_x in addition to automobile emissions. These relatively higher NO_x concentrations keep O_3 levels low. At all the locations, the NO_2 concentrations stayed below the PME standards (350 ppb).

Table 3.8 displays the percentage frequency of O_3 concentrations for the three locations. As shown in the table, at the residential location about 15% of O_3 concentrations exceeded 80 ppb, about 2% exceeded 100 ppb, and about 1% exceeded 120 ppb (1-hour O_3 PME standards). The industrial locations had very few exceedances of 80 ppb and no exceedances of higher. However, the rural locations reported that over 2% exceeded 120 ppb, in addition to a large number of concentrations above 80 ppb. Figure 3.11 shows the average O_3 concentrations at the three locations compared with neighboring cities. As illustrated, the average concentrations of O_3 at all three locations in Riyadh exceeded its neighbors. Overall, the O_3 concentrations at all three locations were barely within the PME standards; however, they exceeded the 1-hour limits a few times during the sampling period.

Table 3.8 Percentage Frequency Distribution of Hourly Mean O_3 Concentration at Residential, Industrial, and Rural Locations

Site	0-20	20-40	40-60	60-80	80-100	100-120	>120
Residential	11.19	24.19	26.35	22.74	14.08	1.44	0.00
Industrial	30.25	24.38	25.62	16.36	3.40	0.00	0.00
Rural	0.90	7.62	33.18	39.91	15.70	0.45	2.24
Total	14.11	18.73	28.38	26.34	11.06	0.63	0.75

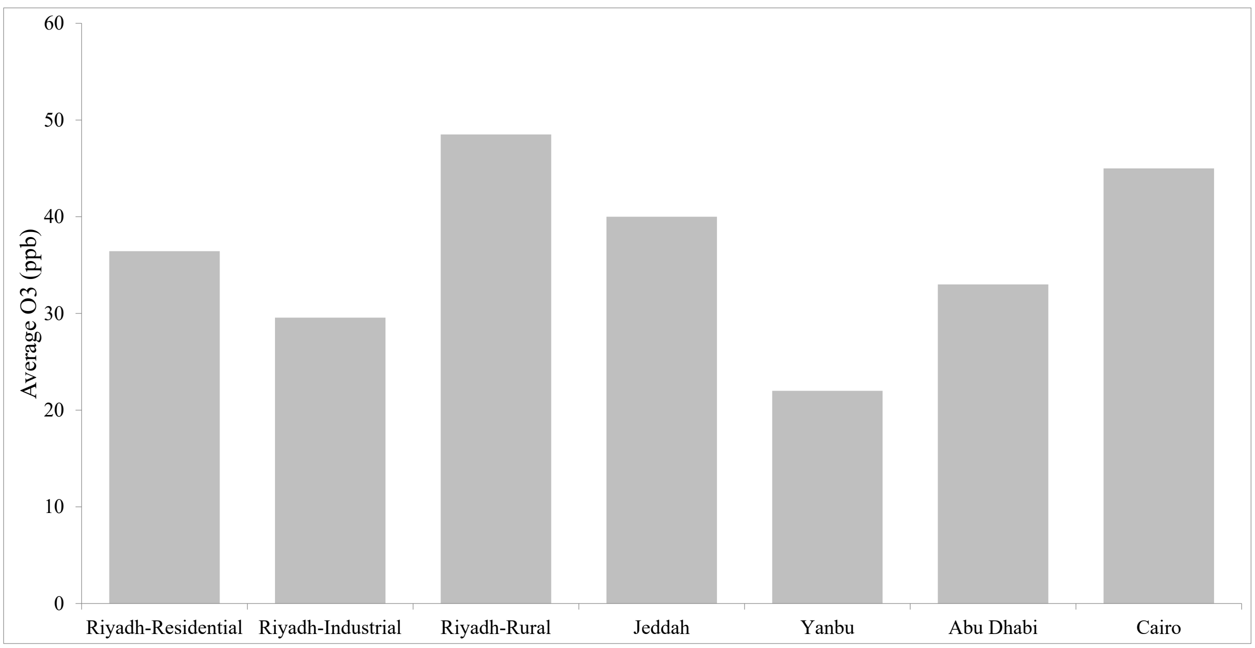

Figure 3.11 Average Daily Levels of O_3 Concentration at Riyadh along with Values at Selected Cities

3.3.3.2 Diurnal Variation NO, NO_2, NO_x, and O_3

Figure 3.12 illustrates the diurnal patterns of NO, NO_2, NO_x, and O_3 concentrations at the residential, industrial, and rural locations. The diurnal pattern of the primary pollutant NO at residential and industrial sites followed a double peak: one in the morning and the other in the evening. The morning peak occurred at around 06:00-07:00 local time (LT) coinciding with rush hour traffic. The average peak concentrations in the residential and industrial sites were 32 ppb and 53 ppb respectively. After rush hour, the NO steadily decreased in the day indicating the photochemical conversion of NO to NO_2 until late in the evening where it peaked again at around 19:00-20:00 LT. The evening peaks in the residential and industrial areas were 18 ppb and 34 ppb respectively. Nighttime NO concentrations remained steadily low. As noted, the NO concentrations at the industrial locations were slightly higher than the residential. The NO concentrations at the rural site remained low during the day and peaked in the early morning to 23 ppb, and this surge of NO appears to be coming from the industrial and residential concentrations due to wind conditions (as depicted in Figure 3.2).

The NO_2 concentrations showed a similar pattern to NO; however, both the morning and evening peaks had a lag time of 1-hour with respect to NO. This lag time can be explained by the photochemical reaction, which converts NO to NO_2. The morning and evening peaks were around 25 ppb and 20 ppb respectively, at all locations. Both residential and industrial locations showed similar patterns and magnitude.

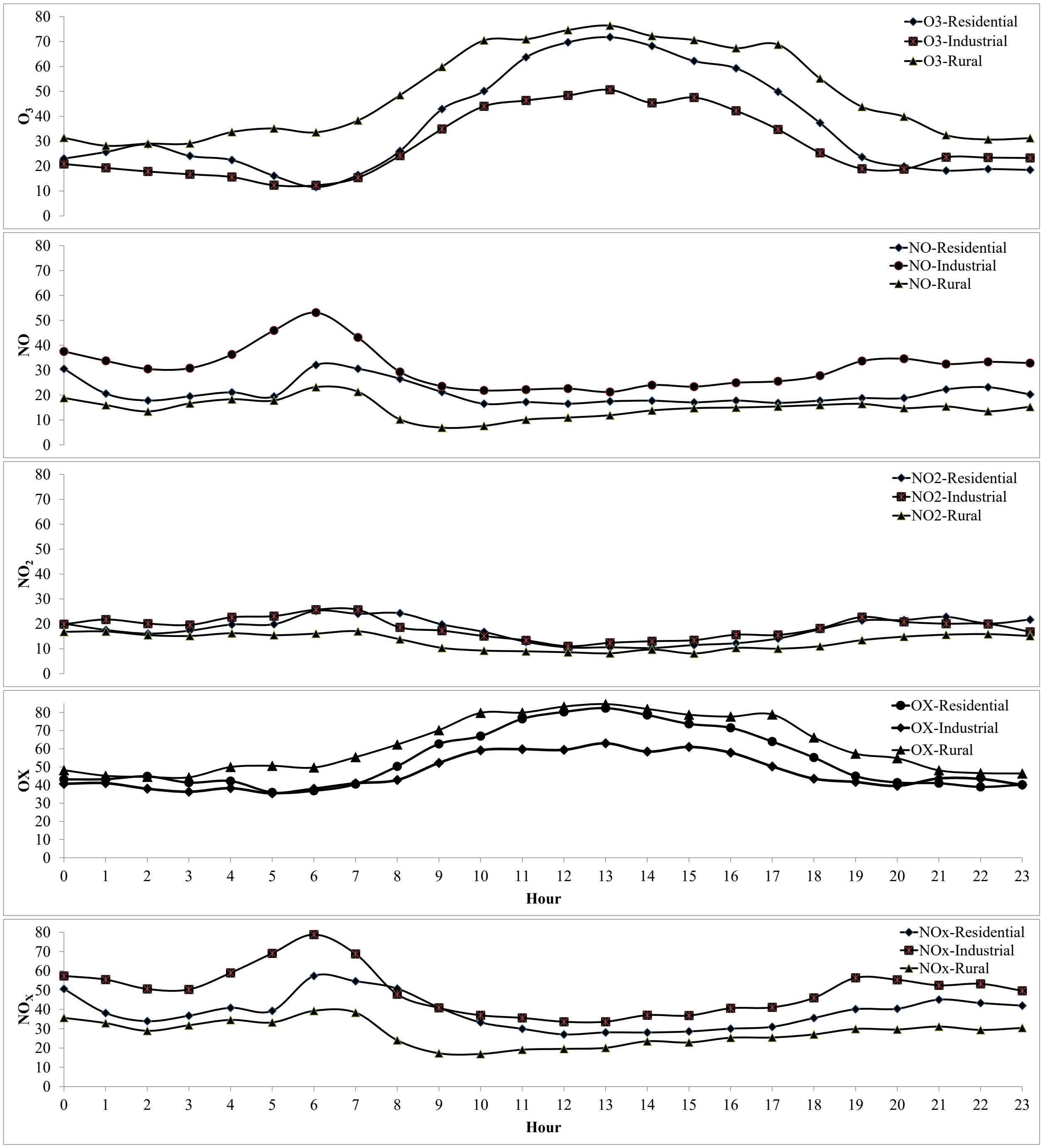

Figure 3.12 Diurnal Variation of Average NO, NO_2, NO_x and O_3 Concentration (ppb) at Residential, Industrial, and Rural Locations

The rural site showed high concentrations of 17 ppb in the morning, then, it dropped to 8 ppb at noon, and, increased slightly through the evening. The NO_2 concentrations were lower at the rural location. Higher NO and NO_2 concentrations at the industrial location may be caused by the industries, especially the petroleum refinery, and traffic emissions.

The concentrations of NO_x in the rural location were very low, at 15 ppb, and remained steady throughout the day. However, in the residential and industrial locations, it followed NO and NO_2 patterns with their double peaks. The industrial location had higher concentrations than the residential location with morning and evening peaks of 80 ppb and 60 ppb respectively. The residential location peaks in the morning and evening were 60 ppb and 45 ppb respectively.

The daily variation of O_3 concentrations is influenced by traffic emissions, photochemical activity, and the height of the planetary boundary level, as also reported by other studies (Jenkin and Clemitshaw, 2000; Han et al., 2009; Notario et al., 2012). The O_3 concentrations gradually increased after sunrise, reached their maximum at noontime, decreased towards sunset, and remained low throughout the night. The daily peak occurred around noontime at the rural location and at 13:00 (LT) at both the residential and industrial locations. A consistent 1-2 h lag between the rural and residential locations was observed. The highest O_3 concentrations were observed in the rural locations followed by the residential and then the industrial. High rural concentrations can be explained by the transport of NO_2 and mixing of air masses due to meteorological conditions; this has also been reported in other regions (Geng et al., 2008; Notario et al., 2012; Han et al., 2013).

Studies have been done to analyze O_3 and its precursors in the Arabian region, (Khoder, 2009; Porter et al., 2014; Al-Jeelani, 2014) but none of the studies explain the early morning O_3 loss. As observed from Figure 3.12, there is a reduction of O_3 early in the morning. This early morning O_3 loss can be explained as follows. The source of NO is primarily in the residential and industrial locations; this NO reacts with O_3 to form NO_2 (Eq. 2.3), resulting in the reduction of O_3 concentrations. Since sunlight is low in the early morning, there is little photochemical breakdown of NO_2 and this newly formed NO_2 is transported over to the rural locations. Photochemical activities increase with sunlight, thus NO_2 acts as an agent for the increase of rural O_3 concentrations (Eqs. 2.1-2.2). The transport of NO_2 from residential and industrial areas to the rural areas is evident from the wind rose diagram (Figure 3.2). This can also be explained by calculating O_3 tendency ($d[O_3] = O_3[t+1] - O_3[t]$). Figure 3.13 illustrates the O_3 tendency for the three locations. The positive values of O_3 tendency indicate that the O_3 chemical production becomes a dominant factor in controlling O_3 concentrations, while negative values mean O_3 destruction plays a major role. As seen in the figure, negative O_3 tendency is observed in the residential location at early morning while positive tendency is noticed at the rural location at the same time.

The diurnal variation of the NO_2 photolysis rate per minute (J1), calculated based on Eqs.3.1 and 3.2, at the three locations is shown in Figure 3.14.

$$\frac{[NO][O_3]}{[NO_{2]}} = \frac{J_1}{K_3} \tag{3.1}$$

$$k_3(ppm^{-1}min^{-1}) = 3.23\ x\ 10^3 \exp[\frac{-1430}{T}] \quad (3.2)$$

NO_2 photolysis rates follow the O_3 formation pattern for all three locations. The highest/lowest photolysis rates (min^{-1}) in the rural, residential, and industrial locations were 4.56/0.74, 4.29/0.45, and 3.54/0.70 respectively

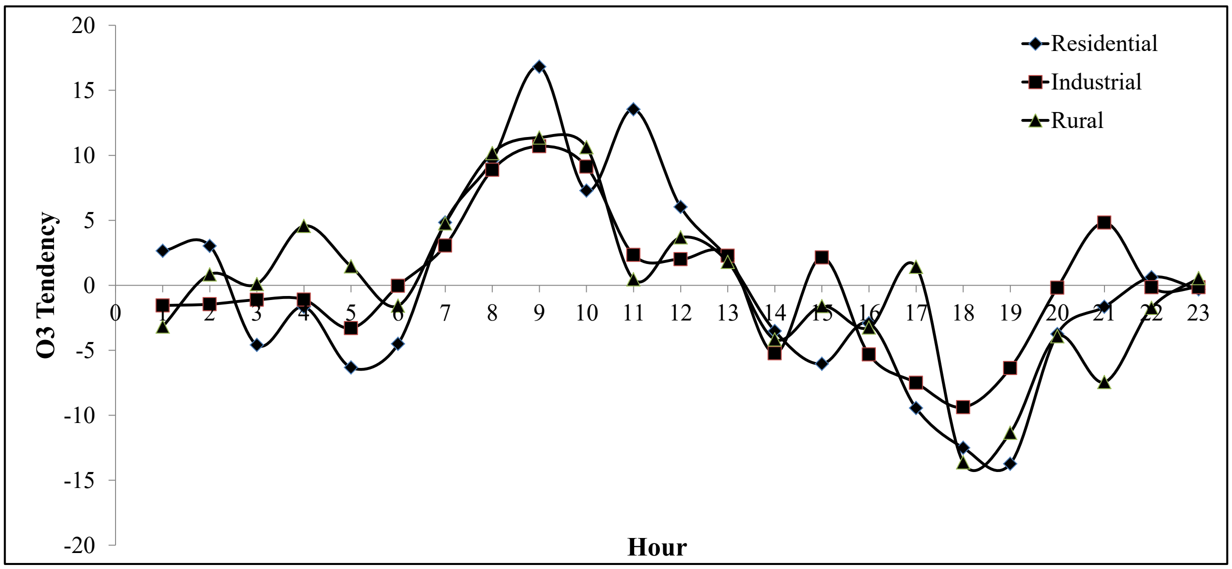

Figure 3.13 Daily Variation of O_3 Tendency at Residential, Industrial, and Rural Locations

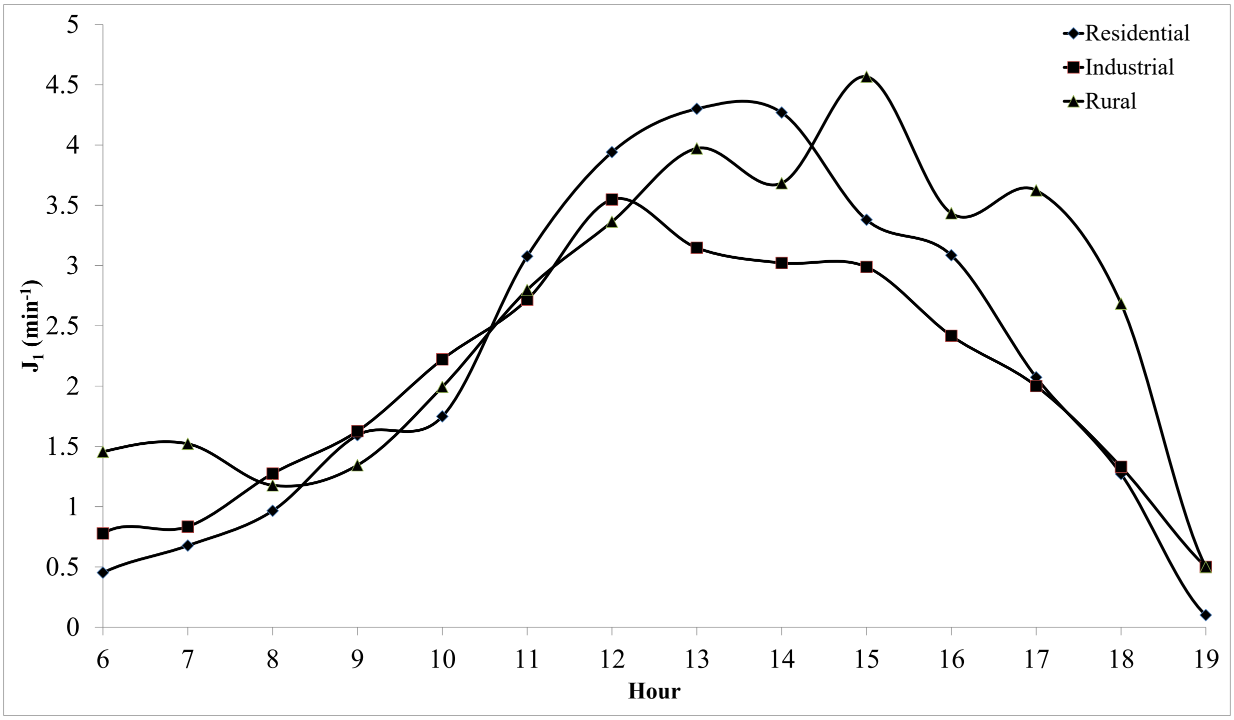

Figure 3.14 Daily Variation of Mean Values of J_1 (min^{-1})

. These values are 3-4 times higher than that of a similar study (Notario et al., 2012). These relatively excessive photolysis rates can be attributed to the high solar radiation in Riyadh. An early morning high NO_2 photolysis rate at the rural locations presents another reason for early morning O_3 loss at residential locations.

3.3.3.3 Relationship between NO, NO_2, NO_X, and O_3

Figure 3.15 illustrates the scatter plots of NO, NO_2, and O_3 versus NO_x along with the fitted polynomial curves for daytime and nighttime. Due to photochemical activity in the day, it is expected that the daytime pattern should be different from nighttime. Daytime is considered from 07:00 LT to 18:00 LT and nighttime from 19:00 LT to 07:00 LT, based on the data collection period.

As depicted in the figure, during the daytime, there is a tendency of O_3 to decrease with NO_x, and the dispersion is large at the lower NO_x concentrations. As the photochemical activity recesses during nighttime, O_3 concentrations remain constant despite increase in NO_x. A strong negative correlation was observed between NO_x and O_3 values in the industrial locations, while a weak correlation was noticed in the residential and rural locations. This indicates that the photochemical activities around the industrial locations were higher, potentially due to the greater emissions of NO_x from traffic and industries in the area. In the rural locations, there was a large dispersion in O_3 concentrations, however, lower concentrations are observed when NO_x values are high.

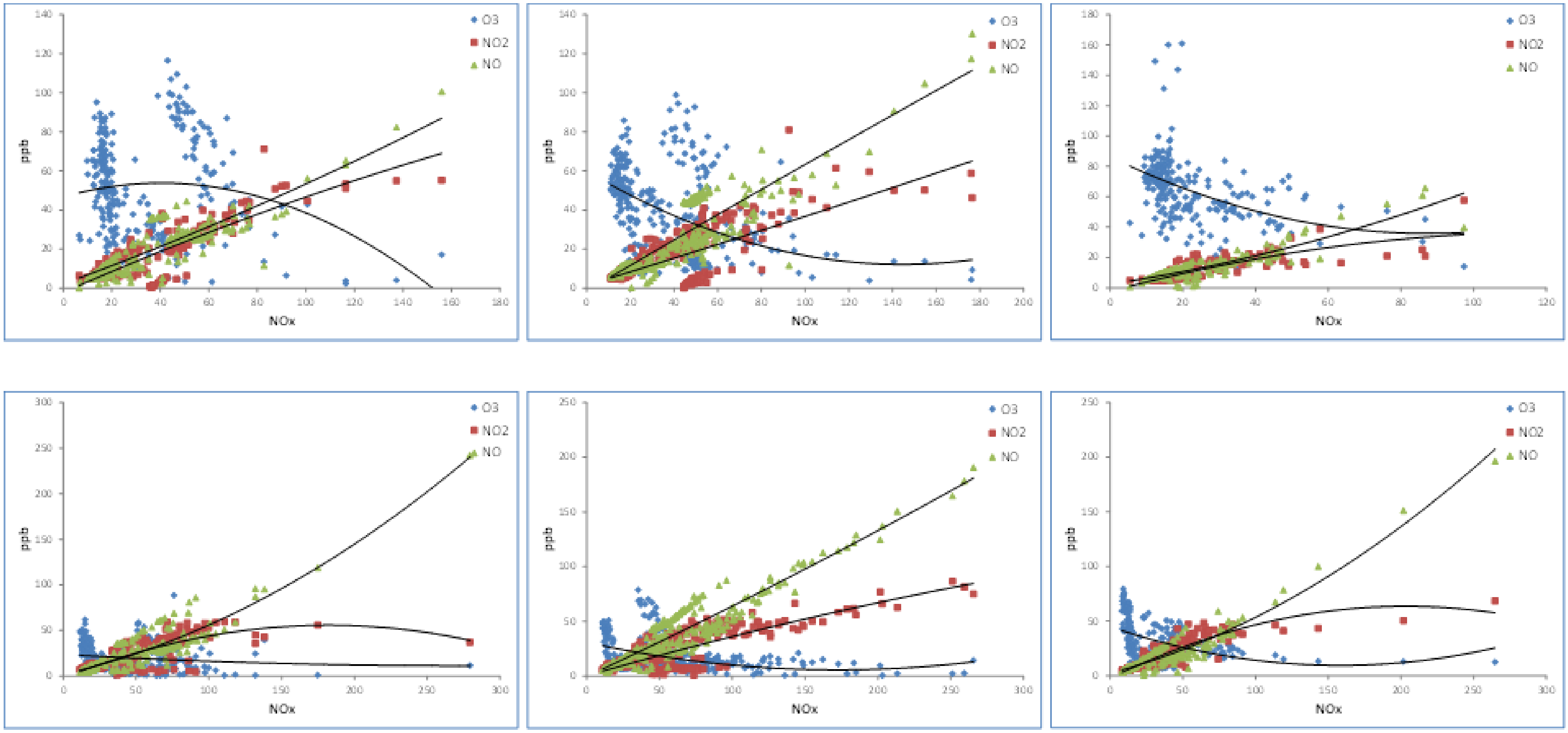

a) Residential b) Industrial c) Rural

Figure 3.15 Variation of NO, NO_2, and O_3, Versus NO_x Concentrations and Polynomial Fit Curves during Day (top) and Night (bottom) for Residential (a), Industrial (b) and Rural (c) Locations

The maximum NO, NO_2, and O_3 concentrations during daytime/nighttime observed in the residential locations were 100/119 ppb, 71/60 ppb, and 116/88 ppb, the maximum concentrations in the industrial locations were 130/190 ppb, 81/86 ppb, and 98/78 ppb, and in the rural locations they were 65/196 ppb, 57/68 ppb, and 160/80 ppb respectively. In view of these results, we can infer that the NO concentrations were observed higher during the night in the industrial location and that day and night showed similar NO_2 concentrations at all locations.

A polynomial fit was found suitable for the NO, NO_2, NO_x, and O_3 scatter plots as shown in Figure 3.15. The photo-stationary state of NO_x concentrations can be inferred from these curves. During the day, the NO_x concentrations for NO and O_3 intersected at 66 ppb, 55 ppb, and 62 ppb for residential, industrial, and rural locations, respectively. This implies that at these NO_x concentrations, O_3 concentrations are higher than NO values, whereas NO concentration exceeds O_3 at higher NO_x levels. For example, at the residential site at the concentration of NO_x equal to 66 ppb, O_3 concentrations were higher than NO, however O_3 concentration decreases with the NO_x value greater than 66 ppb.

Similar analysis of NO, NO_2, NO_x, and O_3 scatter plots was performed for the NO_2 and O_3 intersects. During the day, the NO_x concentrations observed were 77 ppb, 77 ppb and 65 ppb for residential, industrial, and rural locations respectively. In this case, similar behavior is observed for industrial and residential locations while NO_x intercept is lower for the rural location. The patterns of O_3 and its precursor discussed here match with other studies (Clapp and Jenkin, 2001; Mazzeo and Venegas, 2005; Notario et al., 2012), however, the concentrations are higher in this study.

3.3.3.4 NO_x Dependent and Independent Contributions

NO_x independent contribution means the regional contribution and NO_x dependent means to the local contribution. The local and regional contribution of OX (O_3+NO_2) can be identified from the regression analysis of NO_x and OX, where the slope indicates the local OX contribution and the intercept represents the NO_x independent regional contribution. Figure 3.16 shows the variation of the average OX concentration with respect to the NO_x levels as observed during day and night in the three different locations.

In the residential locations, the slope of the curve was slightly higher during day compared to night. This implies that there was an increase of NO_x emissions in the day, evidently from daytime activities; however, there were sources emitting NO during night. In the industrial locations, the slope was lower during the day when compared to night implying that there were high NO emissions during the night. A large number of industries including oil refining could be the potential sources. In the rural locations, almost no local emissions were observed; this is in line with the characteristics of the area as traffic emissions are negligible. However, there was an increase of NO concentrations in the night, most probably buildup from nearby residential and industrial areas.

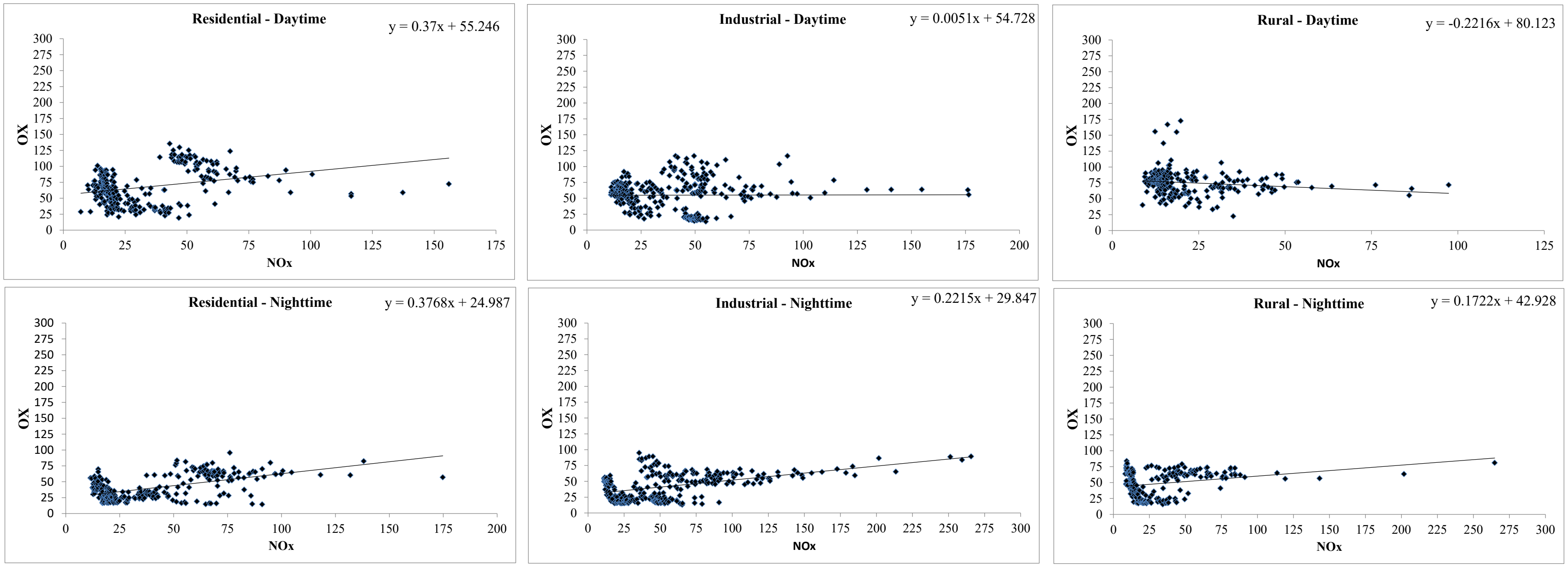

Figure 3.16 Regression Analysis of NO_x vs. OX for Day (Top) and Nighttime (Bottom) at Residential, Industrial, and Rural Locations

The intercept during the day was generally greater than that of night indicating that there was a large NO_x independent regional contribution. In addition, it was noticed that there were higher intersect values in the rural locations indicating that the regional contribution was a major source there. It is implied from the above discussion that that NO_x independent contribution was generally greater indicating larger contributions from NO_x independent sources. While there is the possibility of regional contributions, it is highly likely that these NO_x independent contributions were from VOCs in the atmosphere, which interferes in the photochemical cycle (Eqs.3-3 and 3-4).

$$O + H_2O \rightarrow OH + OH \tag{3.3}$$

$$RH + OH + NO \rightarrow RCHO + HO_2 + NO_2 \tag{3.4}$$

3.3.3.5 Weekend vs. Weekday

The average diurnal difference between weekend and weekday concentrations of NO, NO_2, and O_3 were calculated for the three locations as plotted in Figure 3.17. It shows that the difference is positive for O_3 and negative for NO and NO_2. The reduction of NO concentrations during weekend is manifestly due to reduction of traffic emissions. In the residential area, weekend NO concentrations were observed to be lower in the morning, however, increased during the evening and night contrary to other studies (Debaje and Kakade, 2006; Khoder, 2009; Han et al., 2011). This pattern probably reflects the local traditions of the city where there are increased weekend activities in the evenings.

In the industrial locations, there was a distinction between weekend and weekday NO concentrations during corresponding times of the day. There were consistent negative differences of NO concentration all over the day, indicating that during weekend there is a considerable reduction of traffic emissions as well as emissions from industries.

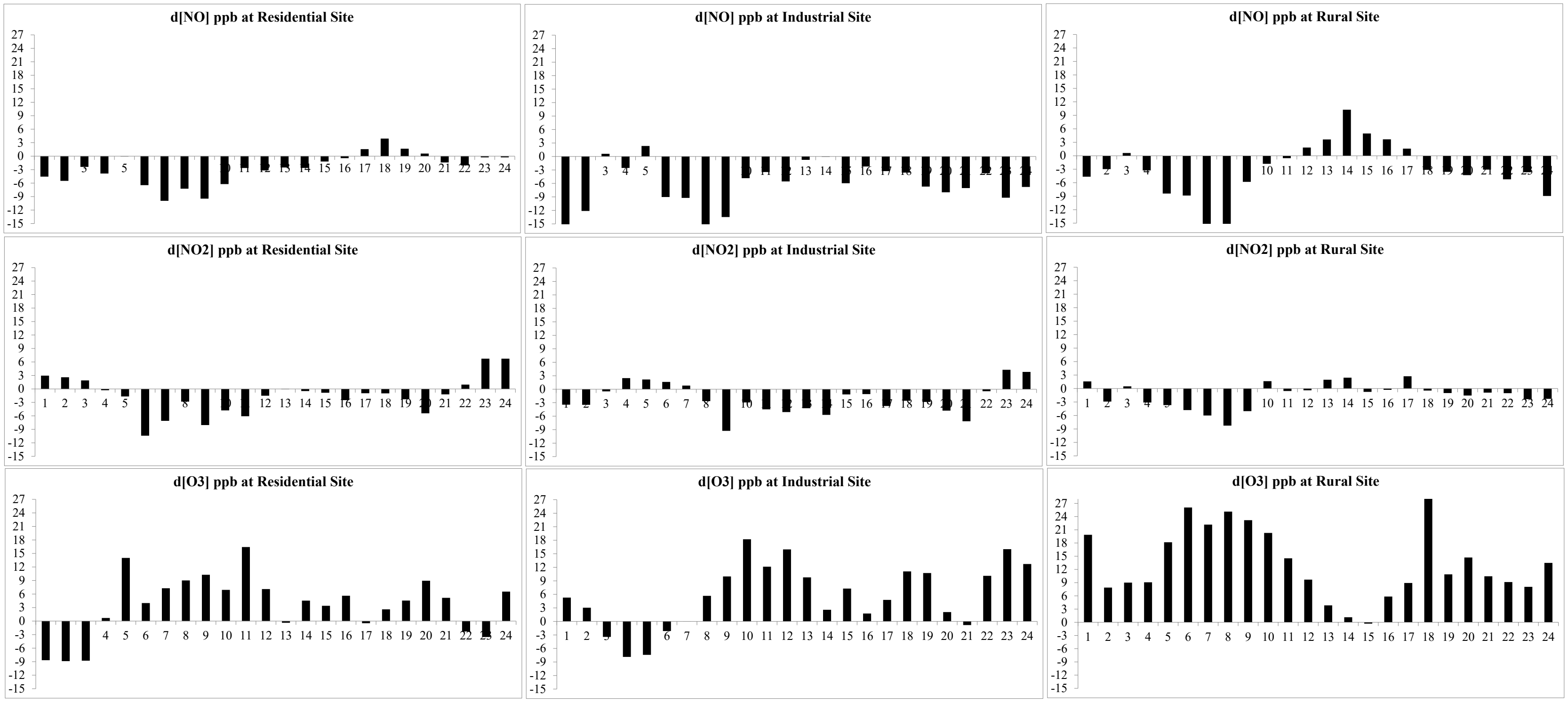

Figure 3.17 Diurnal Weekend and Weekday Differences of NO, NO_2, and O_3 Concentrations at Residential, Industrial, and Rural Locations Averaged during the Sampling Period

Most of the industries work full scale during weekdays and have reduced activities during weekends. It implies that NO concentrations are primarily due to traffic emissions, though contribution from the industries is not negligible. The maximum weekend-weekday difference of NO at the residential, industrial, and rural locations were 10 ppb, 16 ppb and 15 ppb respectively. These differences are higher than other studies (Geng et al., 2008; Khoder, 2009; Han et al., 2013) indicating increased levels of automobile pollution in Riyadh.

The gain of O_3 concentrations during weekend is generally called the weekend effect. The reasons for this effect are the sensitive relation of O_3 formation to VOCs, difference in timing of NO_x emissions, carryover of O_3 and its precursors' concentration from the day before the weekend, and increased weekend emissions (The Research Division, California Air Resources Board, 2003). This weekend effect could be explained for Riyadh as follows. The NO_2 concentration is consistently low during the day indicating that NO_2 chemically reacts resulting in an increased production of OH (Eq. 3-3). The OH radical then reacts with VOCs (Eq. 10) present in the atmosphere converting NO to NO_2. This NO_2 facilitates the formation of O_3 (Eqs. 2-1 and 2-2), thus resulting in the build-up of O_3 concentrations during weekends.

3.4 Summary

This chapter presented details regarding the data collection and analyses for the purpose of developing and validating of the objectives of this research. Riyadh was divided into 16 grids and several air quality parameters (including primary and secondary pollutants) were collected from the center of each grid for a period of one year. Grids were mainly classified as industrial (predominantly industries in the area) and residential (largely residential areas).

Particulate matter samples were analyzed for several metals and ions. PM_{10} concentration was approximately 3 times higher than the Country's ambient air quality standards respectively. Metals and ions contributed to about 21.5% and 16.2% of the PM_{10} concentrations respectively. Summer vs. winter comparison showed that PM_{10} concentrations were approximately 84% higher in summer and the crustal matter species such as Fe, Mn, Ti, Ca^{++}, Mg^{++} increased several folds in summer, primarily attributed to dust storms. The weekdays PM_{10} concentrations were 17% more than the weekend concentrations, indicating weekday activities contributes to the concentrations. Events of the dust storms lead to over 200% increase in the PM_{10} and some metals elements primarily Al, Fe, Mg and Ca. Spatial comparison at industrial and residential locations revealed about 60% increase in PM_{10} concentrations and substantial increase in Zn, Mn, B, Mg, Fe, and Al and the ions K^{+}, SO_4^{--}, and Cl^{-} at industrial locations. Bivariate correlations among the metals and ions demonstrated that strong correlation existed between Al, Fe, Mg, K, and Mn suggesting a common origin for these species i.e. the crustal mineral aerosols. The correlations among cations and anions implied the presence of chemical compounds in the atmosphere such as $CaSO_4$, $(NH_4)_2SO_4$, KCl, KSO_4, and to some extent $MgSO_4$. An investigation of ionic ratios revealed that ratios SO_4^{--}/NO_3^-, Ca^{++}/K^+, and Ca^{++}/Na^+ could be possible indicators to identify scenarios industrial over residential locations, storm days over no storm days and summer over winter periods respectively.

During the sampling period O_3, concentrations exceeded 1-hour local standards a few times yet remained within the standards most of the time. The O_3 concentrations were observed highest in the rural location and lowest in the industrial area. The diurnal variation of NO followed a double peak: one in the morning and the other in the evening, representing the traffic pattern. Early morning NO peaks were observed in the rural location, which were attributed to the movement of NO from other locations. The O_3 concentrations depicted typical pattern, increasing after the sunrise and reaching its maximum during midday. The highest O_3 concentrations were observed in the rural location followed by the residential and industrial areas. NO_2 photolysis rates were 3 to 4 times higher compared to other similar investigations, potentially due to intense solar radiation. A strong negative correlation was observed between NO_x and O_3 values in the industrial location indicating photochemical activities around the industrial area were higher, likely due to additional NO_x emissions from industries. Regression analysis of NO_x and OX ($O_3 + NO_2$) indicated that in residential and industrial locations during night, there are large NO_x independent regional contributions attributed to role of VOCs. Weekend effect was observed in the city potentially due to the production of OH radical and subsequent reaction with VOCs.

CHAPTER 4: MODEL SETUP AND BASE CASE SIMULATION

Photochemical air quality modelling (PAQM) is a complex process that involves meteorological and emissions modelling and in particular captures the appropriate chemical mechanisms, as illustrated in Figure 2.4. Each of the used models and their relationship to PAQM are shown in Figure 4.1. This chapter discusses the settings used in the models, base case simulation, and the comparison of the simulation results with the observed data.

4.1 Meteorological Modelling

Meteorology drives any chemical transport model and so generating an accurate meteorological dataset is very important for reliable air quality predictions. There are many weather forecasting models, among which, the Weather Research and Forecasting model (WRF) has been commonly used for air quality modelling. WRF is a next-generation, mesoscale, numerical weather prediction system designed for both atmospheric research and operational forecasting needs (The Weather Research and Forecasting Model, 2016). WRF version 3.4.1 (the version used for modelling) is a prognostic meteorology model developed in partnership by the National Center for Atmospheric Research, the National Oceanic and Atmospheric Administration, the Air Force Weather Agency, the Naval Research Laboratory, the University of Oklahoma, and the Federal Aviation Administration. This is a hydrostatic, terrain-following, eta-coordinate model designed to simulate or predict mesoscale and regional-scale atmospheric circulations. WRF was primarily developed using FORTRAN coding, and is used as a community model in over 150 countries and updated on an annual basis.

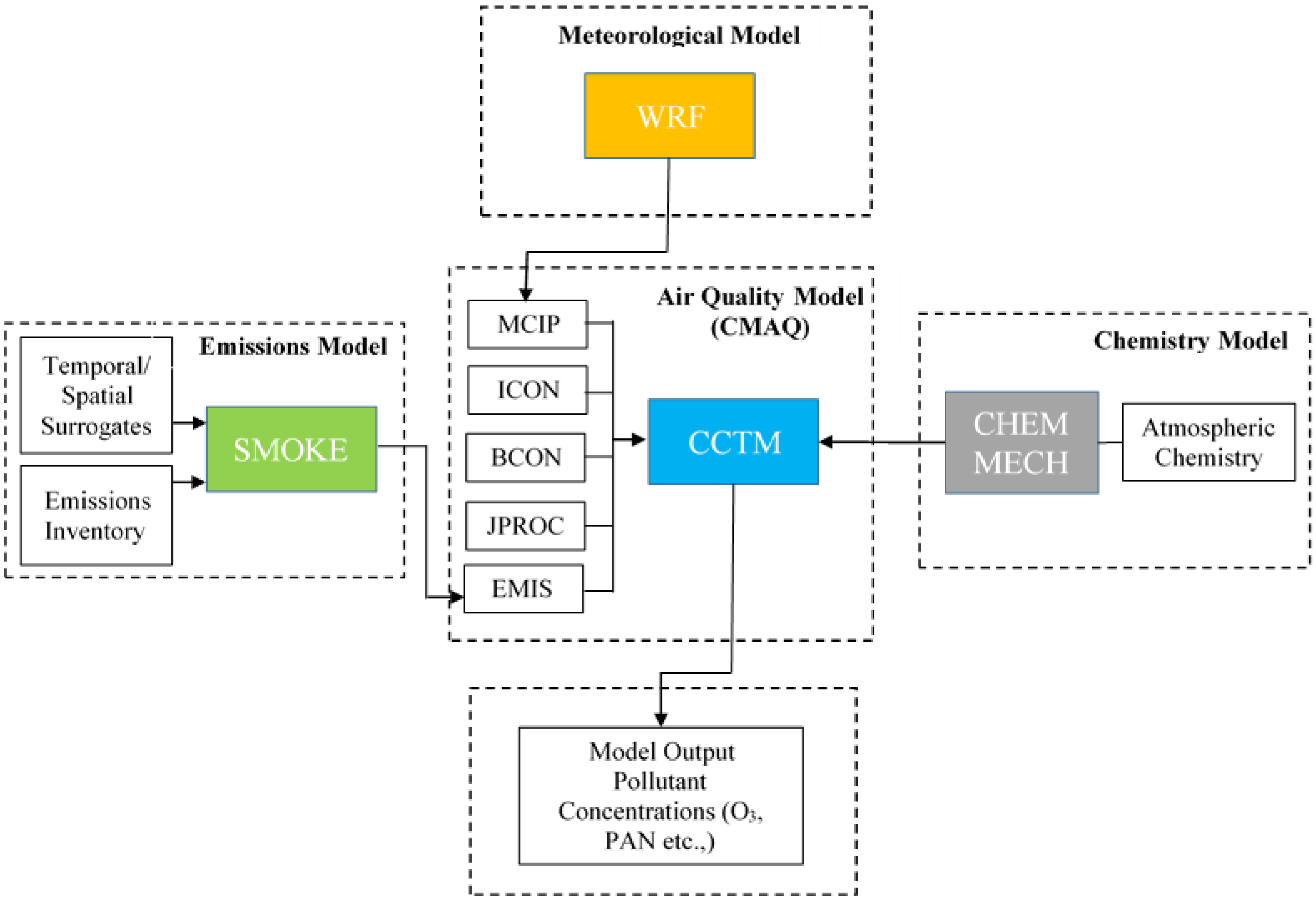

Figure 4.1 Schematics of Air Quality Modelling System

WRF was run for the year 2012 over the domain shown in Figure 4.2. The domain chosen centered at Riyadh. The dimensions of the domain were approximately 300 km x 300 km and the resolution was 4 km. This resulted in 78 x 78 grid points as shown in Figure 4.2.

Terrain elevations and land-use categories needed by the WRF model were taken from United States Geological Society (USGS) datasets archived at the National Center for Atmospheric Research (NCAR). The terrain data and roughness length varied within each grid cell. Typical roughness length values used were 0.0002 m for the open sea and 0.03 m for open flat terrain. During the model runs, WRF used two-way nesting, which generally produces higher accuracy results for the child domain. Two-way nesting averages values of the child domain for grid points covered by a single parental grid point and then replaces that parental grid point value with the averaged value. WRF was initialized with data from the Global Forecast System (GFS), a worldwide numerical weather prediction model operated by the U.S. National Weather Service. WRF also ingested daily sea-surface temperature analysis data provided by the U.S. National Oceanic and Atmospheric Administration at a resolution of 0.083°. WRF was run for 54 hours per run, discarding the first six hours of model output due to model spin-up. This provided high-density, three-dimensional meteorological data for the air quality model. The summary of the physics options implemented in the WRF modelling are shown in Table 4.1.

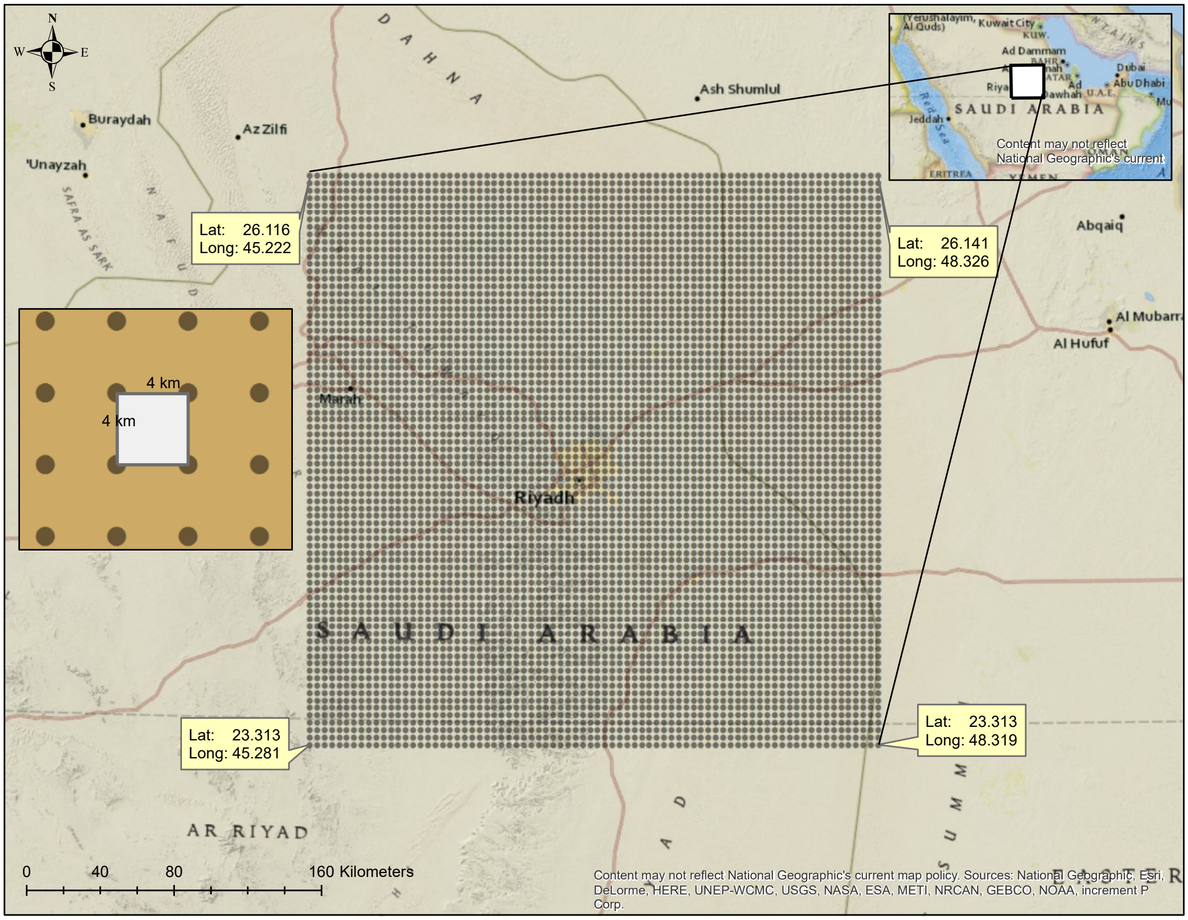

Figure 4.2 Modelling Domain and Grid Points

Table 4.1 WRF Physics Options

Physics Options	Option Chosen and Details
Cumulus Clouds	Kain-Fritsch scheme
Planetary Boundary Layer (PBL)	Mellor-Yamada-Janjic scheme
Moisture Scheme (Microphysics)	WRF Single-Moment 5-class scheme
Radiation Scheme	Rapid Radiative Transfer Model
Surface Clay	Noah Land Surface Model
Surface Scheme	Monin-Obukhov similarity theory.

Meteorology-Chemistry Interface Processor (MCIP)

The meteorological output generated by WRF is not readily compatible with the emissions and air quality modelling software SMOKE and CMAQ-CCTM respectively (as discussed in the following sections). The functions of MCIP are as follows:

- To prepare and diagnose all meteorological fields required for SMOKE and CMAQ-CCTM.
- To calculate the time-varying, species-dependent dry deposition velocities for CMAQ-CCTM.
- To uniformly trim cells off the horizontal boundary of the domain defined by the meteorological model
- To decrease the vertical resolution of the meteorological data by layer collapsing.

The inputs to MCIP were time-period, horizontal and vertical grid definitions, dry deposition velocities option, and satellite cloud observations. MCIP generated a set of output files including grid description, and 2D and 3D meteorological data ready to be used as input to SMOKE and CMAQ-CCTM software.

4.2 Emissions Modelling

As depicted in Figure 4.1, the emissions data, the source of pollutants, is another key input to the PAQM. Hence, appropriate emissions files had to be generated before running PAQM. Emissions files are generally generated by emissions processor; the main purpose of these processors is to convert the resolution of the emission inventory data to the resolution required by an air quality model. The Sparse Matrix Operator Kernel Emissions (SMOKE) modelling system has been developed by the MCNC Environmental Modelling Center (EMC) to generate emissions data compatible with the range of air quality models (The institute for the Environment - The University of North Carolina at Chapel Hill, 2015). It is configured to integrate sparse-matrix algorithms for efficient performance with high performance computing (HPC). The emissions inventories are typically stored annually, while air quality models require inventories on an hourly basis. SMOKE processes the annual inventories and converts them to hourly so that they can be used in air quality modelling; this process is commonly known as temporal allocation. Similarly, SMOKE transforms data spatially and as well performs chemical speciation of pollutants. The emissions inventories are anthropogenic or biogenic, the former being pollutants that are emitted by man-made activities such as power plants, automobile emissions etc., and later being the emissions from natural ecosystem such as plants and forests.

4.2.1 Spatial and Temporal Allocations

4.2.1.1 Spatial Surrogates

Spatial distribution of emissions from macro level inventories (country, province, or county level) to grid level requires spatial surrogates. Several GIS based custom tools were developed that facilitated generation of both area spatial surrogates and line spatial surrogates' files. Table 4.2 summarizes the spatial surrogates created in the modelling domain to allocate the inventory data to the modelling grids. There are 13 provinces in Saudi Arabia; this study's domain mainly falls on the Riyadh province, while some parts of the domain extend into the Eastern province. The domain is hypothetically divided into counties. More number of counties were defined in the middle of the domain where the population is concentrated and is the area of interest as shown in Figure 4.3. Figure 4.4 shows the close up of the domain along with various types of roads and rails (Saudi Geological Survey, 2016) considered for spatial allocation.

4.2.1.2 Temporal Allocations

The temporal allocation profiles for the sources in the domain were developed based on the data distributed by the EMEP website (EMEP, 2016). The weekends were modelled as Thursday and Friday as was the case in the year 2012 in Saudi Arabia.

Table 4.2 Spatial Surrogates used for Generating the Emissions in the Domain

Surrogate ID	Surrogate	Description	Source
1	Population	Population habitation	(General Authority of Statistics, Kingdom of Saudi Arabia, 2012)
2	Expressways	Expressways passing through the domain	(Saudi Geological Survey, 2016)
3	Secondary roads paved	Secondary road within the domain	
4	Unpaved roads	Unpaved roads	
5	Railroads	Railroads	
6	½ Road + ½ Population	Combination of road and population	Composite
7	Crops	Agricultural and natural ecosystem	(Guenther, et al., 2006)
8	Industrial areas	0.75*Industrial + 0.25*Population	Composite
9	Residential areas	0.25*Industrial + 0.75*Population	Composite
10	Rural areas	0.25*Population + 0.75*Crops	Composite

Figure 4.3 Counties Defined in the Domain for Spatial Allocation of Emissions

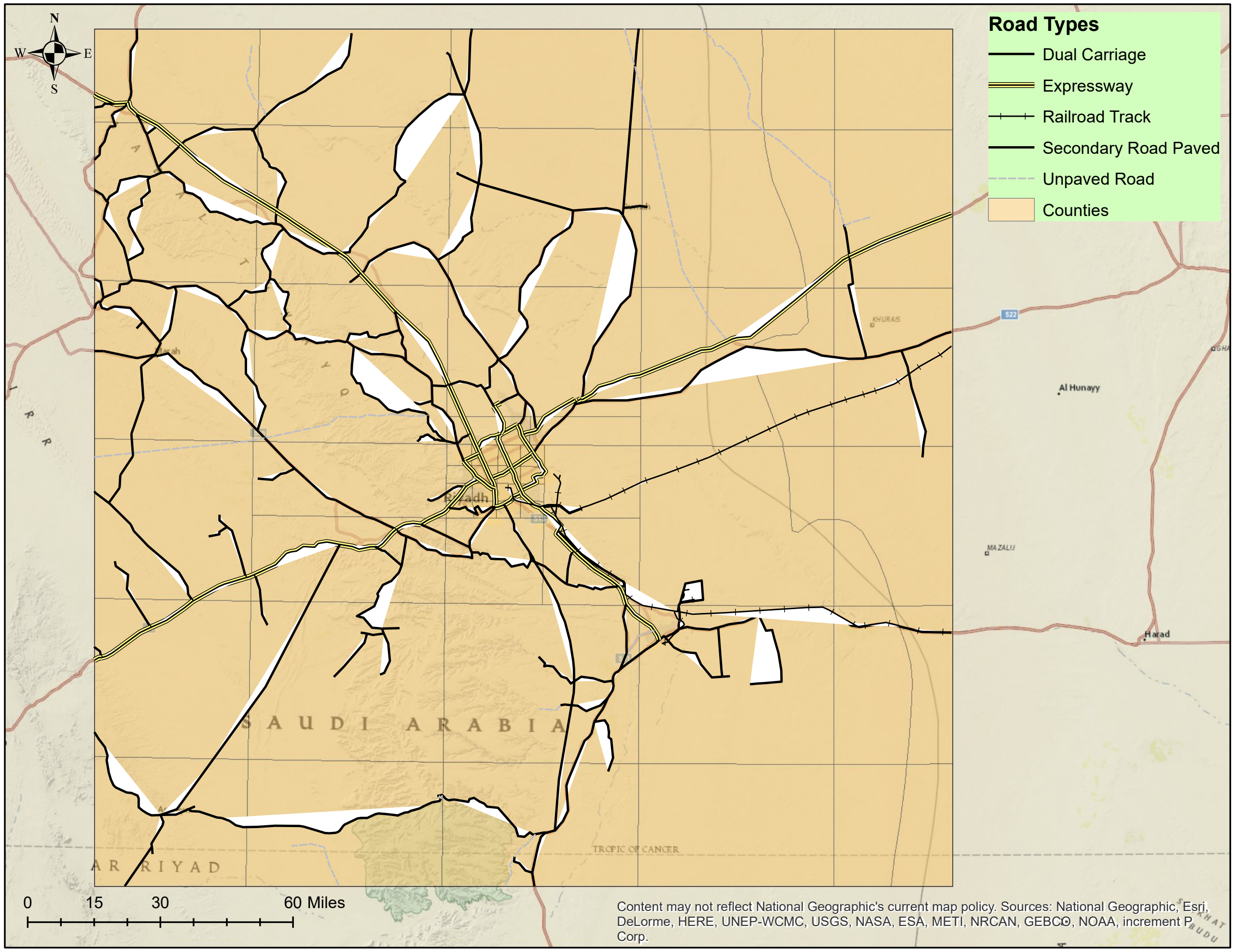

Figure 4.4 Road and Rails in the Domain for Spatial Allocation of Emissions

4.2.2 Biogenic Emissions

A biogenic emissions model, Model of Emissions of Gases and Aerosols from Nature (MEGAN) was used to estimate the terrestrial emissions of gases and aerosols (Guenther et al., 2006). MEGAN requires two types of input data files to generate biogenic emissions: land-cover data and weather data. The weather data generated by WRF and processed with MCIP (as explained in Section 4.1) was used for MEGAN. Global land-cover data, available at the NCAR community data portal (National Science Foundation, 2016), was downloaded and re-gridded to the model domain using GIS. The monthly average leaf area index (LAI), plant functional type (PFT), and emission factors (EF) were computed for each of the grid locations in the model domain. LAI calculates the emissions due to variations in leaf age by employing the equations presented by Guenther et al., (2006). This result in the creation of two files: the first containing information about model domain, emission factors, and monthly LAI, and the second includes information about PFT cover for each of the grid cells in the modelling domain. Figure 4.5 to Figure 4.8 illustrate the spatial extent of the percentage broad leaf trees, needle leaf trees, shrub-lands, and herbaceous cover respectively in the modelling domain. Running MEGAN involves executing three modules. The first module, MG2IOAPI, converts text format to a netCDF format by reading the preprocessed LAI and PFT files. The second module, MEGAN, calculates the gamma values, and the third module, MG2MECH, computes the emission rates and speciates and converts the MEGAN emission output to chemical mechanism species.

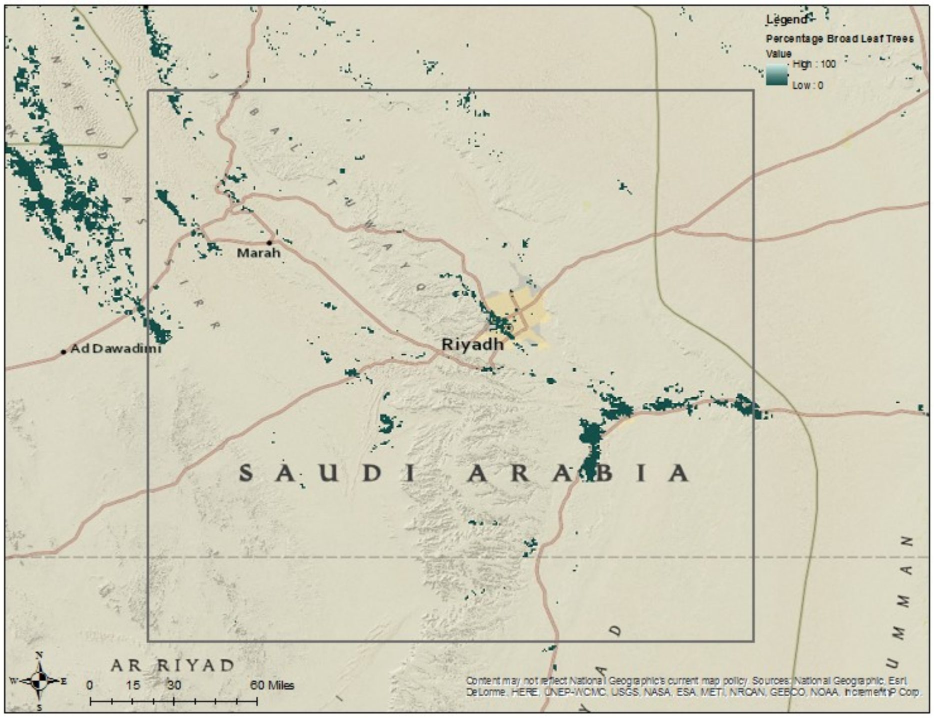

Figure 4.5 Percentage Broad Leaf Trees in the Domain

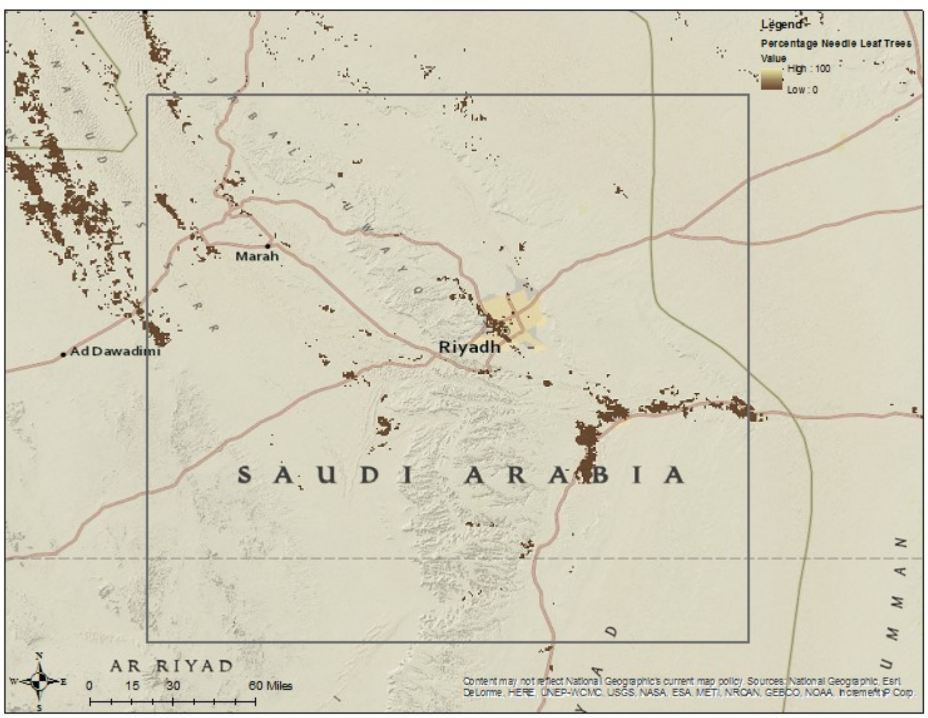

Figure 4.6 Percentage Needle Leaf Trees in the Domain

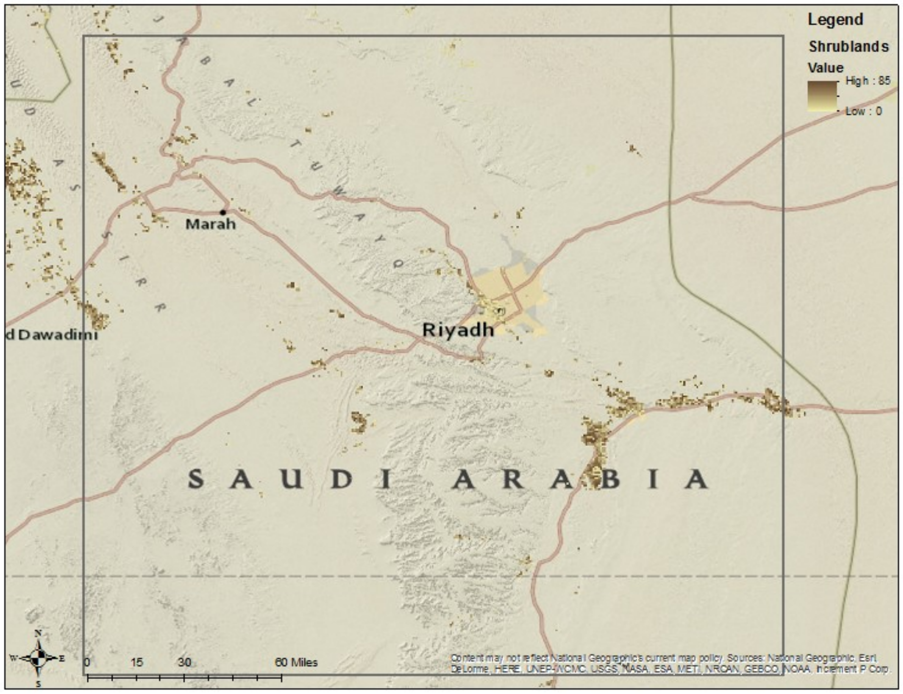

Figure 4.7 Percentage Shrub-Land in the Domain

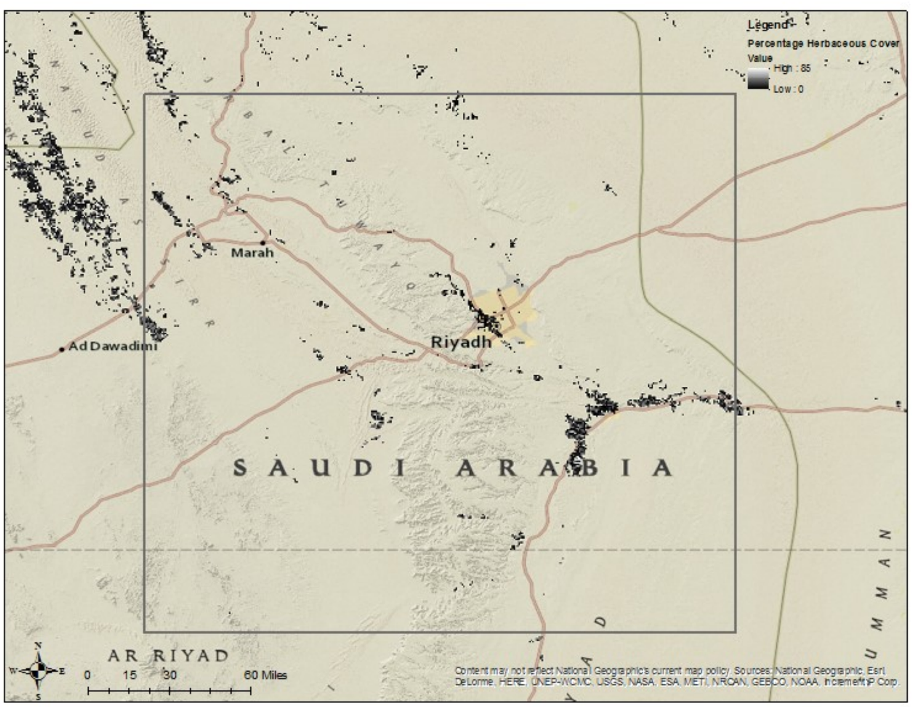

Figure 4.8 Percentage Herbaceous Cover in the Domain

Many speciation mechanisms are available in MEGAN, for this modelling study, the RACM mechanism was used for the speciation. MEGAN generated about 20 species of pollutants, some of which are isoprene (ISOP), terpene (TERP), paraffin (PAR), xylene (XYL), terminal olefin (OLE), methanol (MEOH), methane (CH_4), ammonia (NH_3) etc. All the species are presented in Appendix A. Figure 4.9 and Figure 4.10 show the peak concentrations of spatial variation of ISOP and NO in the modelling domain.

4.2.3 Anthropogenic Emissions

Anthropogenic emissions were formulated by a combination of direct sources of inventories and indirect calculations from the source data. The emissions were substantiated by limited field collected data described in Section 3. The global level sources of data such as CIRCE and EDGAR were explored for possible emissions data; however, they were not very useful as that data is mostly at country-level and at a low resolution. The current study is a very high resolution and limited to a small area and hence required detailed data in high resolution. Two main source types were considered, namely point sources and area sources. Point sources included stack emissions from refineries and cement plants and area sources were the emissions from automobiles. The process followed in generating the emissions files are described as follows.

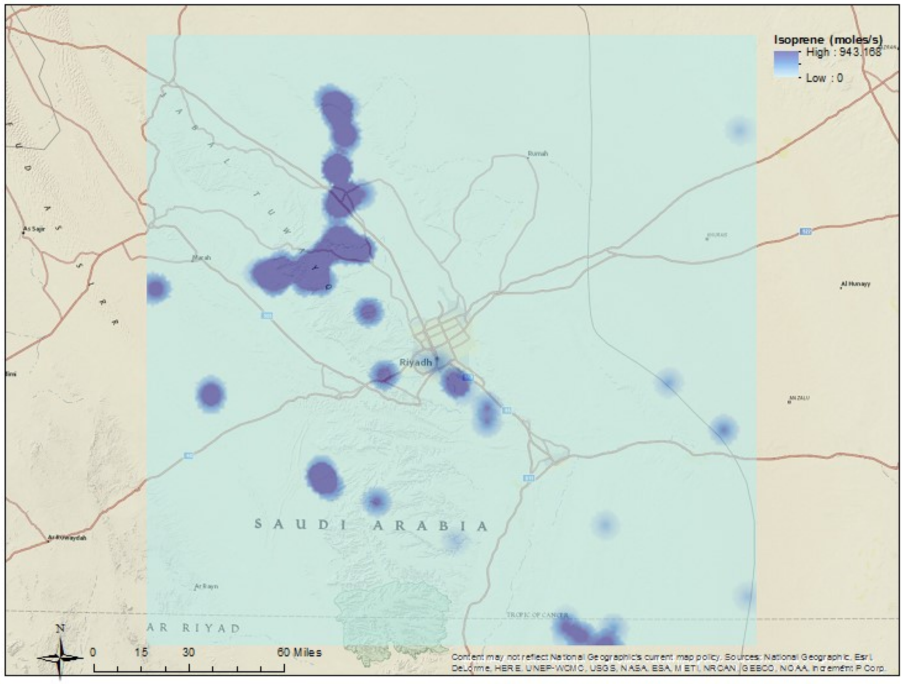

Figure 4.9 Spatial Variation of Isoprene Concentration (8-Hour Day Average) Generated by MEGAN

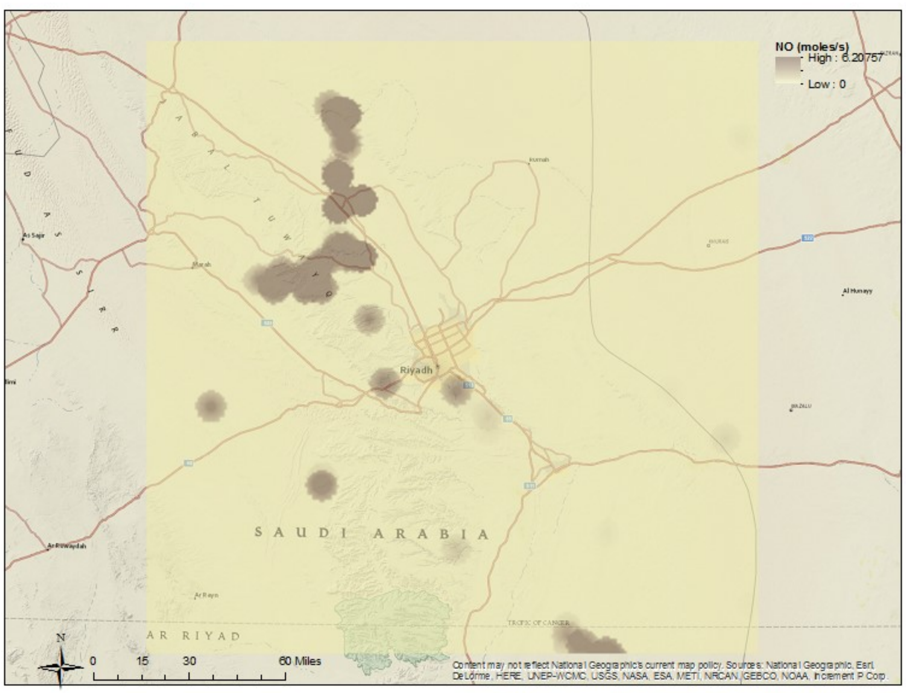

Figure 4.10 Spatial Variation of Nitric oxide Concentration (8-Hour Day Average) Generated by MEGAN

4.2.3.1 Emission Inventories

Two main sources of emissions were considered for modelling, the mobile source such as emissions from automobiles and static sources such as emissions from power plants and factories.

4.2.3.1.1 Automobile Emissions

The emissions of pollutants from automobiles were estimated based on the number of vehicles on the road and the pollutant emission factors of each type of vehicle. Table 4.3 shows the number of vehicles, emission factors, and the total annual emissions.

Table 4.3 Estimation of Emissions from Automobiles

	Private Cars (3.1 million)[1]		Light Trucks (1.2 million)[1]		Heavy Trucks (0.4 million)[1]		
Pollutant	Emission factors [2] (g/mile)	Annual emission (tons)	Emission Factor [2] (g/mile)	Annual emission (tons)	Emission factor [2] (g/mile)	Annual emission (tons)	Total emissions [3] (tons)
VOC	1.034	1,062,089	1.224	483,558	0.447	70,637	1,616,284
THC	1.077	1,106,257	1.289	509,237	0.453	71,586	1,687,080
CO	9.4	9,655,355	11.84	4,677,553	2.311	365,197	14,698,105
NO_x	0.693	711,826	0.95	375,310	8.613	1,361,073	2,448,209
PM_{10}	0.0044	4,520	0.0049	1,936	0.202	31,921	38,376
$PM_{2.5}$	0.0041	4,211	0.0045	1,778	0.219	34,608	40,597
CO_2	368.4	378,407,732	513.5	202,865,166			581,272,898

[1] (General Authority of Statistics, Kingdom of Saudi Arabia, 2012)
[2] (Office of Transportation and Air Quality, USEPA, 2008)
[3] Emissions for year 2012

4.2.3.1.2 Emissions from Static Sources

The main sources of pollution included in the emission inventory were a petroleum refinery, a power plant, and a cement factory. There are several small and medium scale industries in the domain in addition to a few sewage treatment plants that might contribute to the air pollution sources. However, due to the scarcity of accurate emission data, these were ignored. Table 4.4 presents the summary of the emissions from the sources considered in this modelling study.

Table 4.4 Estimation of Emissions from Static Sources

Pollution/Emission Source	Riyadh Refinery		Cement Plant	
	Emission factor (lb/scf) [1]	Annual emissions (tons) [2]	Emission factor (lb/ton) [3]	Annual emissions (tons) [4]
NO_x	32	174	7.4	8,159
CO	80	435	3.7	7,363
SO_2	-	-	8.8	3,681
PM_{10}	-	-	31.94	2,089
$PM_{2.5}$	-	-	129.76	129,115
TOC	-	-	2.1	31,782

[1] (RTI International, 2015)

[2] Calculated based on annual gas produced, approximately 12,000 MMSCF for year 2012 (General Authority of Statistics, Kingdom of Saudi Arabia, 2012)

[3] (US Environmental Protection Agency, 1995)

[4] Estimates based on cement and clinker production in year 2012 ((Yamama Cement Company, 2012)

4.2.4 Generation of Emissions Files

All the biogenic and anthropogenic emissions estimated in the previous section are processed as point and areas sources in SMOKE as described in the manual (The institute for the Environment - The University of North Carolina at Chapel Hill, 2015). This generates intermediate point and area output emission files that were then merged into the final emission files in the netCDF format, which is ready to be used as an input file for CMAQ.

4.3 CMAQ Modelling

As discussed in Section 2.3.3, CMAQ is identified as a suitable PAQM and has been used to model the pollutants. CMAQ consists of several Fortran 90 programs that use state of the science in air quality and estimate O_3, PM, toxic compound, and acid depositions in the troposphere. CMAQ is designed for single or parallel Unix/Linux based systems. The overview of CMAQ system components, installation and configuration are presented in Figure 4.1 and described in detail at the CMAS website (Community Modelling and Analysis System (CMAS), 2016). In order for the model CMAQ to run efficiently, it requires high-end computing resources. The computing support is provided by ACENET (ACENET, 2016). This facility is available to the research students at Atlantic Canadian Universities including Memorial University of Newfoundland.

4.3.1 Domain, Resolution, Initial and Boundary Conditions

The domain and grid resolution of the model is same as configured for the WRF model (Section 4.1). The ICON and BCON processors in CMAQ generate initial and boundary conditions for the simulations. The model used clear vertical profiles as the initial and boundary conditions; the spin up period for the base case run was about 10 days.

4.3.2 Simulations

The base case CMAQ simulation was performed with CMAQv5.0.2 released in May 2014, and it is the most stable version. This version has been used by US-EPA in unit tests, system tests, and for model evaluations prior to release (CMAQv5.0.2 Documentation, 2014). The CCTM module in the CMAQ system enables running the simulations. Two types of configuration options are available in CCTM; one is set during the compilation stage, which generates binary executable file, and the second is set during the execution stage of CCTM. The compile and execution options used for the base case modelling are shown in Table 4.5 and Table 4.6 respectively. The default chemical mechanism CB05TUCL_AE6_AQ with Rosenbrock gas-phase chemistry solver was used. The impact of various chemical mechanisms on the formation of O_3 is discussed in Chapter 5. In-line photolysis calculation module is invoked, and the sixth-generation CMAQ aerosol model with extensions for sea salt emissions and thermodynamics is configured for the simulation.

The simulation was performed for the month of July 2012; this month chosen to compare the simulated data with the observed data which was collected during the same month. On a 32-processor parallel, the simulation took about 15 hours to run.

Table 4.5 Compile Options used in CCTM

Configuration key	Description	Setting
ModDriver	Driver module	ctm_wrf WRF-based scheme for mass-conserving advection; this option is selected as WRF meteorology is used
ModGrid	The CCTM model grid configuration module	Cartesian
ModInit	The CCTM time-step initialization module that uses a Yamartino scheme for mass-conserving advection	init_yamo
ModCpl	Unit conversion and concentration coupling module	gencoor_wrf
ModHadv	The only option in CMAQv5 for the horizontal advection module is the hyamo global mass-conserving scheme	Hyamo
ModVadv	Vertical advection module.	Vwrf
ModHdiff	horizontal diffusion module	Multiscale
ModVdiff	Vertical diffusion module	acm2
ModDepv	Deposition velocity calculation module	m3dry: CMAQ dry deposition velocity routine
ModEmis	CMAQ in-line emissions module	emis
ModPhot	Photolysis calculation module	phot_inline
ModChem	Gas-phase chemistry solver module	ros3: Rosenbrock chemistry solver
ModAero	CMAQ aerosol module	aero6: sixth-generation modal CMAQ aerosol model with extensions for sea salt emissions and thermodynamics; includes a new formulation for secondary organic aerosol yields
ModCloud	CMAQ cloud module for modelling the impacts of clouds on deposition, mixing, photolysis, and aqueous chemistry.	cloud_acm_ae6: ACM cloud processor that uses the ACM methodology to compute convective mixing with heterogeneous chemistry for AERO6
Mechanism	Specifies the gas-phase, aerosol, and aqueous-phase chemical mechanisms to use for modelling air quality.	cb05tucl_ae6_aq

Table 4.6 Execution Options used in CCTM

Configuration key	Description	Setting
CLD_DIAG	Cloud diagnostic file	N
CTM_AERDIAG	aerosol diagnostic file	N
CTM_PHOTDIAG	photolysis diagnostic file	N
CTM_SSEMDIAG	sea-salt emissions diagnostic file	N
CTM_WB_DUST	use inline windblown dust emissions	N
CTM_ERODE_AGLAN	use agricultural activity for windblown dust	
CTM_DUSTEM_DIAG	windblown dust emissions diagnostic file	
CTM_LTNG_NO	turn on lightning NOx	N
CTM_WVEL	save derived vertical velocity component to conc file	Y
KZMIN	use Min Kz option in edyintb	Y
CTM_ILDEPV	calculate in-line deposition velocities	Y
CTM_MOSAIC	landuse specific deposition velocities	Y
CTM_ABFLUX	Ammonia bi-directional flux for in-line deposition velocities	N
CTM_HGBIDI	Mercury bi-directional flux for in-line deposition velocities	N
CTM_SFC_HONO	Surface HONO interaction	Y
CTM_BIOGEMIS	calculate in-line biogenic emissions	N
B3GTS_DIAG	write biogenic mass emissions diagnostic file	Y
CTM_PT3DEMIS	calculate in-line plume rise for elevated point emissions	N
PT3DDIAG	optional 3d point source emissions diagnostic file	Y
PT3DFRAC	optional layer fractions diagnostic	N
CTM_DDM3D	ddm-3d calculations; note: executable must be compiled with "-Dsens"	Y

4.4 Simulation Results and Comparison with Observed Data

The results of the base case CMAQ simulation are presented as spatial and diurnal variation of O_3 and are compared to the observed data in the following sections. The detailed analyses of other parameters from the simulations are elaborately discussed in Chapter 5.

4.4.1 Spatial Variation of O_3

The spatial variation of O_3 concentration in the domain is shown in Figure 4.11. It is averaged over the modelling period. Although the sources of the pollutants are in the center of the domain, the peak concentrations are in the southwest and northeast of the domain. This is likely due to the wind pattern during the modelling period. Figure 4.12 illustrates the close-up of the model predicted concentrations along with the data collected from the selected locations in the domain. As observed from the figure, the values of the observed data were higher than the model predicted at some locations, indicating that the model generally under-predicted the concentrations. For example, at the stations 1, 2, and 5, the concentrations observed were about 40% higher than the model predicted, and at station 3, the observed concentrations were over 200% higher. Station 3 seems to be an outlier, meaning a spike in pollutant concentration might have happened on the observed days, which could not be captured in the model input. Under-prediction of concentrations at other stations could be primarily due to missed inventory of the input data. At station 15 and 16 in the north of the domain, the model seems to have performed perfectly. In general, it could be implied that the model performance was better at locations away from the sources.

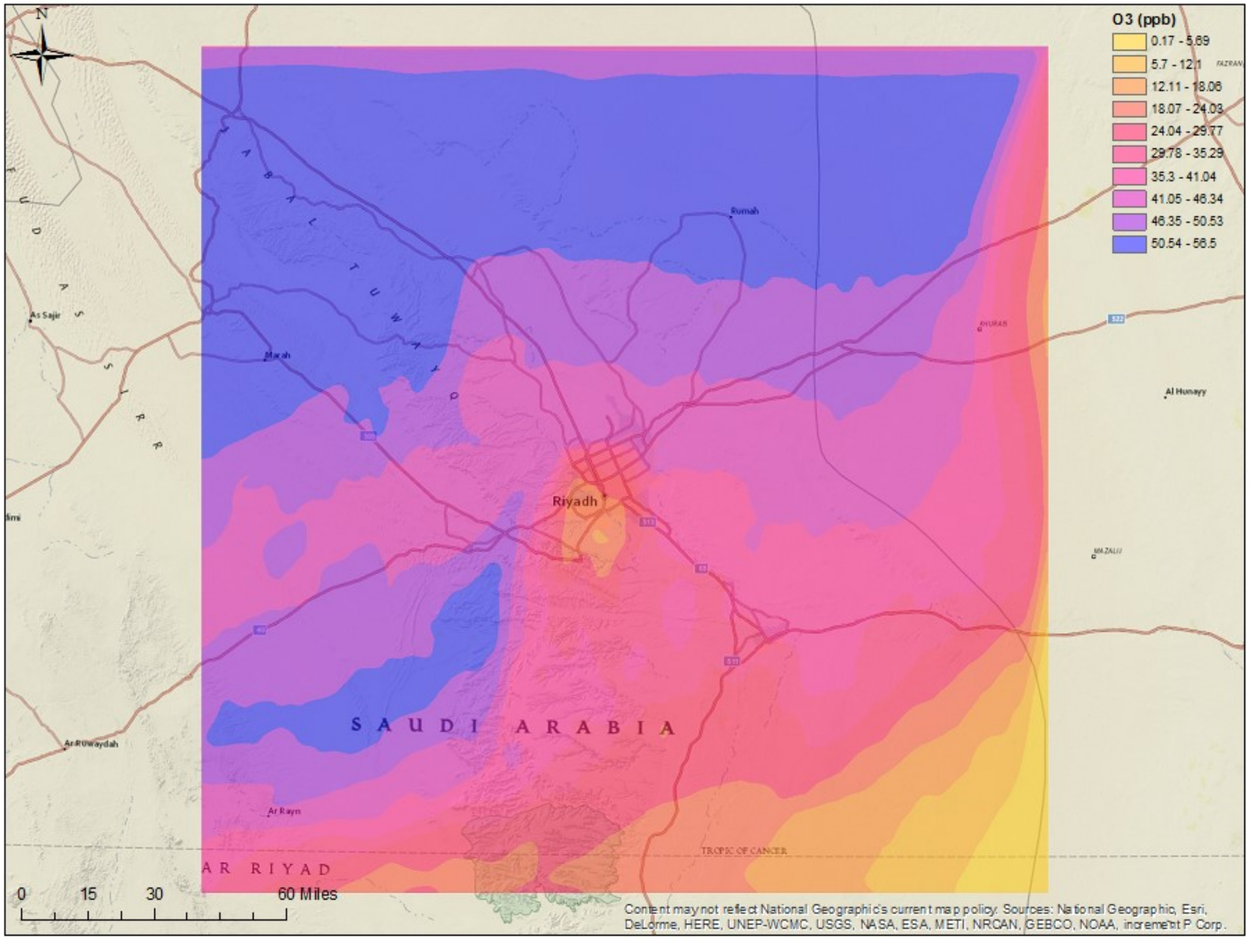

Figure 4.11 Spatial Variation of 8-Hour Average O_3 Concentration on July 15 as Predicted by the Model

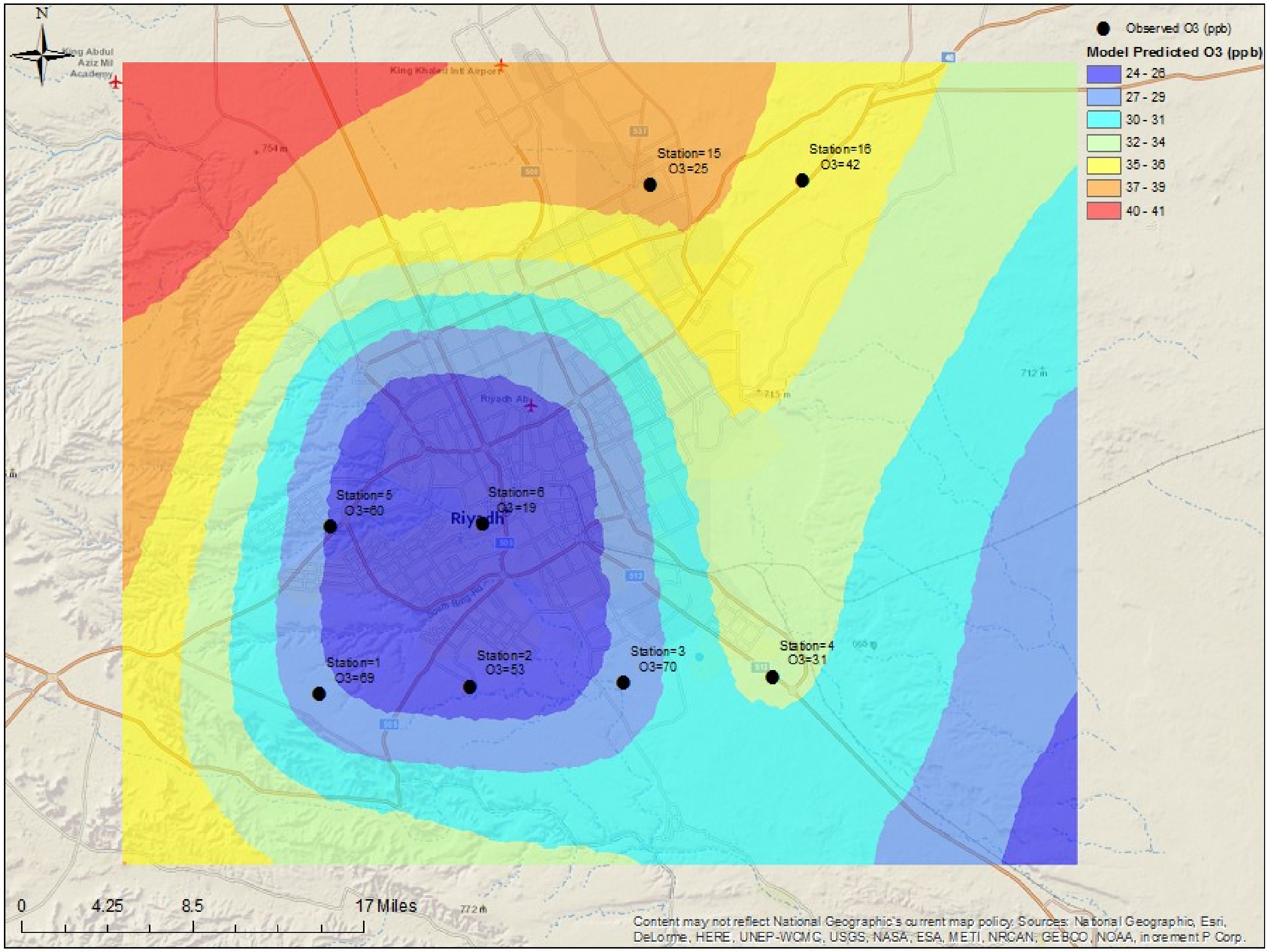

Figure 4.12 Observed vs Model Predicted O_3 Concentration at the Center of Domain

4.4.2 Diurnal Variation of O_3

Figure 4.13 illustrates the diurnal variation of O_3 for both observed and model predicted values. O_3 concentrations in both followed a typical pattern; it gradually increases after sunrise, reached its highest at noontime, decreased towards sunset, and remained low throughout the night. Details on this pattern have been discussed in Section 3.3.3.2. The model values correlated very well with the observed during morning and evening, however, there is a wide variation during the peak of daytime. The model underpredicts the concentrations during peak photolysis period. Two reasons could be attributed to this; noncomprehensive emission inventory and low photolysis rates in the model. The emission inventory performed as discussed in Section 4.2 was based on available data, there is a good possibility that it is not comprehensive resulting in lower prediction by the model compared to observed data. The lower photolysis frequencies require adjustments for the current region and could be accounted for in the model is by including it in the uncertainty analysis as discussed in Chapter 6. The validation of the two major objectives of this research; identification of chemical mechanisms and development of RFM, will not be affected due to the model underpredictions.

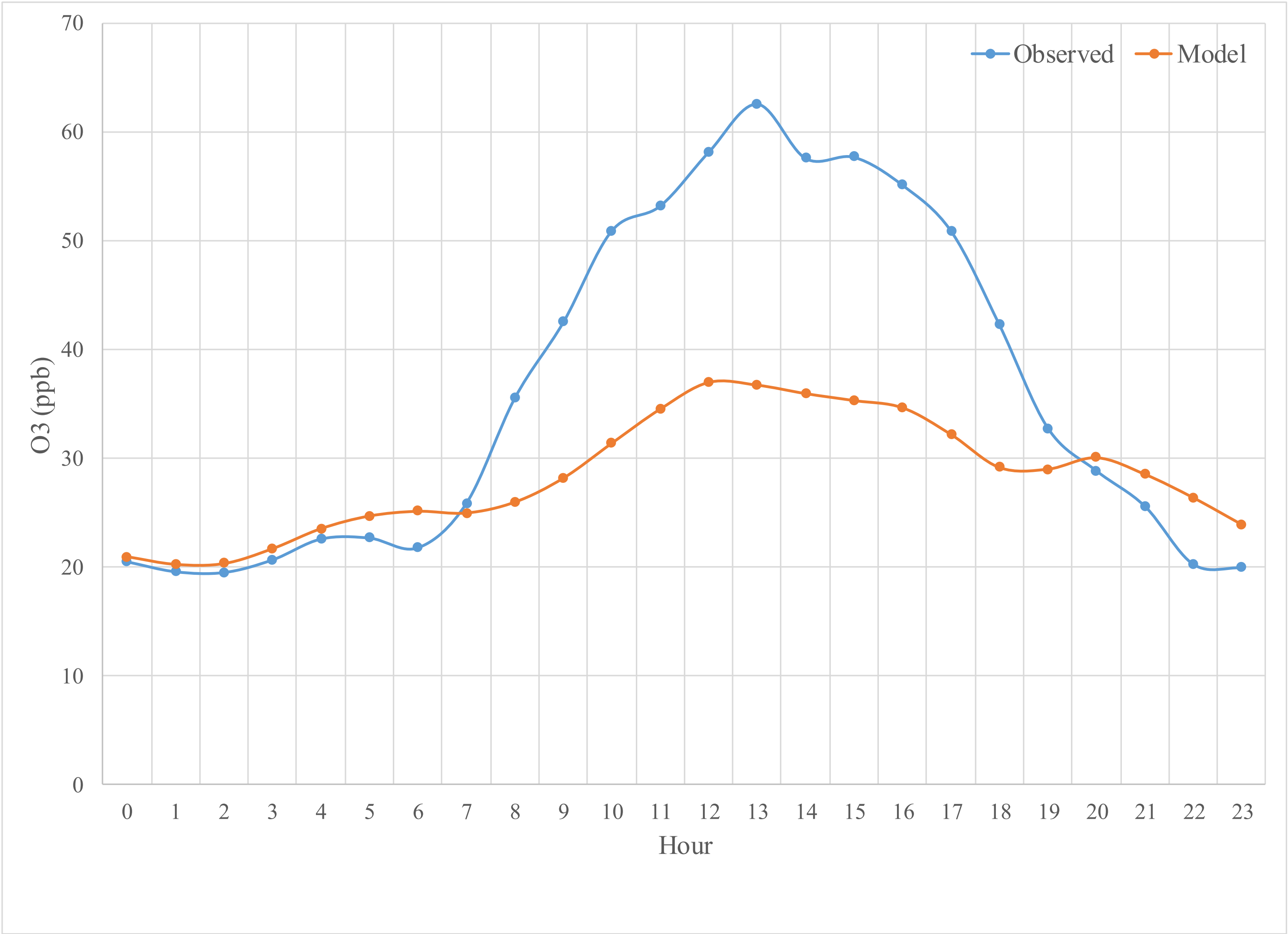

Figure 4.13 Observed and Model Predicted Diurnal Variation of O_3 Averaged at the Observed Stations

4.5 Summary

This chapter involved setting and configuring necessary models required to meet the objectives of this research. Subsequently, a base case simulation was performed to compare the model results with observed data. Simulation of the air quality model, CMAQ, is dependent on the outputs, primarily, from two other models, namely: meteorological model and emissions model. WRF (Weather Research and Forecasting) version 3.4.1 was used to generate the meteorological data necessary for CMAQ. WRF was run for the year 2012 with domain centered at Riyadh. The dimensions of the domain were 300 km x 300 km and horizontal resolution was 4 km resulting in 78 x 78 grid points. Meteorology-Chemistry Interface Processor (MCIP) was used to convert WRF output to CMAQ compatible meteorological dataset.

The emissions model, SMOKE (The Sparse Matrix Operator Kernel Emissions), was employed to generate the emissions in the domain. The emissions inventories were anthropogenic (man-made activities such as power plants, automobile emissions etc.,) and biogenic (emissions from natural ecosystem such as plants and forests). Spatial distribution of emissions from macro level inventories (country, province, or county level) to grid level requires spatial surrogates; this was achieved by developing several advanced GIS based custom tools. Various types of surrogates were created such as for population, expressways, crops, industrial areas, residential area, etc. Biogenic emissions were processed using MEGAN (Model of Emissions of Gases and Aerosols from Nature). MEGAN generated about 20 species of pollutants, some of which are isoprene (ISOP), terpene (TERP), paraffin

(PAR), xylene (XYL), terminal olefin (OLE), methanol (MEOH), methane (CH_4), and ammonia (NH_3). Available anthropogenic emissions data such as road and static emission sources were collected and processed for SMOKE. SMOKE subsequently combined the different emissions and generated one aggregated emissions file ready for CMAQ simulations. CMAQv5.02 was run with clean initial and boundary conditions. The spin-up period was about 10 days. CCTM module in CMAQ is the key module to perform simulations. The default chemical mechanism CB05TUCL_AE6_AQ with Rosenbrock gas-phase chemistry solver was used. July 2012 was selected to run the simulation for the full month. The results of the modelling were compared with the available O_3 data. The results showed that the model generally under-predicted, however, it was observed that the model performance was better away from the sources. Diurnal variation of O_3 showed that the model values correlated well with observed data during morning and evening, however, a wide variation was noticed during midday.

CHAPTER 5: ATMOSPHERIC CHEMICAL MECHANISMS IN ARID REGIONS

5.1 Model Simulations

A detailed literature review identified main atmospheric chemical mechanisms (ACM) that were developed to understand issues associated with urban smog formation as presented in Section 2.3.2. The ACMs share the common concept of reaction rates and products; however, differ in rate constants, photolysis (due to change in pressure and temperature), and the treatment of organic and inorganic chemistry. Several studies have compared these mechanisms and found large variations among model predictions. Those studies also note that the variation in O_3 predictions depends on the location, VOC/NO_x ratios, and concentrations of precursor pollutants. The production of O_3 and other components of photochemical smog depends on various reactions in the atmosphere and their reaction rates. These reaction rates are unique to the characteristics of arid regions. Since ACM and their reaction rates have not been studied in arid regions, this chapter studies the various chemical mechanisms on the formation of O_3, selected oxidants, and nitrogen species in the central region of Saudi Arabia.

Air quality model simulations were performed using the CMAQ model with several chemical mechanisms that included the variations of CB05 (CB05E51, CB05TUCL), RACM (RACM2), and SAPRC07 (SAPRC07TB, SAPRC07TC, SAPRC07TIC). The configuration of other parameters such as domain, resolution, meteorology, and emission are the same as presented in Chapter 4. This results in 6 simulations, that were performed to model a period of one month. The Rosenbrock third order numerical solver (Sandu, et al., 1997) was used to solve the system of differential equations for gas-phase chemistry.

The summer month of July was chosen to reflect the arid weather. The wind conditions in the domain during this period is illustrated in Figure 5.1. As shown in the figure, the winds in general are predominantly coming from north and northeast indicating the pollutants are driven towards the southwest of the domain. At the stations in the north, wind speeds are in the range of 6 -8 m/s which is relatively high compared to the stations in the middle and south where the wind speeds were in the range of 2-5 m/s.

This chapter presents the results of the comparison of various chemical mechanisms on the formation of selected hydroxyl radicals, nitrogen compounds, and O_3. The surface O_3 concentrations were compared with observed data.

5.2 Comparing Variation of CB05 and SAPRC07

5.2.1 CB05E51 and CB05TUCL

Table 5.1 presents the domain-wide mean concentrations of various species simulated with six different chemical mechanisms, including the variations of CB05 (CB05E51 and CB05TUCL). The differences in the mean concentrations between the two CB05 mechanisms were less than 1% except for OH, NO_z, and MEPEX where CB05E51 produced 7%, 7.7%, and 8% more than CB05TUCL respectively. The differences in the mean concentrations of O_3 (shown in Figure 5.2) were less than 0.5%; this implies that there is no significant difference between the mechanisms when producing O_3. In order to compare with the other mechanisms, the concentrations for various parameters were averaged and will be referred to as CB05.

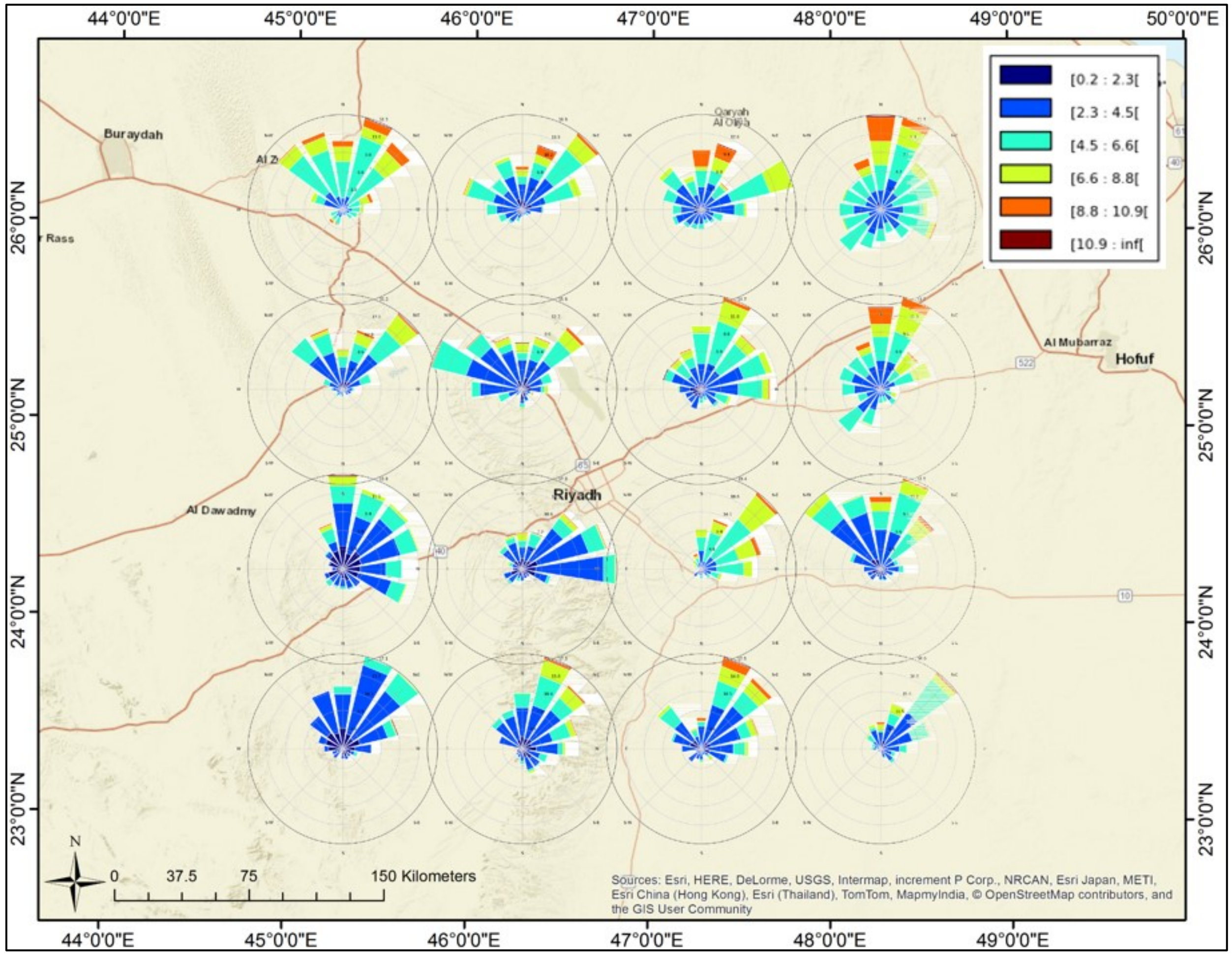

Figure 5.1 Wind roses illustrating wind condition at various locations in the domain during the modelling period (wind speed in m/s and coming from)

Table 5.1 Domain-Wide Mean Concentrations Predicted by Six Chemical Mechanisms during the Modelling Period.

Species	Unit	CB05E51	CB05TUCL	SAPRC07TB	SAPR07TC	SAPRC07TIC	RACM2
Hydroxyl radical (OH)	pptv	0.101	0.093	0.094	0.094	0.097	0.119
Hydrogen peroxide (H_2O_2)	pptv	1396	1400	1389	1389	1399	1454
Methylhydroperoxide (MEPX)	pptv	350.20	324.79	279.41	279.48	279.20	370.68
Nitric acid (HNO_3)	pptv	79.55	78.43	77.36	77.46	78.59	82.96
Peroxyacetyl nitrate (PAN)	pptv	4.13	4.07	3.15	3.18	3.45	2.29
Nitrogen oxide (NO)	pptv	7.06	6.99	7.89	7.93	8.18	8.74
Nitrogen dioxide (NO_2)	pptv	60.97	62.23	67.58	67.72	68.36	63.79
Secondary Nitrogen (NO_z)	pptv	197.62	212.91	257.29	257.38	258.64	207.32
Ozone (O_3)	ppbv	36.84	36.91	37.15	37.15	37.15	37.04

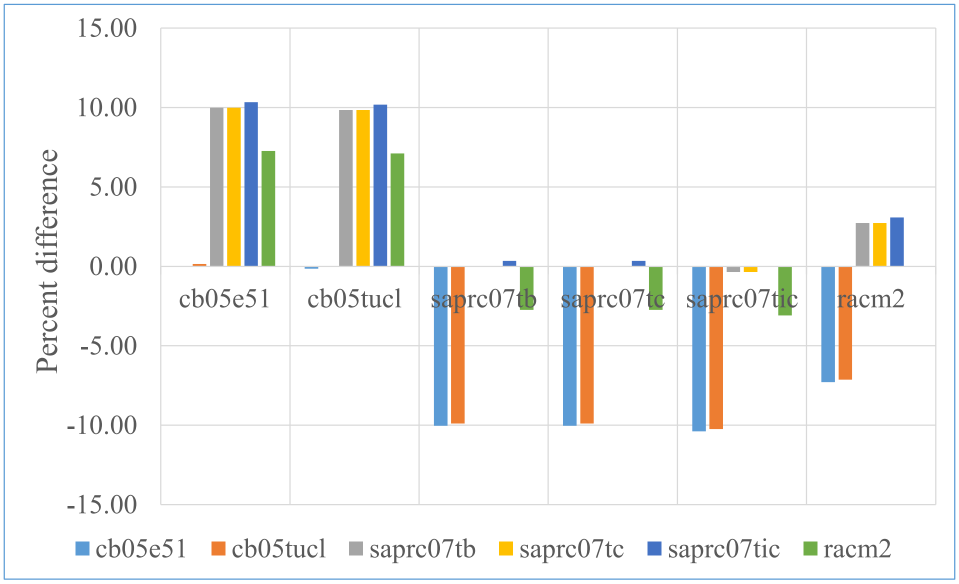

Figure 5.2 Comparison of Mean O_3 Concentration for Various Chemical Mechanisms.

5.2.2 SAPRC07TB, SAPRC07TC, and SAPRC07TIC

The three variations of SAPRC07 (SAPRC07TB, SAPRC07TC, and SAPRC07TIC) produced similar concentrations for all species. The differences between the species presented in the Figure 5.1 were less than 1% implying that no significant variation exists in terms of producing the listed species. The concentrations produced by the three variations were averaged (called SAPRC07) to compare with other mechanisms.

5.3 Comparing CB05, SAPRC07 and RACM2

5.3.1 Selected Oxidants

5.3.1.1 Effect on Hydroxyl radical (OH)

The atmospheric oxidation capacity is determined by the presence of an OH radical, as it reacts with many trace species present in the atmosphere. In the current domain and simulation, domain-wide mean OH concentrations predicted by SAPRC07, CB05, and RACM2 were 0.095 pptv, 0.097 pptv, and 0.119 pptv respectively. RACM2 predicts about 25% more OH than CB05 and SAPRC07 while there was no significant difference between the CB05 and SAPRC07 predictions (Table 5.2). Spatial variation of the OH radical and percent differences is shown in Figure 5.3. CB05 and SAPRC07 predicted 0.160 pptv in the north and close to zero in south, while RACM2 predicted a high of 0.195 pptv in the northwest and a low of 0.075 pptv in the southeast. Compared to the CB05 mechanism, RACM2 predicted higher OH production mostly in the range of 24-32% and the maximum difference was up to 64%. SAPRC07 predicted higher OH in the range of 24-30% compared to other with the highest increase reaching as high as 60%. Spatially, the maximum enhancement was observed in the southwest of the domain. This is the same area where O_3 is produced in high concentrations (described later). Some of the reasons that can be attributed to this high OH production by RACM2 are explained below.

Firstly, RACM2 produces more O_3 and subsequently generates more O atoms under photolysis, and O atoms react with H_2O to produce OH radicals. Secondly, the lower reaction rate of NO_2 + OH in RACM2, consumes less OH radicals from the atmosphere compared to CB05 and SAPRC07. Sarwar, et al., 2013 identified that additional reactions in RACM2 with olefins and methacrolein may be another reason for the higher OH production. However, this does not seem to be the case, as the reactions with olefins and methacrolein exist with the same rates in all three mechanisms. The CMAQ model species name for methacrolein in CB05 is MAPAN and the species name in SAPRC07 and RACM2 is MACR.

Table 5.2 Domain-Wide Mean Concentrations during the Modelling Period of Various Species Averaged by Variations (CB05, SAPRC07, and RACM2).

Species	Unit	CB05	SAPRC07	RACM2	Percent Differences		
					CB05 vs SAPRC07[1]	CB05 vs RACM2[2]	SAPRC07 vs RACM[3]
Hydroxyl radical (OH)	pptv	0.1	0.1	0.119	-1.9	22.8	25.3
Hydrogen peroxide (H_2O_2)	pptv	1.4	1.40	1.45	-0.42	3.97	4.41
Peroxyacetic acid (PACD)	pptv	61	4	28	-92.46	-54.4	504.74
Methylhydroperoxide (MEPX)	pptv	337	279	370	-17.22	9.84	32.9
Nitric acid (HNO_3)	pptv	78	77	82	-1.49	5.02	6.61
Peroxyacetyl nitrate (PAN)	pptv	4	3	2	-20.48	-44.18	-29.68
Nitrogen oxide (NO)	pptv	7	7	8	13.83	24.40	9.28
Nitrogen dioxide (NO_2)	pptv	61	67	63	10.20	3.56	-6.02
Secondary Nitrogen (NO_z)	pptv	205	257	207	25.5	1.01	-19.57
Ozone (O_3)	ppbv	36.8	40.1	38.5	8.81	4.46	-3.95

[1] 100 x (SAPRC07 - CB05) / CB05
[2] 100 x (RACM2 - CB05) / CB05
[3] 100 x (RACM2 – SAPRC07) / SAPRC07

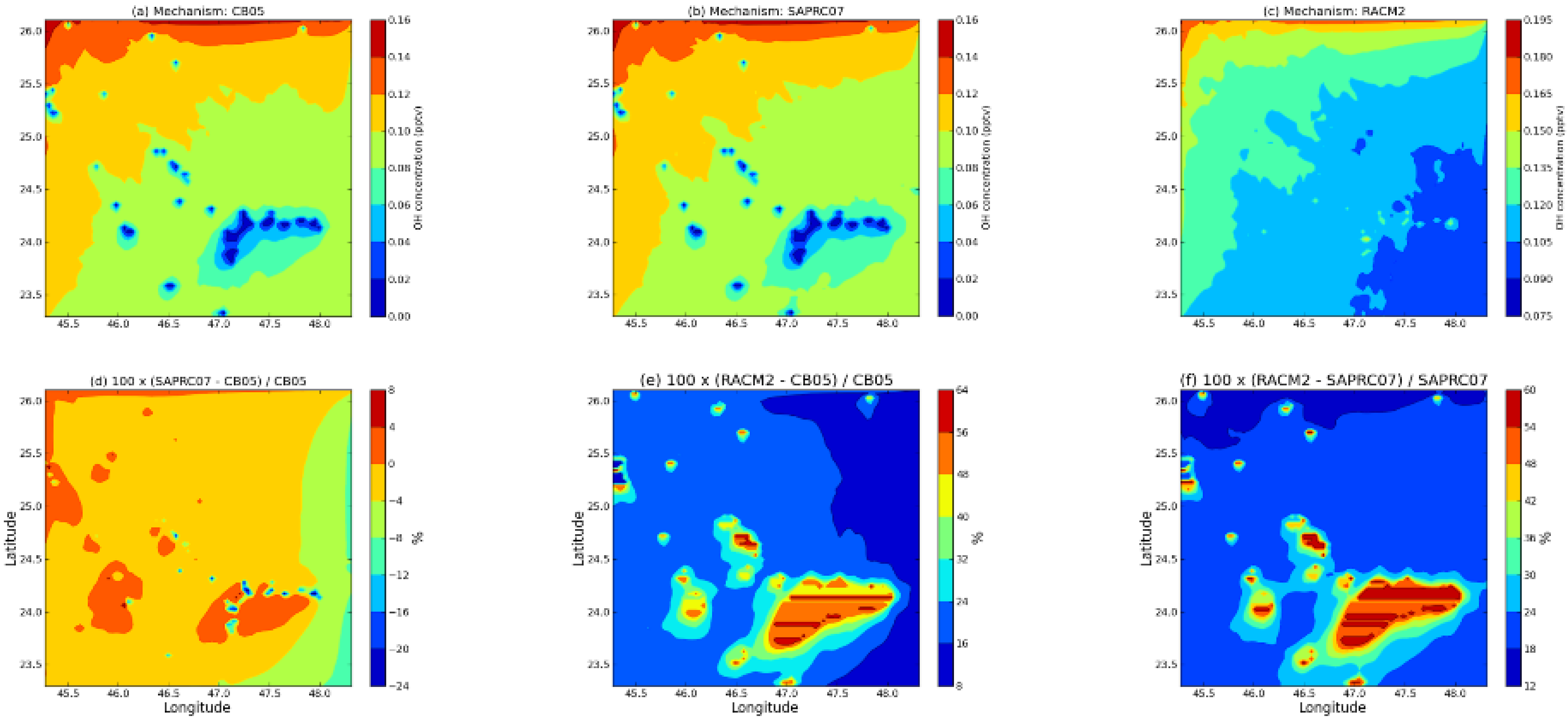

Figure 5.3 Spatial Distribution of Predicted Mean OH Concentrations Obtained with Chemical Mechanism a) SAPRC07 b) RACM2 c) CB05 and Percent Differences between the Mechanisms e) SAPRC07 and CB05 e) RACM2 and CB05 f) RACM2 and SAPRC07

For the study by Sarwar, et al., 2013 in their US domain, it was observed that OH enhancement by RACM2 was in the range of 36-60%. Comparing these results, the enhancements in this study, however, were mostly in the range of 24-32%, which is significantly lower than the US domain. This could be due to the shortage of atmospheric moisture. The OH measurements were not performed in the study area; hence, the model predictions could not be compared with field measurements. Some studies suggested that RACM2 under-predicts the observed OH by 15% and CB05 by 30% (Mao, et al., 2010; Lu, et al., 2013).

5.3.1.2 Effect on Hydrogen Peroxide (H_2O_2)

H_2O_2 exists in considerable amounts in both gaseous and aqueous phases inside clouds, and it is considered the most efficient oxidant in the aqueous phase and is known to convert SO_2 to SO_4 (Seinfeld and Pandis, 2006). Figure 5.4 shows the spatial variation of mean H_2O_2 in the domain obtained with CB05, SAPRC07, and RACM2 mechanisms and corresponding percent differences. SAPRC07 and CB05 predicted similar H_2O_2 concentrations in the domain, varying from 0.90 ppbv in the north to 1.95 ppbv toward the southeast. RACM2 produced up to 9% more H_2O_2 than the other two, with its highest concentration in the south. The chemical reactions and rates governing the formation and destruction of H_2O_2 under various chemical mechanisms are shown in Table 2.4. The formation of H_2O_2 in CB05 and SAPRC07 is similar except for the additional reaction OH + OH = H_2O_2 in CB05, however, it also has an additional destruction reaction (H_2O_2 + O=OH + HO_2).

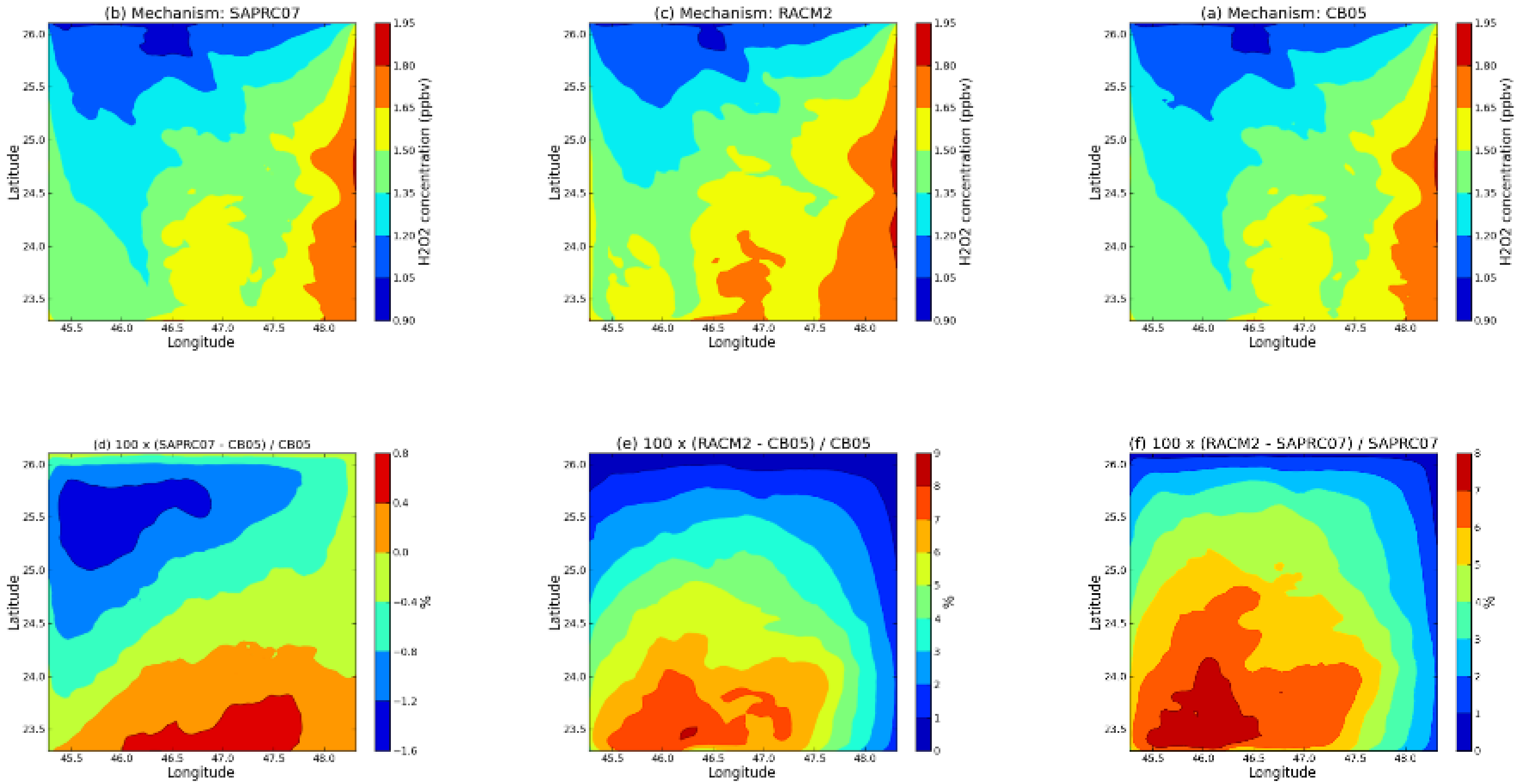

Figure 5.4 Spatial Distribution of Predicted Mean H_2O_2 Concentrations Obtained with Chemical Mechanisms a) SAPRC07 b) RACM2 c) CB05 and Percent Differences between the Mechanisms e) SAPRC07 and CB05 e) RACM2 and CB05 f) RACM2 and SAPRC07

RACM2 produces additional H_2O_2 because of the reactions of O_3 with different organic compounds (such as alkenes), as shown in Table 2.4. RACM2 has the highest H_2O_2 formation potentially due to these reactions unlike another finding (Sarwar, et al., 2013). This implies that organic compounds have a significant role in the formation and destruction of O_3.

5.3.2 Selected Nitrogen Species

5.3.2.1 Effect on Peroxyacyl nitrates (PAN)

PAN is one of the components of photochemical smog and forms with the reaction of aldehydes and NO_2 as shown in Table 2.5. Although the reaction rates differ (RACM2 reaction rate being the highest), the formation mechanisms of the three mechanisms are similar. The reverses of the same mechanisms destroy PAN; additionally, it is also destroyed with the formation of NO_2, NO_3, and other compounds. In RACM2, PAN reacts with OH to form NO_3 and other organic compounds. Figure 5.5 shows the spatial distribution of the mean PAN concentration and percent differences predicted by the three mechanisms. In most of the domain, all three mechanisms produced concentrations in the range 0-8 ppbv, but there were few patches of concentrations in the north ranging from 48 to 64 ppbv. CB05 produced the maximum concentration followed by RACM2 and SAPRC07. Due to large differences in the concentrations at certain locations, the percent differences showed a wide variation. The concentrations of PAN predicted by all mechanisms, when compared with another study (Sarwar et al., 2013) are high.

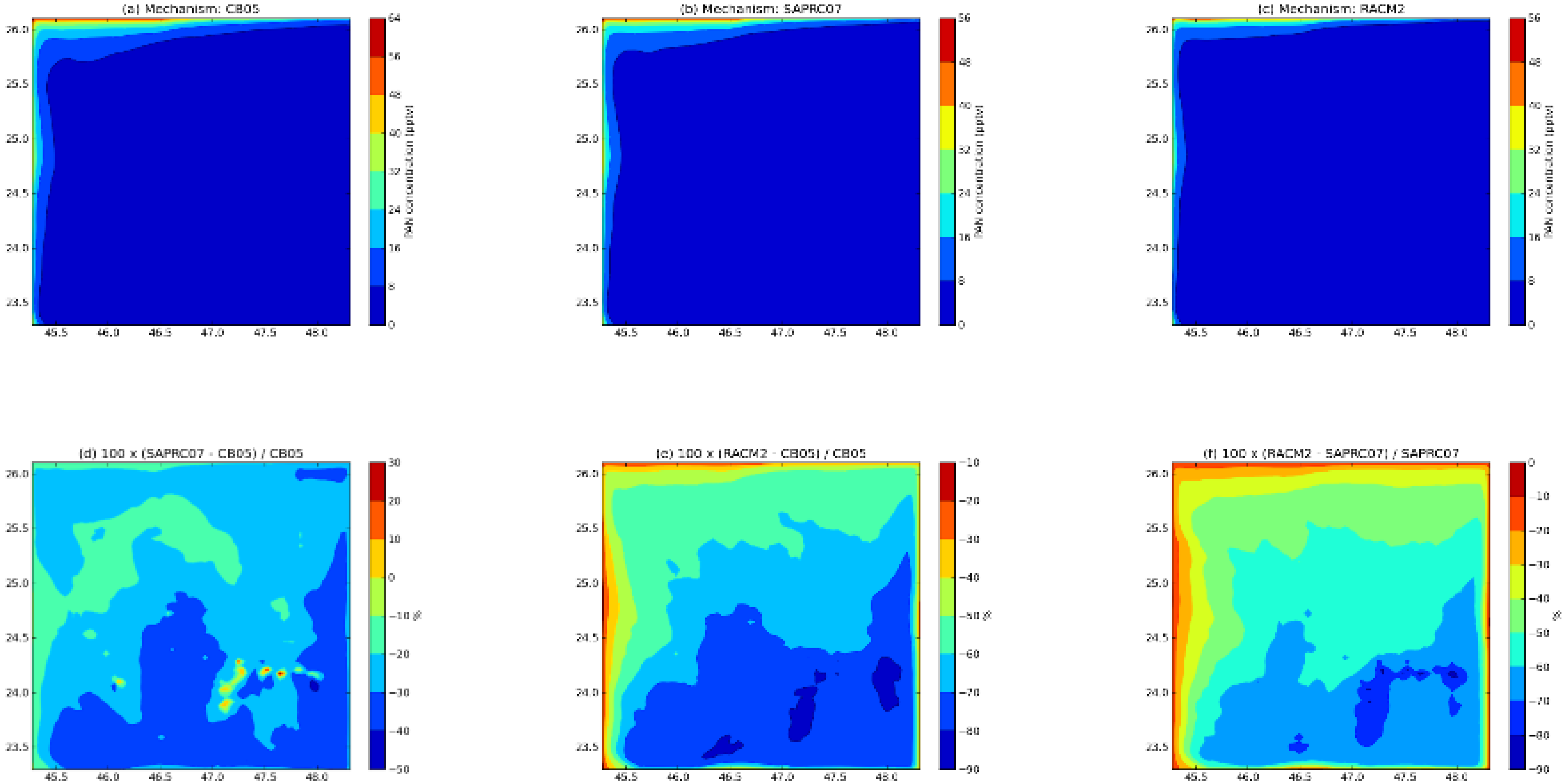

Figure 5.5 Spatial Distribution of Predicted Mean PAN Concentrations Obtained with Chemical Mechanisms a) SAPRC07 b) RACM2 c) CB05 and Percent Differences between the Mechanisms e) SAPRC07 and CB05 e) RACM2 and CB05 f) RACM2 and SAPRC07

This indicates that there is high formation of photochemical smog in certain areas in the domain. The reason for this high concentration and its formation requires experimental analysis.

5.3.2.2 Effect on Secondary Nitrogen Species (NO_z)

NO_z was calculated based on equations presented in Table 5.3 for the three mechanisms. Figure 5.6 shows the variation of the mean concentration of NO_z predicted by the mechanisms along with the percent differences. RACM2 predicts the highest concentration followed by SAPRC07 and CB05. For all the three mechanisms, the lowest concentration was in the southeast area of the domain and the highest was towards the northwest. RACM2 produced about 60% and 35% more NO_z than CB05 and SAPRC07 respectively. The major components of NO_z are organic nitrates (NTR) and PAN which composed about 78%, 81%, and 86% of NO_z concentrations in CB05, SAPRC07, and RACM2 respectively.

Table 5.3 Components in Secondary Nitrogen Species (NO_z) in Various Mechanisms.

Chemical Mechanism	NO_z
CB05	NO_3 + 2 *N_2O_5 + HONO + HNO_3 + PAN + PANX + PNA + NTRI + NTRIO2 + NTRM + $NTRMO_2$ + NTROH + NTRPX + CRON + CRNO + CRN2 + CRPX + OPAN
RACM2	NO_3 + 2 *N_2O_5 + HONO + HNO_3 + PAN + PPN + MPAN + HNO_4 + ISON + ONIT + NALD + ADCN + OLNN + OLND
SAPRC07	NO + NO_2 + NO_3 + $2N_2O_5$ + HONO + HNO_3 + HNO_4 + PAN + PAN2 + PBZN + MAPAN + NPHE

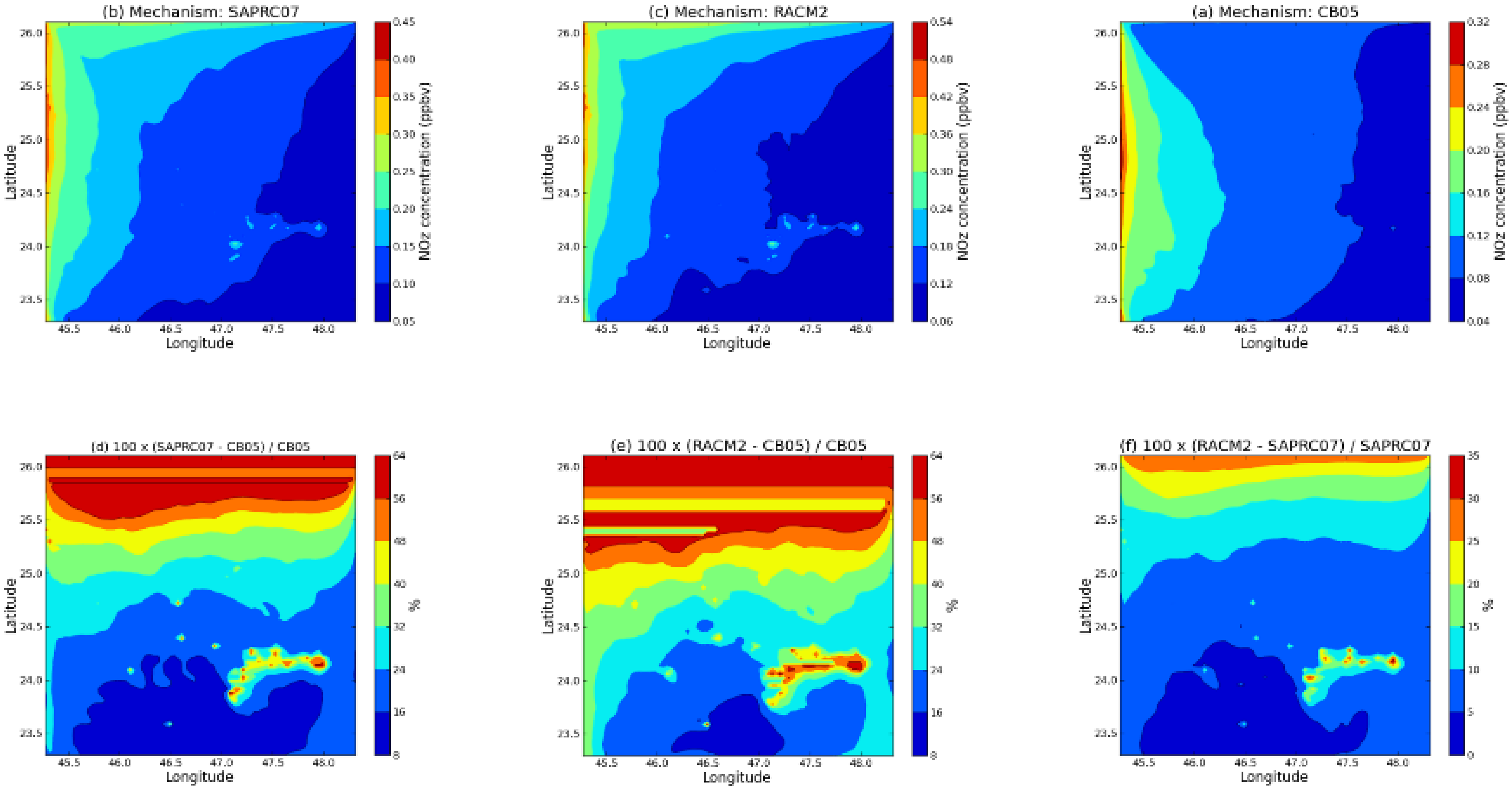

Figure 5.6 Spatial Distribution of Predicted Mean NO_z Concentrations Obtained with Chemical Mechanisms a) SAPRC07 b) RACM2 c) CB05 and Percent Differences between the Mechanisms e) SAPRC07 and CB05 e) RACM2 and CB05 f) RACM2 and SAPRC07

5.3.3 Formation of O_3

5.3.3.1 Effect on Surface O_3

As shown in Figure 5.2 and Table 5.2, SAPRC07 produced the highest O_3 concentration, followed by RACM2 and CB05. SAPRC07 produced approximately 3% more O_3 than RACM2 and approximately 10% more than CB05. RACM2 predictions were by 7% over CB05. Comparing RACM2 and CB05 mechanisms in the US domain, Sarwar et al., (2013) found RACM2 predicted 10% more O_3 than CB05. Kim et al., (2009) also compared O_3 and observed that RACM2 predicts higher concentration than CB05 in California. The reasons for high production of O_3 could be summarized as follows:

1. The production and destruction of O_3 is primarily governed by reactions of NO and NO_2 with other molecules including O_3 such as the reaction O_3 + NO. This reaction has lower reaction rate in RACM2 when compared to CB05 and SAPRC07, and this lower reaction rate keeps the concentration of O_3 high.
2. NO_2 is the primary source for producing O, if it reacts with other molecule such as OH, the O_3 concentrations will be lower. In RACM2 the reaction rate of NO_2 + OH is lower, thus more NO_2 is available for photolysis, subsequently producing more O_3.
3. NO_2 can also be produced through organic compounds (RO2) by the conversion of NO; these conversions are higher in RACM2, especially by aromatic compounds.
4. The organic nitrates recycling reactions are also higher in RACM2.

Similar reasons were outlined by Kim et al., (2009), Shearer et al., (2012), and Sarwar et al, (2013) to explain the higher O_3 production by RACM2 compared to CB05. In the current study, as well, RACM2 produced higher than CB05, however, the percent differences were larger. In addition to faster photolysis due to high temperature, the reaction NO_2 + OH is further slowed down, likely due to the shortage of OH radical in the atmosphere, as the region is dry. Kim et al., (2009) studied the effect of condensing the updated SAPRC07 mechanism and found that it produced greater O_3 concentration, the reasons of which were not evaluated. In the current study, SAPRC07 produced the highest concentration over RACM2 and CB05. Explanations 1 and 2 mentioned above for high O_3 concentration cannot be the reasons as reaction rates for SAPRC07 is equal to CB05 rates. In fact, SAPRC07 should produce similar O_3 concentration to CB05; however, it produces less O_3 even than RACM2. However, the role of organic compounds and NO_x recycling from organic nitrates seems to be predominant in SAPRC07, thus producing more NO_2 (e.g. from HNO_4) which in turn is the reason for the formation of O_3. Further analysis on this aspect is required to gain insights by performing sensitivity analysis on these reactions.

Over the course of one month, O_3 data was collected in the field at three stations in the domain. The mean O_3 concentration at the three locations was 39.16 ppbv. This observed value is about 6% and 2% more than the predicted values by CB05 and RACM2 respectively; however, it is 2.5% less than the SAPRC07 predicted value.

Spatial variations of the mean O_3 predicted by the three mechanisms are shown in Figure 5.7.

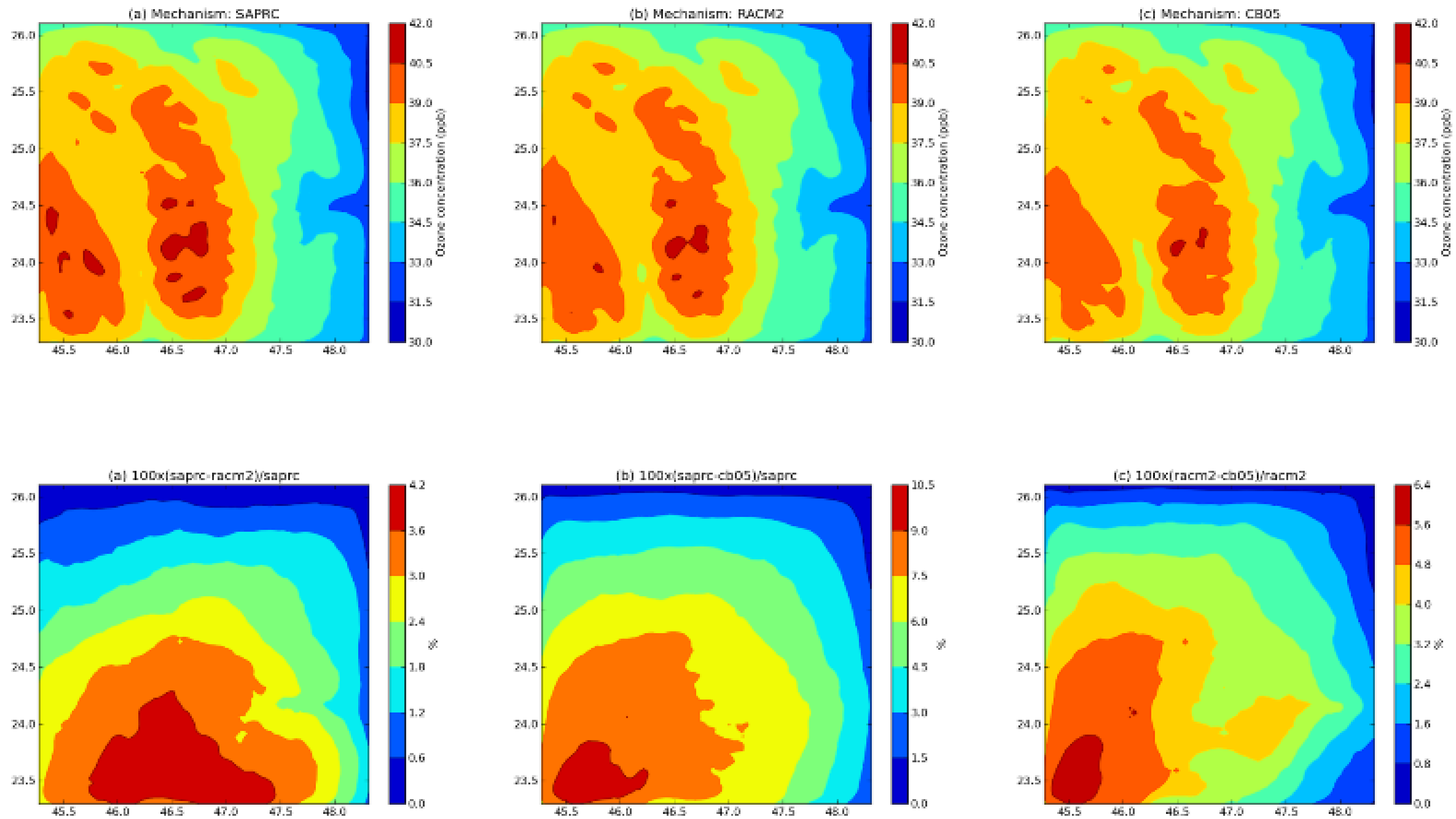

Figure 5.7 Spatial Distribution of Predicted mean O_3 Concentrations Obtained with Chemical Mechanisms a) SAPRC07 b) RACM2 c) CB05 and Percent Differences between the Mechanisms e) SAPRC07 and CB05 e) RACM2 and CB05 f) RACM2 and SAPRC07

The peak concentrations were generally in the middle and towards the west (check wind direction) of the domain. This is likely due to the predominant wind direction that was from the northeast which drives the O_3 concentration from north to south. All the three mechanisms share similar spatial distribution pattern, with SAPRC07 having the larger patches of peak concentrations. Figure 5.7 also illustrates the spatial differences between the mechanisms and differences were high towards south of the domain.

5.3.3.2 Diurnal Variation of O_3

Figure 5.8 shows boxplots of hourly diurnal O_3 predictions obtained with the six chemical mechanisms. The O_3 predicted with all the mechanisms takes a general pattern over the day increasing after sunrise, reaching to a maximum at noontime, and subsiding towards the evening. From midnight to 4 am (sunrise), there was no effect of the chemical mechanisms as O_3 concentrations were same. Immediately after sunrise CB05 started producing more O_3 than the others did, and as the day progressed all variations of SAPRC07 (SAPRC07TB, SAPRC07TC, and SAPRC07TIC) produced higher concentrations over the other two i.e., RACM2 and CB05. The concentration differences between various mechanisms were highest during noontime and close to zero during midnight, indicating that the reaction rates in the formation of O_3 are sensitive to temperatures. The reactions in SAPRC07 and RACM2 under high temperature produced more O_3, while CB05 had no significant change due to high temperatures. The organic aromatic reactions (converting NO to NO_2) appeared to take precedence in SAPRC07 and RACM2 under high temperatures. Figure 5.9 illustrates the diurnal variation including the observed data.

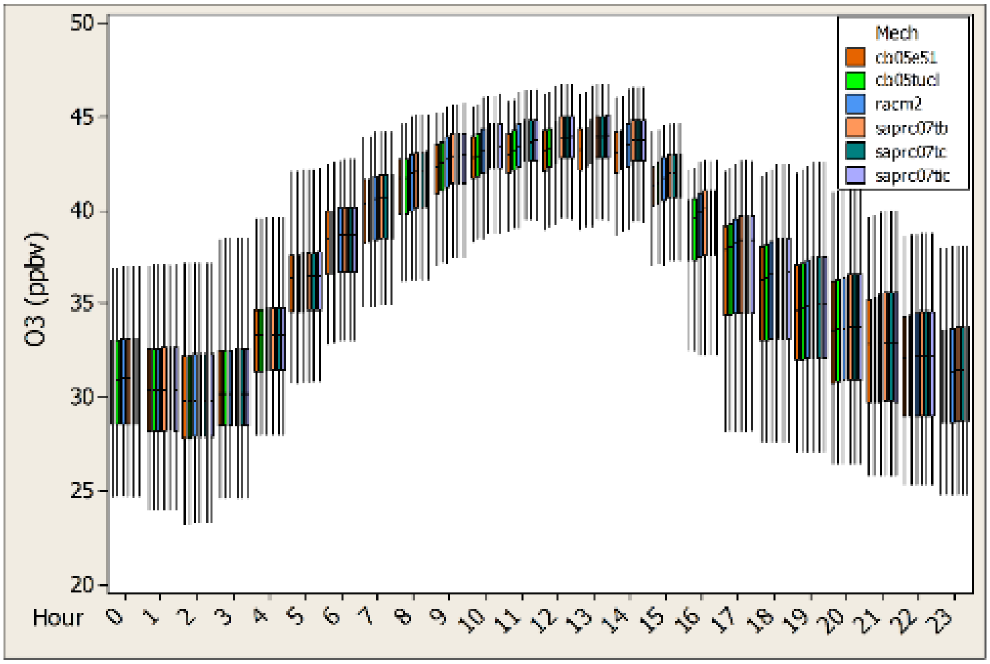

Figure 5.8 Comparison of Diurnal Variation of Predicted Hourly Surface O_3 Obtained with Six Chemical Mechanisms.

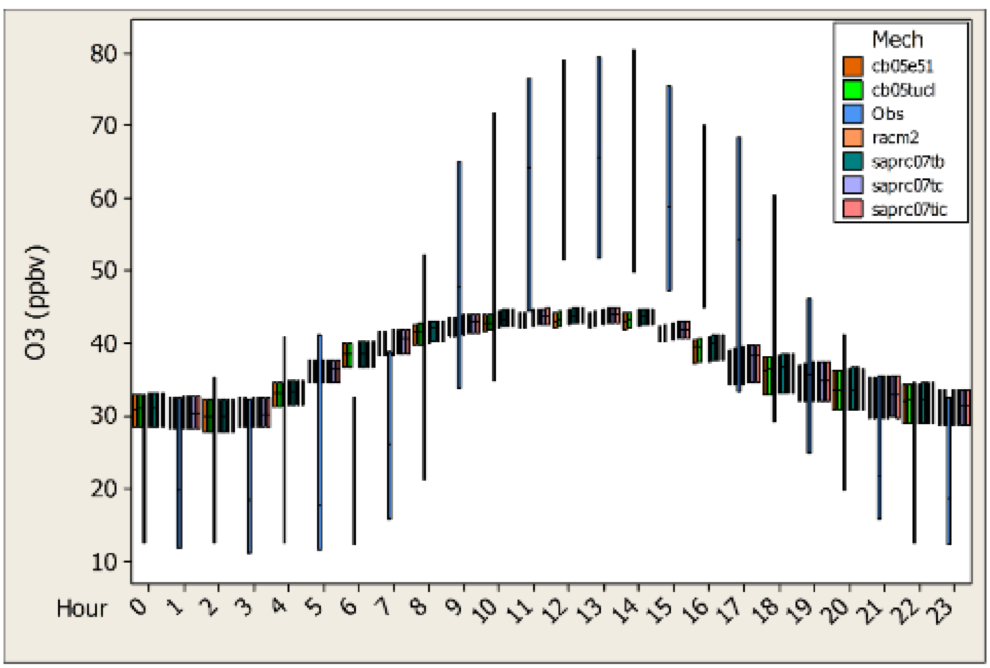

Figure 5.9 Comparison of Diurnal Variation of Predicted Hourly Surface O_3 Obtained with Six Chemical Mechanisms and Observed Data.

Generally, the observed data was scattered more than the model values. There is significant difference in the observed and model predicted values and this difference is anticipated as the model simulations were performed with only biogenic emissions inventory. During nighttime, the observed values are lower or similar to model values, and there is a significant drop in the concentration in the early morning. Early morning O_3 loss is a well-known phenomenon that is also applicable in Riyadh. There is a huge increase in O_3 concentration during the day (from 8 to 17 hours). This increase is due to daytime activities most likely the automobile traffic. Evening and late night values are similar to the model predictions.

Two things can be inferred from this: firstly, that the biogenic emissions produce substantial O_3 concentrations, in this case up to 40 ppbv, and secondly, that the spike of observed values during daytime (up to 65%) indicates significant anthropogenic contributions.

5.3.3.3 Vertical Distribution of O_3

Figure 5.10 presents the vertical profiles of O_3 predicted by SAPRC07, RACM2, and CB05. These are averaged over the entire domain and modelling period. As depicted in the figure, SAPRC07 continued to enhance O_3 over RACM2 and CB05 till approximately 12,000 m, and above that, the three mechanisms produced almost same O_3 concentrations. The average SAPRC07 enhancement was approximately 1-2 ppbv and 4-5 ppbv over RACM2 and CB05 respectively. Thus, vertically, SAPRC07 also produced higher O_3 concentrations than other mechanisms.

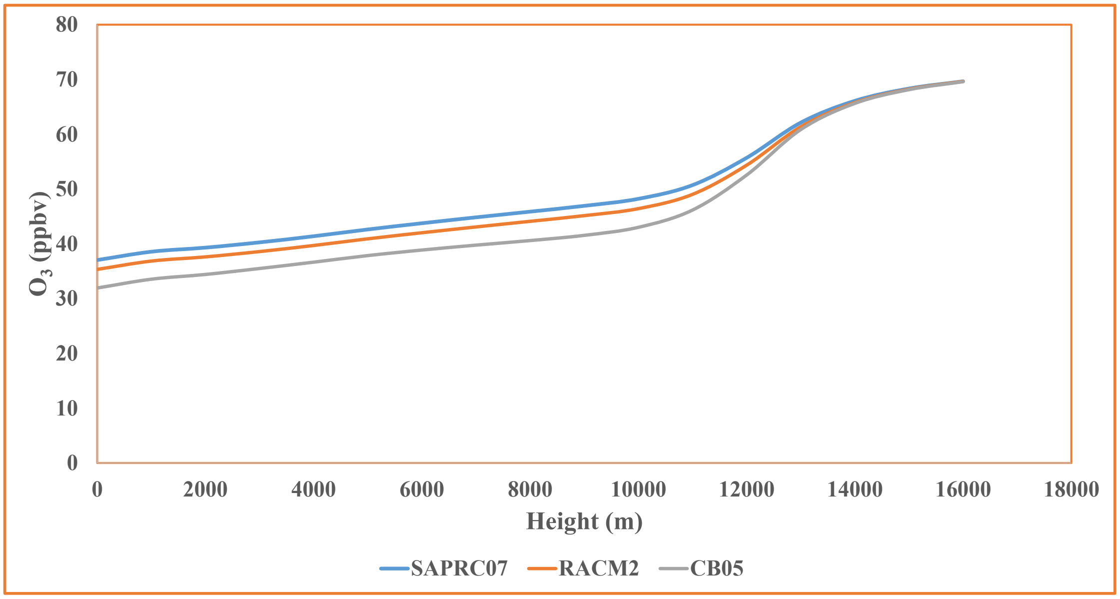

Figure 5.10 Domain-Wide Mean Predicted Vertical O_3 Profile Obtained with SAPRC07, RACM2, and CB05 Chemical Mechanisms during the Modelling Period.

5.3.3.4 Ozone Production Efficiency (OPE)

The conditions under which O_3 forms can be determined by calculating OPE. OPE is defined as the number of molecules of oxidant ($O_3 + NO_2$) produced photochemically when molecules of NO_x are oxidized (Kleinman, et al., 2002). It is generally calculated from the slope of linear regression relationship between daytime O_3 and NO_z concentration for aged air masses (O_3/NO_x>46) (Arnold and Dennis, 2006). Figure 5.11 shows the average OPE calculated over the entire domain and modelling period. The OPE values for CB05, SAPRC07, and RACM2 were 36.5, 19.7, and 13.2 respectively. The observation data was not sufficient to calculate OPE. When compared with other studies OPE values were high. This can potentially be due to the dry weather conditions of the study area. It is also noticed that CB05 produced more O_3 as NO_z increased and this indicates that CB05 is more sensitive to NO_z values in the formation of O_3 than RACM2 and SAPRC07. However, the NO_z produced is lesser in CB05 compared to SAPRC07 and RACM2, thus it produces lower O_3 concentrations.

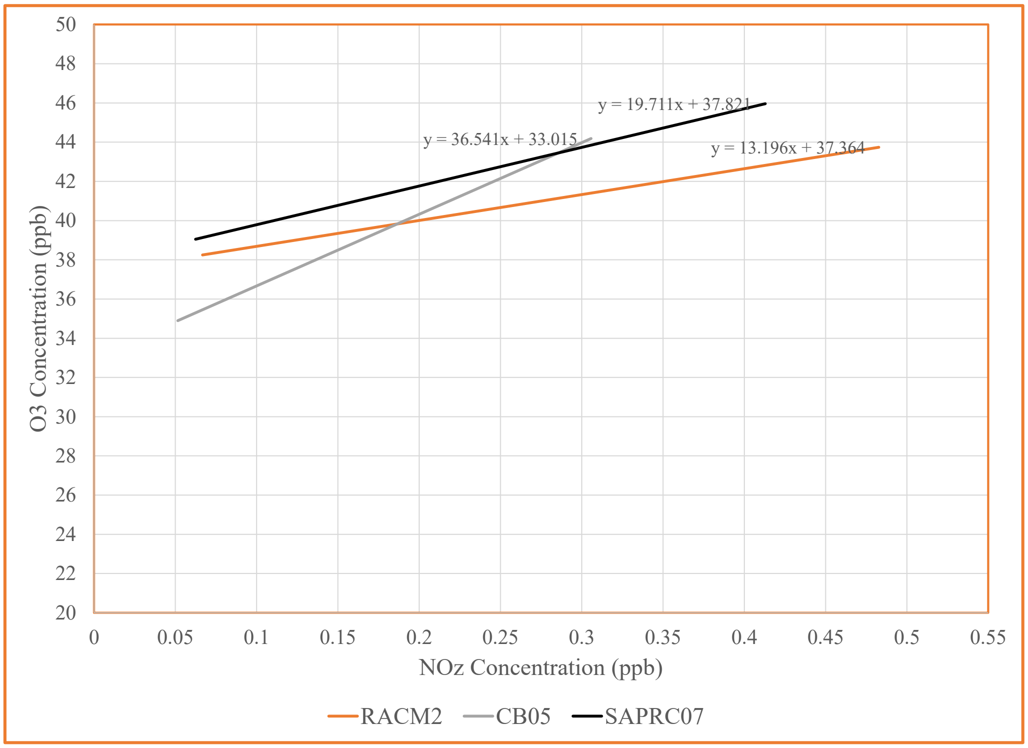

Figure 5.11 Domain-wide Mean O_3 Production Efficiency for three Chemical Mechanisms.

5.4 Summary

This chapter investigated the effect of various chemical mechanisms in CMAQ when implemented in the arid region of central Saudi Arabia. One month simulations were performed for six different chemical mechanisms and the predicted values were compared for oxidants (OH and H_2O_2), nitrogen species (PAN and NO_z), and O_3 (diurnal variation, surface distribution and vertical variation). The mechanism CB05TUC produced more oxidants and nitrogen species than CB05E51; however, both mechanisms predicted the same O_3 concentrations. There was no significant difference in the production of any of the parameters between SAPRC07TB, SAPRC07TC, and SAPRC07TIC. RACM2 produced higher OH concentrations than the other mechanisms, but the enhancements were much less than other studies. This indicates the shortage of the OH radical in the area is seemingly due to the arid conditions. Higher concentrations of the H_2O_2 radicals were produced by RACM2, due to the reaction of O_3 with alkenes, implying the predominant role of organic compounds in the atmosphere. High PAN concentrations were noticed in the domain by all mechanisms, indicating photochemical smog conditions in certain locations. SAPRC07 produced the highest concentration of surface O_3 followed by RACM2 and CB05. A similar pattern was noticed in the vertical variation of O_3. When compared with the observed O_3, RACM2 predictions were the closest. Diurnal variation indicated significant spike in O_3 during daytime verifying that automobile activities contribute significantly to O_3 formation. OPE values were very high compared to other studies. Based on the current comparisons, RACM2 appear to be the appropriate chemical mechanism to run photochemical models for O_3 predictions in dry and arid areas such as the current study area.

CHAPTER 6: PARAMETRIC UNCERTAINTIES AND REDUCED FORM MODEL

As discussed in Section 2.2, the heterogeneous reaction between minerals in dust and NO_2 influences the formation of O_3 in the atmosphere. Since this factor has not been taken into account by PAQM, especially CMAQ, this could be investigated through a RFM. In this chapter, parametric uncertainty coefficients are computed and analyzed in detail. Subsequently a continuum RFM is developed to characterize parametric uncertainties and is validated against the CMAQ runs. Through probabilistic framework, the likelihood of the impact on O_3 formation is also evaluated.

6.1 Parametric Uncertainties

In the formation of O_3, the parametric uncertainty (emission rates, reaction rate constants, initial and boundary conditions) plays a relatively larger role compared to structural uncertainty (model formulation, chemical mechanisms, deposition schemes etc.). This is because the formation mechanisms are generally well established in PAQM, while input parameters are highly uncertain. Several input parameters, such as emission rates, reaction rates, and photolysis frequencies contribute to the uncertainty of O_3 responsiveness to emissions perturbations. Sensitive coefficients and impact factors are important in the development and validation of RFM (discussed in Section 6.2). These coefficients were computed for each of the parameters, as discussed below.

6.1.1 Sensitivities and Impact Factors

The first order sensitivity ($S_j^{(1)}$), second order sensitivity ($S_{i,j}^{(2)}$), cross sensitivity ($S_{j,k}^{(2)}$), and impact factors (IF) were calculated based on the following equations where, $\epsilon_j =$

Fractional change in targeted emission rate (E_j); $\emptyset_k$= Fractional error in input parameter (P_k).

$$S_j^{(1)} = \frac{\partial C}{\partial \epsilon_j} \tag{6. 1}$$

$$S_{i,j}^{(2)} = \frac{\partial^2 C}{\partial \epsilon_j^2} \tag{6. 2}$$

$$S_{j,k}^{(2)} = \frac{\partial^2 C}{\partial \epsilon_j \partial \emptyset_k} \tag{6. 3}$$

$$\mathrm{IF} = \frac{S_{j,k}^{(2)}}{S_j^{(1)}} \tag{6. 4}$$

CMAQ Decoupled Direct Method (CMAQ-DDM) is an add-in to the base model CMAQ that calculates sensitivity coefficients simultaneously while air pollutant concentrations are being computed. It has been proved accurate and computationally efficient in calculating the first and second order sensitivities to O_3 (Cohan et al., 2005; Napelenok and Cohan, 2008). In this study, CMAQ-DDM was used to compute sensitivity coefficients for all the uncertain input parameters, including emissions rates, reaction rate constants, photolysis rates, and aerosols concentrations. Cross sensitivities were also computed to assess the relative impact of each of the selected input parameters on O_3 sensitivity to NO_x and aerosol emissions. These coefficients were calculated for the maximum 8-hour average concentration in each of the grid points in the modelling domain. The IF denotes the fractional change in first order sensitivity due to 1-sigma change in each input parameter (Digar, et al., 2011), as illustrated in Eq. 6.4. IF was used to identify the significance of the role of the input parameters on the formation of O_3.

6.1.2 Cross Sensitivities to NO_x Emissions

6.1.2.1 Photolysis Frequencies

The maximum first and second order sensitivity coefficients for the combined photolysis were estimated as 20.313 and -3.940 respectively and the cross sensitivity to NO_x and impact factor were 15.696 and 3.369 respectively, as shown in Table 6.1. These coefficients are high when compared to other studies (Hanna et al., 2001; Deguillaume et al., 2007); the primary reason could be the high solar radiations. In order to identify the specific photolysis reactions contributing to the formation of O_3, detailed sensitivities of each of the photolysis reactions were also computed, as presented in Table 6.1. It is observed that the sensitivity coefficients of the photolysis reactions R9, R74, R1, R36, R25, and R52 are relatively higher than other reactions and presumably play higher roles in photolysis.

Table 6.1 Photolysis Reactions and Cross Sensitivities to NO_x Emissions

Reaction	SJ1	SJ2	SJK_NO_x	Impact Factor
Combined	2.122E+01	-3.941E+00	1.696E+01	3.369E+00
<R9>O3=O1D	6.910E+00	-7.696E-01	1.032E+01	2.270E+00
<R74>FORM=2.000*HO2+CO	2.699E+00	-1.828E-01	2.726E+00	5.999E-01
<R1>NO2=NO+O	1.027E+01	-3.204E+00	1.856E+00	4.084E-01
<R36>H2O2=2.000*OH	8.261E-01	-5.093E-02	4.632E-01	1.019E-01
<R25>HONO=NO+OH	1.688E-01	-4.280E-02	1.708E-01	3.758E-02
<R86>ALD2=MEO2+CO+HO2	9.243E-02	-6.314E-04	8.782E-02	1.932E-02
<R71>MEPX=FORM+HO2+OH	5.829E-02	-1.105E-03	4.240E-02	9.329E-03
<R101>ALDX=MEO2+CO+HO2	7.509E-02	-1.833E-03	3.278E-02	7.213E-03
<R64>ROOH=OH+HO2+0.500*ALD2+0.500*ALDX	4.260E-02	-8.853E-04	2.301E-02	5.064E-03
<R14>NO3=NO2+O	6.468E-02	-3.179E-02	1.168E-02	2.570E-03
<R52>HNO3=OH+NO2	1.161E-01	-3.633E-04	7.952E-03	1.750E-03
<R51>PNA=0.610*HO2+0.610*NO2+0.390*OH+0.390*NO3	2.228E-04	-1.202E-07	3.680E-05	8.097E-06
<R141>CRPX=CRNO+OH	2.361E-06	2.457E-06	9.264E-06	2.038E-06
<R53>N2O5=NO2+NO3	1.475E-06	1.045E-07	3.051E-06	6.713E-07
<R105>PANX=CXO3+NO2	4.480E-04	-4.767E-07	-1.287E-05	-2.832E-06
<R90>PAN=C2O3+NO2	1.517E-03	-4.656E-06	-1.034E-04	-2.274E-05
<R8>O3=O	-1.568E-03	4.396E-05	-1.057E-03	-2.326E-04
<R62>NTR=NO2+HO2+0.330*FORM+0.330*ALD2+0.330*ALDX-0.660*PAR	3.444E-02	-8.120E-04	-2.064E-03	-4.540E-04
<R15>NO3=NO	-2.391E-02	1.068E-02	-5.273E-02	-1.160E-02
<R75>FORM=CO	-1.183E-01	3.361E-01	-3.709E-01	-8.161E-02

It is well known that the R1 (NO_2=NO + O) is the major photolysis reaction in the formation of O_3, which is also the case in the current scenario. The reaction with second highest sensitivity values is R9 (O_3=O1D), implying there is a significant role of excited monoatomic oxygen (O1D) in the formation of O_3 when compared to reaction R8 (O_3=O). O_3 is known to disassociate into O1D at a threshold wavelength of about 305 nm (Seinfeld and Pandis, 2006). O1D is highly reactive. It reacts with relatively stable species such as H_2O and N_2O and forms NO and OH undergoing the following reactions.

$O_3 + h\upsilon \rightarrow O_2 + O1D$

$O1D + H_2O \rightarrow OH + OH$

$O1D + N_2O \rightarrow NO + NO$

The ground state monoatomic oxygen (O) can also react with H_2O, but the reaction is endothermic and very slow. The sensitivity values for R8 are negative, indicating that this reaction is very slow and plays a role in the destruction of O_3 rather than formation. The O_3 response to NO_x emissions is also sensitive to formaldehyde (FORM). As per the reaction R74, FORM photodissociates into HO_2 and CO, and the reaction R36 produces OH radicals. Both HO_2 and OH radicals increase the production of O_3 (as discussed in the next section). Other reactions R25 and R52 contribute to the O_3 response as well. Two reactions R8 and R15 have negative coefficients indicating that these reactions reduce the O_3 formation but their absolute values are very low. The above analysis implies the following:

- The wavelength of the solar radiation in the atmosphere is such that it promotes the formation of O1D in greater quantity than the O molecule, indicating that the type of wavelength of solar radiation in arid regions enhances the production of O_3.
- There are more NO and OH molecules in the atmosphere due to the reaction of O1D with H_2O and N_2O.
- Photodissociation of FORM, H_2O_2, HONO and ALDX also have substantial roles in O_3 response to NO_x emissions.
- Only two photolysis reactions have negative values and both are very small indicating photolysis reactions mainly promote the formation of O_3.

6.1.2.2 Reactions

The selected reactions that have high positive impact (IF > 0.01) on the formation of O_3 to NO_x emissions are shown in Table 6.2. As observed from Table 6.2, many reactions are highly sensitive to NO_x in the formation of O_3. The reactions R10, R11, R22, R30, and R66 have very high impact factors. All these reactions produce radicals that promote the formation of O_3. For example, in the reaction R11 O1D produced due to photolysis (section 6.2.2) reacts with H_2O to form OH radical, which in turn reacts with CH_4 (R66) producing organic compounds known to enhance O_3 formation. In addition, O1D produced the O molecule, which is another main source of O_3 formation (R2).

Table 6.2 Selected Reactions and Positive Cross Sensitivities to NO_x Emissions

Reaction	SJ1	SJ2	SJK_NO_x	Impact Factor
<R11>O1D+H2O=2.000*OH	6.558	-1.047	9.792	2.155
<R10>O1D+M=O+M	0.413	8.965	4.712	1.037
<R66>OH+CH4=MEO2	6.831	-0.281	3.544	0.780
<R30>HO2+NO=OH+NO2	5.453	-2.075	1.125	0.248
<R65>OH+CO=HO2	4.982	-0.081	1.031	0.227
<R2>O+O2+M=O3+M	0.329	-0.015	0.703	0.155
<R22>NO+NO+O2=2.000*NO2	0.421	0.000	0.664	0.146
<R112>PAR+OH=0.870*XO2+0.130*XO2N+0.110*HO2+0.060*ALD2-0.110*PAR+0.760*ROR+0.050*ALDX	0.757	-0.074	0.519	0.114
<R39>OH+H2=HO2	0.470	-0.004	0.231	0.051
<R84>ALD2+OH=C2O3	0.268	-0.056	0.200	0.044
<R29>OH+HNO3=NO3	0.237	0.004	0.190	0.042
<R113>ROR=0.960*XO2+0.600*ALD2+0.940*HO2-2.100*PAR+0.040*XO2N+0.020*ROR+0.500*ALDX	0.162	-0.045	0.105	0.023
<R37>OH+H2O2=HO2	0.079	-0.007	0.087	0.019
<R16>NO3+NO=2.000*NO2	0.092	-0.007	0.079	0.017
<R19>N2O5+H2O=2.000*HNO3	0.001	0.003	0.067	0.015
<R99>ALDX+OH=CXO3	0.089	-0.017	0.051	0.011

Table 6.3 presents the reactions which have negative impacts (IF >-0.01). The significant reactions that consume O_3 are R28, R3, R13, and R12. NO is the main compound which reacts with O_3 (R7), and this NO is produced mainly by R4. By observing Table 6.2 and Table 6.3, it can be inferred that there are more reactions promoting the formation of O_3 with cumulatively high impact than the reactions that consume O_3, thus there is a net positive O_3 formation.

Table 6.3 Selected Reactions and Negative Cross Sensitivities to NO_x Emissions

Reaction	SJ1	SJ2	SJK_NO_x	Impact Factor
<R28>NO2+OH=HNO3	-4.661	15.724	-4.695	-1.033
<R3>O3+NO=NO2	-4.541	10.038	-2.076	-0.457
<R7>NO2+O3=NO3	-0.122	0.322	-0.787	-0.173
<R13>O3+HO2=OH	-0.651	0.156	-0.645	-0.142
<R34>HO2+HO2=H2O2	-0.302	0.233	-0.461	-0.101
<R43>OH+HO2=	-0.330	0.545	-0.432	-0.095
<R73>FORM+OH=HO2+CO	-0.013	0.508	-0.356	-0.078
<R68>MEO2+HO2=MEPX	-0.290	0.249	-0.277	-0.061
<R12>O3+OH=HO2	-0.308	0.069	-0.247	-0.054
<R88>C2O3+NO2=PAN	-0.091	0.179	-0.196	-0.043
<R26>OH+HONO=NO2	-0.010	0.015	-0.139	-0.030
<R56>XO2+HO2=ROOH	-0.026	0.106	-0.130	-0.029
<R35>HO2+HO2+H2O=H2O2	-0.135	0.022	-0.111	-0.024
<R103>CXO3+NO2=PANX	-0.057	0.080	-0.090	-0.020
<R4>O+NO2=NO	-0.006	0.061	-0.085	-0.019
<R24>NO+OH=HONO	-0.009	0.010	-0.083	-0.018
<R17>NO3+NO2=NO+NO2	-0.003	0.064	-0.061	-0.013
<R55>XO2N+NO=NTR	-0.025	0.097	-0.059	-0.013
<R91>C2O3+HO2=0.800*PACD+0.200*AACD+0.200*O3	-0.024	0.019	-0.047	-0.010
<R114>ROR=HO2	-0.034	0.141	-0.044	-0.010

6.1.2.3 Aerosols

Cross sensitives of aerosols emissions to NO_x emissions were computed to analyze the role of aerosols. The only species that had a cross sensitivity value greater than zero is ANO3J (fine mode nitrate). The first and second order sensitivity values were 4.73E-06 and 1.14E-13 respectively. The cross sensitivity to NO_x emissions was 1.79E-10. All the values were low, but positive, indicating a small role of aerosol species (fine mode nitrate) in the formation of O_3 (further discussed in the next section).

6.1.3 Cross Sensitivities to Aerosol Emissions

In order to understand the role of aerosols in the formation of O_3, cross sensitivities of various parameters to aerosols emissions were computed. As discussed in Section 6.1.2.3, the only aerosol species that had a positive sensitivity is the fine-mode nitrate species (ANO3J), hence the cross sensitivities are primarily for this species. Table 6.4 presents the first order, second order, and cross sensitivity coefficients for the photolysis reactions while Table 6.5 shows the same for various other reactions. The last column in the tables shows percent change in IF of aerosol emissions to NO_x emissions (100 * IF_{AER} - $IF_{NO_x}$is / IF_{NO_x}). This compares the role of aerosol emissions with NO_x emissions in the formation of O_3. IF_{AER} is the IF for aerosols cross sensitivities and $IF_{NO_x}$is the IF for NO_x cross sensitivities.

In general, the cross-sensitivity coefficients for both photolysis and other reactions were very low; however, the IFs were significant for some photolysis reactions and other chemical reactions. As per Table 6.4, the sequence of photolysis with respect to IF was similar to the IF estimate for cross sensitivities with NO_x emissions (Table 6.1 and Table 6.2), however, the percent change varied. The significant positive change in IFs were for reactions R52 and R14 (given below), and the percent change in IF was equal to 99% and 85 % respectively.

<R52> $HNO_3 = OH + NO_2$

<R14> $NO_3 = NO_2 + O$

Table 6.4 Photolysis Reactions and Cross Sensitivities to Aerosol Emissions

Reaction	SJ1	SJ2	SJK_Aer	Impact Factor
<R9>O3=O1D	6.910E+00	-7.696E-01	5.223E-06	1.455E+00
<R52>HNO3=OH+NO2	1.161E-01	-3.633E-04	2.351E-06	6.549E-01
<R1>NO2=NO+O	1.027E+01	-3.204E+00	1.629E-06	4.537E-01
<R74>FORM=2.000*HO2+CO	2.699E+00	-1.828E-01	1.291E-06	3.597E-01
<R36>H2O2=2.000*OH	8.261E-01	-5.093E-02	2.455E-07	6.838E-02
<R25>HONO=NO+OH	1.688E-01	-4.280E-02	9.119E-08	2.540E-02
<R14>NO3=NO2+O	6.468E-02	-3.179E-02	6.410E-08	1.786E-02
<R86>ALD2=MEO2+CO+HO2	9.243E-02	-6.314E-04	3.501E-08	9.752E-03
<R101>ALDX=MEO2+CO+HO2	7.509E-02	-1.833E-03	2.407E-08	6.705E-03
<R71>MEPX=FORM+HO2+OH	5.829E-02	-1.105E-03	2.236E-08	6.229E-03
<R64>ROOH=OH+HO2+0.500*ALD2+0.500*ALDX	4.260E-02	-8.853E-04	1.660E-08	4.625E-03
<R15>NO3=NO	-2.391E-02	1.068E-02	7.894E-09	2.199E-03
<R62>NTR=NO2+HO2+0.330*FORM+0.330*ALD2+0.330*ALDX-0.660*PAR	3.444E-02	-8.120E-04	2.472E-10	6.886E-05
<R51>PNA=0.610*HO2+0.610*NO2+0.390*OH+0.390*NO3	2.228E-04	-1.202E-07	8.423E-11	2.346E-05
<R105>PANX=CXO3+NO2	4.480E-04	-4.767E-07	1.487E-11	4.143E-06
<R90>PAN=C2O3+NO2	1.517E-03	-4.656E-06	1.338E-11	3.728E-06
<R53>N2O5=NO2+NO3	1.475E-06	1.045E-07	4.188E-12	1.167E-06
<R141>CRPX=CRNO+OH	2.361E-06	2.457E-06	3.485E-12	9.707E-07
<R8>O3=O	-1.568E-03	4.396E-05	-1.408E-10	-3.922E-05
<R75>FORM=CO	-1.183E-01	3.361E-01	-2.803E-08	-7.808E-03

As per Table 6.5, the reaction R9, the photolysis of O_3 into O1D, has the highest IF similar to the NO_x emissions but 45% less. The reactions for which the IF increased significantly (when compared to NO_x cross sensitivities) were R29, R30, and R67, and the percent increase in the IF was 91%, 41%, and 69% respectively.

<R29> $OH + HNO_3 = NO_3$

<R30> $HO_2 + NO = OH + NO_2$

<R67>$MEO_2 + NO = FORM + HO_2 + NO_2$

Table 6.6 shows the reactions which have negative cross sensitivities with aerosol emissions, and the prominent reactions in this category were R28 and R3 with relatively large cross sensitivity values. The percent change in IF for these reactions was about 260% and 164% respectively.

<R28> $NO_2 + OH = HNO_3$

<R3> $O_3 + NO = NO_2$

The above reactions involve different forms of nitrate compounds. The aerosol emissions seem to be highly sensitive to the compounds HNO_3, NO_3, and NO. This presents an evidence of heterogeneous reactions occurring between these compounds and aerosol species (Eq. 2.20 to 2.23). In the presence of aerosols, the formation of HONO, the reaction of HNO_3, and the conversion of NO_2 (g) to NO (aq) will influence the overall formation of O_3. NO_x recycling is suppressed causing less production of O_3; it appears that this is because of the dust update of HNO_3, NO_3, and NO.

Table 6.5 Selected Reactions and Positive Cross Sensitivities to Aerosol Emissions

Reaction	SJ1	SJ2	SJK_Aer	Impact Factor	% change in impact factor
<R11>O1D+H2O=2.000*OH	6.558E+00	-1.047E+00	4.958E-06	1.381E+00	-56
<R29>OH+HNO3=NO3	2.366E-01	3.676E-03	1.592E-06	4.436E-01	91
<R66>OH+CH4=MEO2	6.831E+00	-2.805E-01	1.586E-06	4.419E-01	-76
<R30>HO2+NO=OH+NO2	5.453E+00	-2.075E+00	1.509E-06	4.202E-01	41
<R65>OH+CO=HO2	4.982E+00	-8.099E-02	8.192E-07	2.282E-01	1
<R10>O1D+M=O+M	4.130E-01	8.965E+00	6.194E-07	1.725E-01	-501
<R112>PAR+OH=0.870*XO2+0.130*XO2N+0.110*HO2+0.060*ALD2-0.110*PAR+0.760*ROR+0.050*ALDX	7.574E-01	-7.377E-02	1.690E-07	4.708E-02	-143
<R67>MEO2+NO=FORM+HO2+NO2	6.881E-01	-5.162E-01	1.108E-07	3.086E-02	69
<R2>O+O2+M=O3+M	3.291E-01	-1.469E-02	9.573E-08	2.667E-02	-480
<R16>NO3+NO=2.000*NO2	9.173E-02	-6.529E-03	5.219E-08	1.454E-02	-19
<R84>ALD2+OH=C2O3	2.684E-01	-5.633E-02	4.782E-08	1.332E-02	-230
<R113>ROR=0.960*XO2+0.600*ALD2+0.940*HO2-2.100*PAR+0.040*XO2N+0.020*ROR+0.500*ALDX	1.621E-01	-4.520E-02	3.871E-08	1.078E-02	-114
<R19>N2O5+H2O=2.000*HNO3	1.455E-03	3.350E-03	3.662E-08	1.020E-02	-45
<R87>C2O3+NO=MEO2+NO2	5.477E-01	-1.778E-01	3.598E-08	1.002E-02	39

Table 6.6 Selected Reactions and Negative Cross Sensitivities to Aerosol Emissions

Reaction	SJ1	SJ2	SJK_Aer	Impact Factor	% change in impact factor
<R28>NO2+OH=HNO3	-4.661E+00	1.572E+01	-1.031E-06	-2.873E-01	-260
<R3>O3+NO=NO2	-4.541E+00	1.004E+01	-6.227E-07	-1.735E-01	-163
<R13>O3+HO2=OH	-6.511E-01	1.556E-01	-1.745E-07	-4.862E-02	-192
<R43>OH+HO2=	-3.304E-01	5.446E-01	-8.634E-08	-2.405E-02	-295
<R88>C2O3+NO2=PAN	-9.071E-02	1.794E-01	-4.951E-08	-1.379E-02	-212
<R73>FORM+OH=HO2+CO	-1.263E-02	5.076E-01	-4.353E-08	-1.213E-02	-546

Earlier studies have also reported up to 40% reduction in O_3 due to these reactions (DeReus, et al., 2000; Umann, et al., 2005; Bonasoni, et al., 2004). The quantification of reduction or increase in O_3 will be studied through an RFM discussed in the following sections.

6.2 Reduced Form Model (RFM)

6.2.1 Development of RFM

An RFM is developed by incorporating uncertainties in the emissions with more than one input parameters. The Eq. 2.35 could be re-written as shown in the following Eq. 6.5.

$$\Delta C_{\varepsilon_j} = (1+\varphi_{\varepsilon j})\varepsilon_j S_{\varepsilon j}^{(1)} + (1+\varphi_{\varepsilon j})^2 \frac{\Delta\varepsilon_j^2}{2} S_{\varepsilon j}^{(2)} + (1+\varphi_{\varepsilon j})\varepsilon_j \sum_k \varphi_k \, S_{\varepsilon j,k}^{(2)} + \text{HOT} \quad (6.5)$$

Where,

ΔC_{ε_j} = Change in concentration of pollutants due to change in emissions ε_j

$\varphi_{\varepsilon j}$ = Fractional error in input parameter

$S_{\varepsilon j}^{(1)}$= First-order sensitivity of pollutant concentration to ε_j

$S_{\varepsilon j}^{(2)}$ = Second-order sensitivity of pollutant concentration to ε_j

$S_{\varepsilon j,k}^{(2)}$ = Cross sensitivity of uncertain parameter j with k with emissions

This equation is analogous to the response equation presented by Digar and Cohan (2010) and can be used to investigate the role of aerosol in O_3 response. A study by Cohan et al. (2005) applied this equation using CMAQ-DDM sensitivity coefficients to characterize the impact of parametric error on pollutant emission response considering only one uncertain parameter. In order to estimate the combined role of uncertainty in aerosol and NO_x emissions, Eq. 6.1 can be modified as follows.

$$\Delta C_{\varepsilon_j \omega_j} = (1+\varphi_{\varepsilon j})\varepsilon_j S_{\varepsilon j}^{(1)} + (1+\varphi_{\varepsilon j})^2 \frac{\Delta\varepsilon_j^2}{2} S_{\varepsilon j}^{(2)} + (1+\varphi_{\varepsilon j})\varepsilon_j \sum_k \varphi_{\varepsilon k}\, S_{\varepsilon j,k}^{(2)} + (1+\varphi_{\omega j})\omega_j S_{\omega j}^{(1)} + (1+\varphi_{\omega j})^2 \frac{\Delta\omega_j^2}{2} S_{\omega j}^{(2)} + (1+\varphi_{\omega j})\omega_j \sum_k \varphi_{\omega k}\, S_{\omega j,k}^{(2)} + \text{HOT} \quad (6.\ 6)$$

Where,

$\Delta C_{\varepsilon_j \omega_j}$ = Change in concentration due to change in emissions ε_j and aerosols ω_j

$\varphi_{\omega j}$ = Fractional error due to aerosols emission ω_j in input parameter

$S_{\omega j}^{(1)}$ = First-order sensitivity of pollutant concentration to ω_j

$S_{\omega j}^{(2)}$ = Second-order sensitivity of pollutant concentration to ω_j

$S_{\omega j,k}^{(2)}$= cross sensitivity coefficient of pollutant concentration to ωi and input parameter k

Assuming that the fractional error in the input parameter is same for both emissions, meaning $\varphi_{\varepsilon j} = \varphi_{\omega j} = \varphi_j$, and re-arranging Eq. 6.2 leads to Eq. 6.3.

$$\Delta C_{\varepsilon_j \omega_j} = (1+\varphi_j)\left(\varepsilon_j S_{\varepsilon j}^{(1)} + \omega_j S_{\omega j}^{(1)}\right) + (1+\varphi_j)^2 \left(\frac{\Delta\varepsilon_j^2}{2} S_{\varepsilon j}^{(2)} + \frac{\Delta\omega_j^2}{2} S_{\omega j}^{(2)}\right) + (1+\varphi_j)(\varepsilon_j \sum_k \varphi_{\varepsilon k}\, S_{\varepsilon j,k}^{(2)} + \omega_j \sum_k \varphi_{\omega k}\, S_{\omega j,k}^{(2)}) + \text{HOT} \quad (6.\ 7)$$

The above equation can be used to estimate a change in O_3 concentration for any amount of NO_x emission perturbations (ε_j) and or aerosol perturbations (ω_j). However, before any such estimates can be made, testing the accuracy of this equation is pivotal. If the equation proves accurate, it would facilitate instantaneous characterization of pollutant emissions and or aerosol emissions response over wide ranges of input uncertainty through Monte Carlo sampling of input parameters, as will be discussed in Section 6.3.

6.2.2 Evaluation of RFM

Section 6.1 discussed uncertain parameters and corresponding sensitivity coefficients to NO_x and aerosol emissions. As a result, the first order, second order, and cross sensitivity coefficients were computed for a number of different input parameters. These coefficients will be used to evaluate the developed RFM for NO_x emissions, aerosol emissions, and both combined. The steps followed for evaluating the RFM against the CMAQ runs are as follows:

- Compute sensitivity coefficients for various uncertain parameters.
- Run the CMAQ simulations for various emissions (increase or decrease) scenarios.
- Compute the BFD of O_3 concentration for model runs which is the difference between base simulation and controlled simulation, as given by the Eq. 6.8 where ΔC_{BF} = brute force difference, $C_{B,\emptyset_k P_k}$= concentration at base level, and $C_{R,\emptyset_k P_k}$= concentration at reduced level

$$\Delta C_{BF} = C_{B,\emptyset_k P_k} - C_{R,\emptyset_k P_k} \tag{6. 8}$$

- Compute RFM concentrations by the necessary RFM equations by simultaneously increasing all selected input parameters paired with corresponding NO_x reduction scenarios.

- Calculate statistical and linear regression parameters to compare BF and RFM values. The parameters employed for the comparison were Normalized Mean Bias (NMB), Normalized Mean Error (NME), Correlation Coefficient (r^2), Slope, and Intercept.

CMAQ simulations were performed by varying the emissions, but other input parameters in the model remained constant, as discussed in Chapter 4. All the values used for the comparison were averaged for daily 8-hour estimates after excluding the spin up period. Different types of uncertainties are considered for both NO_x and aerosol perturbations.

For NO_x control scenarios, the uncertainties are U1 (NO_x emissions), U2 (NO_x and VOC emissions), U3 (NO_x, VOC, and photolysis frequencies), and U4 (NO_x, VOC, photolysis frequencies, and reaction rates). For aerosol perturbation scenarios, the types of uncertainties considered U5 (aerosol emissions), U6 (aerosol emissions and photolysis), and U7 (aerosol emissions, photolysis, and reaction rates).

6.2.2.1 Perturbations in NO_x Emissions

The first case for testing the developed RFM is for NO_x emissions reduction scenarios. The CMAQ simulations were run for the central region of Saudi Arabia. This region is a NO_x sensitive region (Shareef et al., 2016), so O_3 is predominantly sensitive to NO_x emissions here. Hence, NO_x reduction scenarios were considered. CMAQ was run for the three scenarios, which were uniform reduction of NO_x emissions by 10%, 25%, and 50%. Simultaneous increases in all the selected input parameters of 10%, 25%, and 50% were considered and paired with the corresponding NO_x reduction scenarios. The steps discussed in the previous section were followed, and Table 6.7 presents the results of this analysis. The BFD of O_3 concentrations for 10%, 25%, and 50% NO_x reduction was -0.98 ppb, -2.62 ppb, and -5.87 ppb respectively, as shown in Table 6.7. For the uncertainty case U4, the 10%, 25%, and 50% reduction in NO_x emissions produced r^2 values of 0.920, 0.918 and 0.902 respectively indicating a good correlation between BF and RFM values. The corresponding NMB values were -2.34%, -4.43%, and 6.32% respectively and NME values were 5.85%, 7.37%, and 11.41% respectively, as shown in Table 6.7.

It was observed that the performance decreases as NO_x emissions increased, so RFM performs slightly better at lower reductions levels. The RFM model presented by Digar (2012) showed similar performance. It is known that due to imperfections in the CMAQ-DDM sensitivity coefficients, and the impact magnitudes' decline with targeted perturbations, the errors do not converge to 0% (Cohan, et al., 2005; Napelenok and D. S. Cohan, 2008). It was also observed that across the uncertainties, U1 to U4, the r^2 values increased. For example, for the 50% NO_x reduction scenario, the r^2 value for U1, U2, U3, and U4 were 0.9022, 0.9116, 0.9205, and 0.9299 respectively. This implies that RFM performs better if a higher number of uncertainties are included in the computations. It shows the importance of all the sensitivity coefficients to be included in RFM. Figure 6.1 illustrates the spatial plots for BFD (of the CMAQ runs), the RFM (incorporating uncertainties), and the difference between the two for 10% emission reduction.

Table 6.7 Performance of the RFM in Predicting the Impacts of Perturbation in NO_x Emissions on 8-Hour O_3 Concentrations

Change in NO_x Emissions	Uncertain Input Parameters	Change in input parameters	Impact of Reduction (ppb)		NMB (%)	NME (%)	r^2	Slope	Intercept
			BFD	RFM					
-10%	E_{NOx} (U1)	10%	-0.979	-0.825	2.34	5.85	0.9202	0.8707	0.1553
10%	E_{NOx}; E_{VOC} (U2)	10%	-0.979	-0.722	-2.32	5.85	0.9299	0.8758	0.1532
-10%	E_{NOx}; E_{VOC}; J_{PHOT} (U3)	10%	-0.979	-1.020	2.37	5.56	0.9323	0.8716	0.1564
-10%	E_{NOx}; E_{VOC}; J_{PHOT}; Reactions (U4)	10%	-0.979	-1.028	2.24	5.39	0.9415	0.903	0.1415
-25%	E_{NOx} (U1)	25%	-2.624	-2.033	4.43	7.37	0.9187	0.7507	0.5285
-25%	E_{NOx}; E_{VOC} (U2)	25%	-2.624	-1.752	4.41	7.27	0.9595	0.7782	0.5016
-25%	E_{NOx}; E_{VOC}; J_{PHOT} (U3)	25%	-2.624	-1.337	5.54	6.44	0.9628	0.8261	0.4687
-25%	E_{NOx}; E_{VOC}; J_{PHOT}; Reactions (U4)	25%	-2.624	-1.026	4.28	6.09	0.9322	0.9054	0.3695
-50%	E_{NOx} (U1)	50%	-5.871	-4.253	6.32	11.41	0.9022	0.1768	2.3199
-50%	E_{NOx}; E_{VOC} (U2)	50%	-5.871	-4.564	6.26	11.59	0.9116	0.2581	2.1746
-50%	E_{NOx}; E_{VOC}; J_{PHOT} (U3)	50%	-5.871	-4.236	6.59	12.87	0.9605	0.6784	1.4782
-50%	E_{NOx}; E_{VOC}; J_{PHOT}; Reactions (U4)	50%	-5.871	-4.786	6.03	12.82	0.9699	0.8532	1.0601

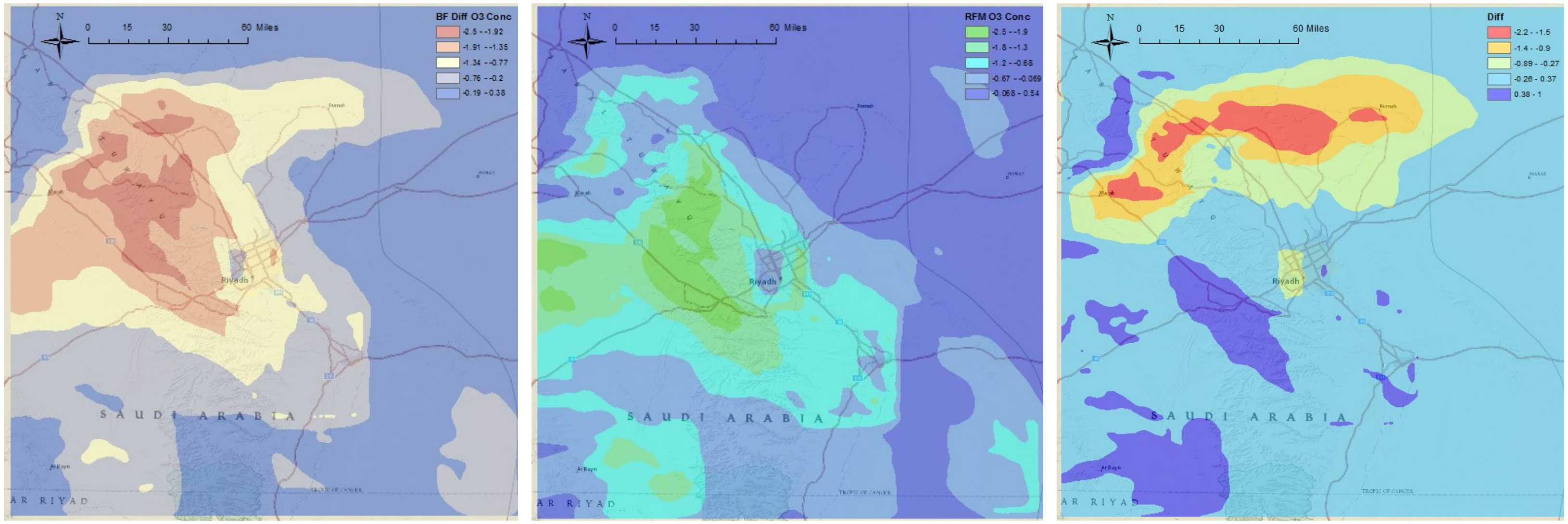

a b c

Figure 6.1 a) O_3 Reduction (ppb) from BF Difference of CMAQ Runs under 10% NO_x Reduction B) RFM Predictions C) Difference between BF and RFM Concentration

The plots show that the RFM model accurately represents the plume of O_3 reductions resulting from the NO_x reduction. As observed from the figure, RFM performed very well across the domain, however, there are areas where it deviated. The RFM overestimated in a few areas southwest of the domain and underestimated a few places in the north. The performance of RFM was good near the sources and in the proximity of population habitation (the center of the domain).

6.2.2.2 Perturbations in Aerosol Emissions

As discussed in Section 6.1, the only species in aerosols sensitive to O_3 is ANO3J (fine mode nitrate). The concentration of this species was increased by 10% to 500% for running the CMAQ simulations and BFD was calculated from the runs. The purpose of increasing aerosol concentrations in this scenario is to study the reduction of O_3 due to this increase. The BFD in O_3 concentration for 10%, 20%, 30%, 40%, 50%, 100%, 200%, 300%, 400%, and 500% increase in aerosol concentration was 0.1232 ppb, 0.0980 ppb, 0.0728 ppb, 0.1034 ppb, 0.1632 ppb, 0.2635 ppb, 0.2835 ppb, and 1.2031 ppb respectively. The impacts on O_3 concentrations due to the increase in aerosols emissions do not follow a linear pattern. The percent change in O_3 against percent increase in aerosols emissions is shown in Figure 6.2. The O_3 concentration decreases initially, up to aerosol increase of about 50%, and after that the concentration starts to increase. The percent increase in O_3 concentration is from about 8% to 30% with an increase of aerosol emissions from 300% to 500% respectively.

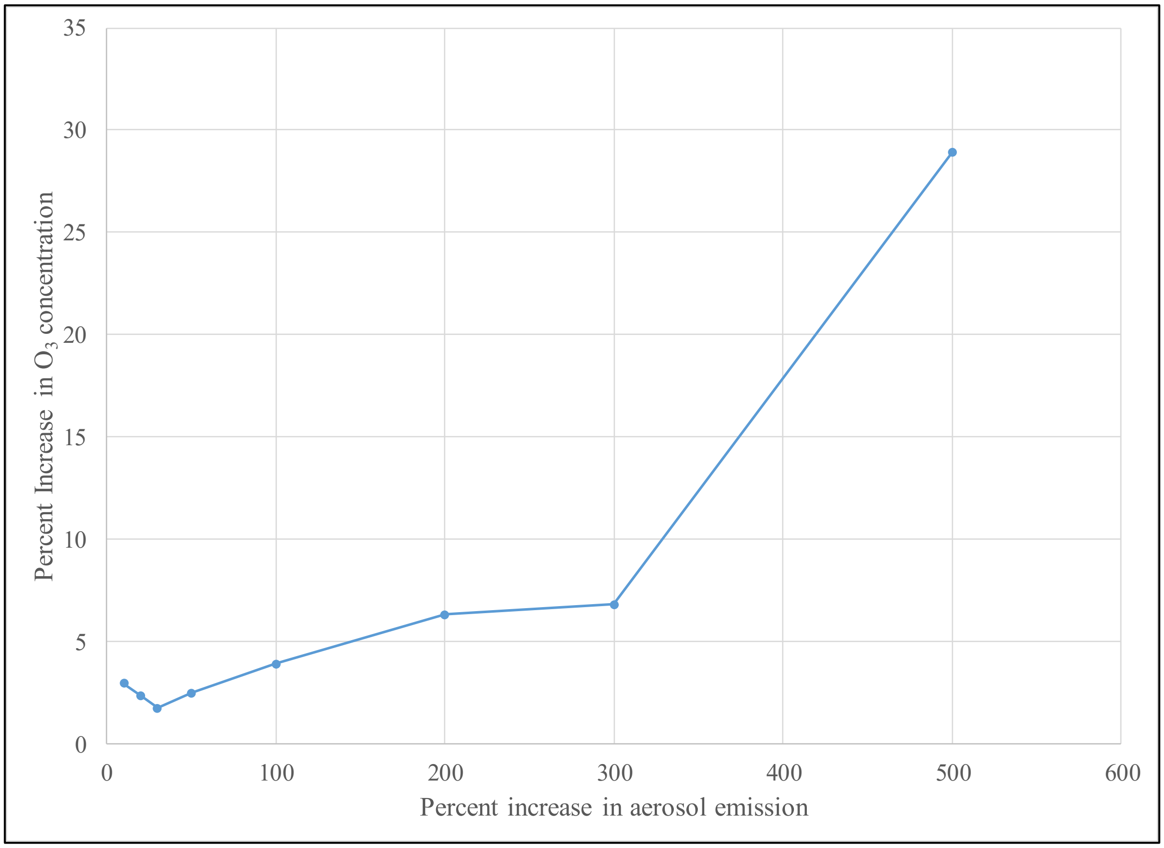

Figure 6.2 Relationship between the Percent Increase in O_3 Concentration with respect to the Percent Increase in Aerosol Concentrations

The reason for the nonlinear increase in O_3 concentration can be explained as follows. As discussed in Section 6.1.3, the heterogeneous reactions of dust with HNO_3, NO_3, and NO suppress the NO_x cycle resulting in less production of O_3. However, as the dust concentration increases (primarily ANO3J), it appears that this reaction halts; in turn, the resulting large number of nitrate compounds in the atmosphere promote the NO_x cycle.

The Eq. 6.5 was employed to compute the RFM values. For simplicity, only one case of uncertainty (U7) was considered in RFM. Table 6.8 presents the results and the statistical parameters of the comparisons. The r^2 values with respect to BFD averaged to about 0.862. In this case, RFM underperforms slightly for aerosol emission perturbations when compared to NO_x perturbations. The primary reason for this appears to be the low values of sensitivity coefficients for aerosols. The aerosol perturbations produced a low yet nonnegligible change in O_3 concentration. Similar to NO_x perturbations, the aerosol perturbations in the RFM model performed better at lower increase levels.

Table 6.8 Performance of the RFM in Predicting the Impacts of Perturbations in Aerosol Emissions on 8-Hour O_3 Concentrations

Change in aerosol Emissions	Uncertain Input Parameters	Change in input parameters	Impact of Reduction (ppb)		NMB (%)	NME (%)	r^2
			BFD	RFM			
10%	E_{AER}; J_{PHOT}; Reactions (U7)	10%	0.1232	0.099	-10.425	-32.146	0.882
20%	E_{AER}; J_{PHOT}; Reactions (U7)	20%	0.0980	0.813	-10.555	-32.798	0.879
30%	E_{AER}; J_{PHOT}; Reactions (U7)	30%	0.0728	0.070	-10.555	-32.798	0.877
50%	E_{AER}; J_{PHOT}; Reactions (U7)	50%	0.1034	0.112	-12.721	-50.647	0.862
100%	E_{AER}; J_{PHOT}; Reactions (U7)	100%	0.1632	0.176	-15.223	-52.289	0.867
200%	E_{AER}; J_{PHOT}; Reactions (U7)	200%	0.2635	0.283	-15.823	-52.289	0.823
300%	E_{AER}; J_{PHOT}; Reactions (U7)	300%	0.2835	0.305	-13.752	-37.093	0.856
500%	E_{AER}; J_{PHOT}; Reactions (U7)	500%	1.2031	1.452	-10.525	-32.146	0.850

6.2.2.3 Perturbations in both NO_x and Aerosol Emissions

Eq. 6.7 was developed for computing the concentrations when multiple parameters could be perturbed. This equation is used to compute RFM values and compare with BFD values. Table 6.9 presents the results of this analysis. The BFD values for simultaneous NO_x and aerosol perturbations of 10%, 25%, and 50% were -0.856 ppb, -2.526 ppb, and -5.798 ppb respectively. The r^2 values for 10%, 25%, and 50% combined perturbations were 0.7103, 0.7547, and 0.4425 respectively. RFM in a combined mode appears to perform better at 10% and 25% perturbations; the primary reason for this is that in the combined mode it accounts for the cross sensitivities on both NO_x and aerosol emissions and thus predicts more accurate values. However, at 50% the model does not perform well, this could be because of the nonlinear impact on O_3 due to aerosol increase (Figure 6.2) which could not be accounted for in the RFM.

Table 6.9 Performance of the RFM in Predicting the Impacts of Perturbations in both NO_x and Aerosol Emissions

Change in Emissions	Uncertain Input Parameters	Change in input parameters	Impact of Reduction (ppb)		NMB (%)	NME (%)	r^2	Slope	Intercept
			BFD	RFM					
-10% NO_x and +10% aerosols	E_{NOx}; E_{AER}	10	-0.857	-0.690	-23.2901	-58.2194	0.7103	0.8758	-0.1532
	E_{NOx}; E_{AER}; E_{VOC}	10	-0.857	-0.357	-100	-115.157	0.7356	0	0
	E_{NOx}; E_{AER}; E_{VOC}; J_{PHOT}	10	-0.857	-0.709	-23.717	-55.5755	0.7504	0.8716	-0.1564
	E_{NOx}; E_{AER}; E_{VOC}; J_{PHOT}; REACTION RATES	10	-0.857	-0.722	-22.8244	-53.9948	0.7823	0.903	-0.1415
-25% NO_x and +25% aerosols	E_{NOx}; E_{AER}	25	-2.526	-1.710	-24.149	-72.7219	0.7547	0.7782	-0.5016
	E_{NOx}; E_{AER}; E_{VOC}	25	-2.526	-1.922	-100	-117.571	0.7625	0	0
	E_{NOx}; E_{AER}; E_{VOC}; J_{PHOT}	25	-2.526	-1.847	-25.3053	-64.4065	0.6855	0.8261	-0.4687
	E_{NOx}; E_{AER}; E_{VOC}; J_{PHOT}; REACTION RATES	25	-2.526	-1.934	-22.8878	-60.057	0.6629	0.9054	-0.3695
-50% NO_x and +50% aerosols	E_{NOx}; E_{AER}	50	-5.798	-2.791	-32.8466	-111.359	0.4425	0.2581	-2.1746
	E_{NOx}; E_{AER}; E_{VOC}	50	-5.798	-2.890	-100	-123.247	0.3592	0	0
	E_{NOx}; E_{AER}; E_{VOC}; J_{PHOT}	50	-5.798	-3.449	-35.4294	-88.7227	0.2729	0.6784	-1.4782
	E_{NOx}; E_{AER}; E_{VOC}; J_{PHOT}; REACTION RATES	50	-5.798	-3.449	-30.0293	-78.2626	0.3948	0.8532	-1.0601

6.3 Probabilistic Framework and Emissions Perturbations

In the previous sections, parametric uncertainties were analyzed in detail followed by development and evaluation of RFM. The developed RFM was in good agreement with BFD of CMAQ runs. The results of CMAQ are known to be uncertain due to structural and parametric uncertainties, as discussed in earlier sections. Efforts have been done to characterize the probabilistic response of air pollutants to perturbations by employing numerous Monte Carlo CMAQ simulations. However, large computing requirements make it impractical to perform numerous simulations. Hence, RFM equations can be used for any perturbations of φ_k, where k is an uncertain parameter, in contrast to the direct Monte Carlo simulations of CMAQ.

6.3.1 Probabilistic Framework

This section discusses the results of the Monte Carlo simulations that were performed for RFM (Eq. 6.7), treating each of the input parameter as an independent log-normally distributed variable with 1-sigma uncertainty. Uncertain input parameters selected for Monte Carlo analysis is based on IF (abs (IF) > 0.01), as discussed in Section 6.1.1 and presented in Table 6.10. It should be noted that all photolysis frequencies are combined and used as one uncertain parameter. The probabilistic framework of this approach is illustrated in Figure 6.3. For each targeted emission perturbation (NO_x reduction or aerosol increase), one million Monte Carlo sampling of the uncertainty parameter (φ_k) were made to generate a probabilistic distribution of the change in concentrations, as a result of perturbations.

Table 6.10 Uncertain Input Parameters for Monte Carlo Analysis

Parameter	Uncertainty	Factor	Sigma	Cross Sensitivity (ppb|)	
				NO_x	Aerosol
Emission Rates					
NO_x Emissions	±40 (1α) [a]	1.40	0.336	-19.182	
VOC Emissions	±50 (1α) [a]	1.50	0.405	3.332	
Aerosol Emissions	±40 (1α) [a]	1.40	0.336		0.00472
Reaction Rates					
Combined Phot	±50 (2α) [b]	1.41	0.347	15.696	0.00981
<R11>O1D+H2O=2.000*OH	±10 (1α) [*]	1.10	0.095	9.792	0.00495
<R28>NO2+OH=HNO3	±30 (2α) [c]	1.14	0.131	-7.243	0.00103
<R65>OH+CO=HO2	±10 (1α) [*]	1.10	0.095	1.031	0.002340
<R66>OH+CH4=MEO2	±20 (1α) [a]	1.20	0.182	3.544	0.00158
<R3>O3+NO=NO2	±10 (1α) a	1.10	0.095	-2.076	-0.00186
<R30>HO2+NO=OH+NO2	±10 (1α) a	1.10	0.095	1.125	0.001509
<R43>OH+HO2=	±10 (1α) [*]	1.10	0.095	-0.432	-0.000840
<R73>FORM+OH=HO2+CO	±10 (1α) [b]	1.10	0.095	0.519	0.000189
<R34>HO2+HO2=H2O2	±10 (1α) [a]	1.10	0.095	-0.461	-0.000296
<R13>O3+HO2=OH	±10 (1α) [*]	1.10	0.095	0.886	-0.000016
<R112>PAR+OH=0.870*XO2+0.130*XO2N+0.110*HO2+0.060*ALD2-0.110*PAR+0.760*ROR+0.050*ALDX	±10 (1α) [a]	1.10	0.095	0.519	0.0001971
<R7>NO2+O3=NO3	±10 (1α) [*]	1.10	0.095	-0.787	-0.000274
<R22>NO+NO+O2=2.000*NO2	±10 (1α) [*]	1.10	0.095	0.664	0.000132
<R67>MEO2+NO=FORM+HO2+NO2	±10 (1α) [*]	1.10	0.095	0.051	0.000135

[a] Deguillaume et al., 2007; [b] Hanna et al., 2001; [c] Sander S P, 2006 ; * Adopted in this study.

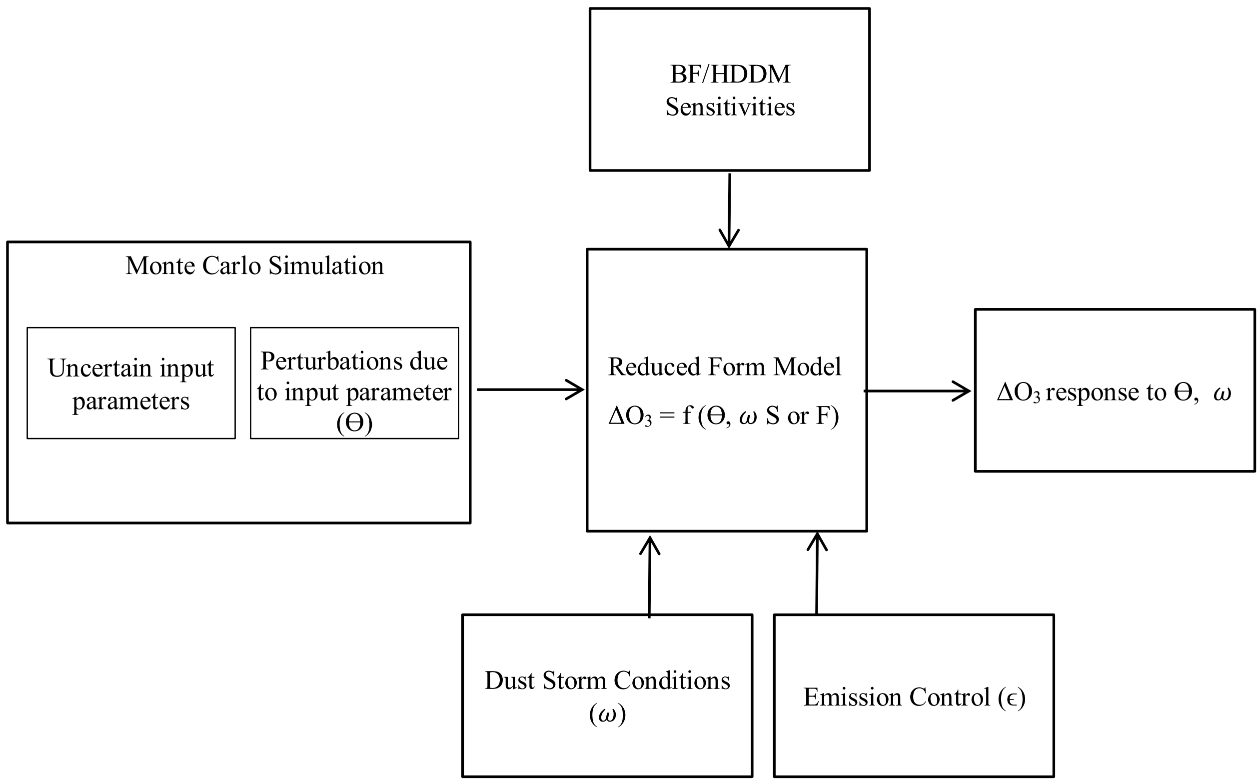

Figure 6.3 Probabilistic Framework for Characterizing O_3 Response to Emissions Perturbations under Parametric Uncertainties

The primary aim of this was to estimate the probability that a perturbation would actually produce an O_3 increase or decrease in view of the parametric uncertainty. Analogous to the approach by Digar (Digar, et al., 2011), two analysis scenarios were considered: fixed (T_{fixed}) and flexible (T_{flex}) target. T_{fixed} assumes that the reduction or increment of emissions is known and only the impact on O_3 concentrations (ΔC) of the perturbation is uncertain due to input uncertainty. The likelihood of meeting the fixed target (L_{fixed}) is the probability that ΔC is greater than or equal to T_{fixed}, given by Eq. 6.9.

$$L_{fixed} = P\ (\Delta C \geq T_{fixed}) \tag{6. 9}$$

On the other hand, T_{flex} is the case where the required impact ΔC, cannot be predicted with a certainty. The likelihood of meeting this T_{flex} is a function that increases with impact and a Gaussian function can be used as presented in Eq. 6.10 and the likelihood (L_{flex}) can be calculated using the probability density as shown in Eq. 6.11.

$$T(\Delta C) = \int_{-\infty}^{\Delta C} \frac{1}{\sigma\sqrt{2\pi}} e^{\frac{-(x-\mu)^2}{2\sigma^2}}\, dx \tag{6. 10}$$

$$L_{flex} = \int_{-\infty}^{+\infty} P(\Delta C)\, T(\Delta C)\, d\Delta C \tag{6. 11}$$

6.3.2 Likelihood of Impact on O_3 due to NO_x Reduction

NO_x emission reduction scenarios will be considered as discussed in Section 6.2 to estimate the probability of T_{fixed} and T_{flex}. Additionally, aerosol increases will also be considered as it is proved that it contributes to the increase or decrease of O_3 concentrations. This probabilistic framework will be used to estimate the probability of increase/decrease in O_3 concentrations with aerosol emissions perturbations.

Three parameters (the mean, 5th percentile, and 95th percentile) for RFM under various NO_x emission reduction scenarios of the one million Monte Carlo samplings of the input, φ_k, are presented in Table 6.11. The table also presents the results considering different types of uncertainties. Deterministic values were computed based on the base RFM runs (φ_k=0). The last column in the table shows the likelihood of achieving a T_{fixed}, hypothetically taken as 5 ppb. It can also be noted that the probabilistic mean values correlate very well with the deterministic values.

Figure 6.4 illustrates the probability density and cumulative density plots of 10% NO_x reductions under various parametric uncertainties. Across the uncertainties, it is observed that the likelihood of achieving a T_{fixed} increases from U1 to U3, however, the likelihood decreases for U4 indicating the higher uncertainty associated with chemical reactions.

For a 25% NO_x reduction, the likelihood of reaching a 5 ppb O_3 reduction target is 58%, 59%, 65%, and 54% under the uncertainties U1, U2, U3, and U4 respectively. For 50% NO_x reduction, the likelihood of reaching a 5 ppb reduction is over 99%. Therefore, to get a definite 5 ppb reduction in O_3, NO_x must be reduced by at least 50%.

Figure 6.5 and Figure 6.6 show the probability distribution plots for 25% and 50% NO_x reduction respectively considering all uncertainties. The probabilistic values are closer to the deterministic values when the NO_x reduction is less, as indicated by the cumulative distribution plots shown in Figure 6.7.

Table 6.11 Likelihood to Achieve a Fixed Target under NO_x Reduction Scenarios Considering Parametric Uncertainties

Change in NO_x Emissions	Uncertain Input Parameters	Deterministic O_3 impact*	O_3 impact under parametric uncertainty			Likelihood to achieve $T_{fixed} \geq 5$ ppb
			mean	5th pctl	95th pctl	
-10%	E_{NOx} (U1)	2.50	1.866	1.122	2.988	0.11%
10%	E_{NOx}; E_{VOC} (U2)	2.50	1.854	1.128	3.004	0.12%
-10%	E_{NOx}; E_{VOC}; J_{PHOT} (U3)	2.50	1.979	1.193	3.162	0.18%
-10%	E_{NOx}; E_{VOC}; J_{PHOT}; Reactions (U4)	2.50	1.773	1.060	2.853	0.08%
-25%	E_{NOx} (U1)	6.45	5.847	3.259	9.961	58.94%
-25%	E_{NOx}; E_{VOC} (U2)	6.45	5.872	3.276	9.994	59.48%
-25%	E_{NOx}; E_{VOC}; J_{PHOT} (U3)	6.45	6.132	3.439	10.393	64.80%
-25%	E_{NOx}; E_{VOC}; J_{PHOT}; Reactions (U4)	6.45	5.617	3.107	9.622	54.01%
-50%	E_{NOx} (U1)	14.41	15.694	8.050	28.206	99.97%
-50%	E_{NOx}; E_{VOC} (U2)	14.41	15.690	8.083	28.280	99.97%
-50%	E_{NOx}; E_{VOC}; J_{PHOT} (U3)	14.41	16.208	8.411	29.062	99.98%
-50%	E_{NOx}; E_{VOC}; J_{PHOT}; Reactions (U4)	14.41	15.179	7.746	27.519	99.94%

* BF differencing of CMAQ runs at selected receptors (O_3 concentration >=50 ppb)

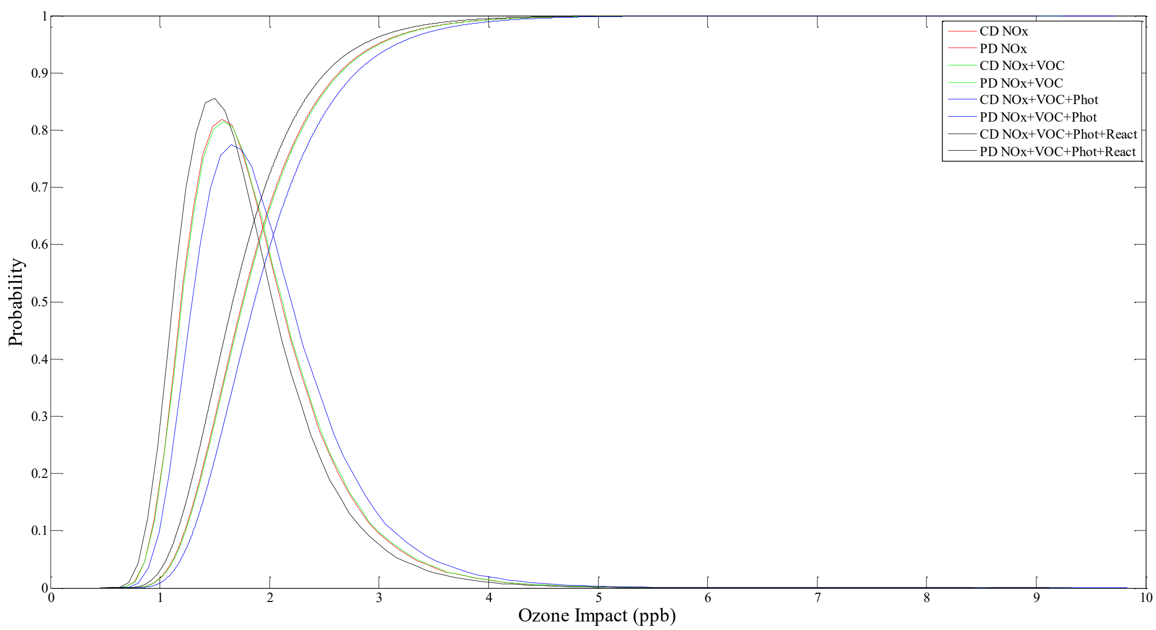

Figure 6.4 Probability Density and Cumulative Distribution Plot of O_3 Impact for Various Uncertainties Under 10% NO_x Reduction

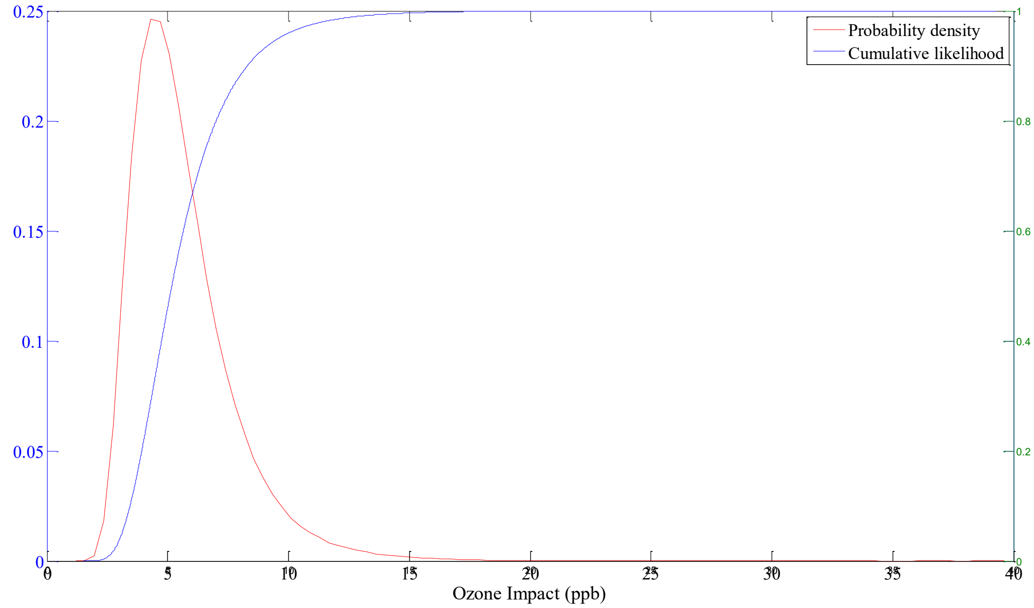

Figure 6.5 Probability Distribution of O_3 Impact Under 25% NO_x Reduction Considering All Parametric Uncertainties.

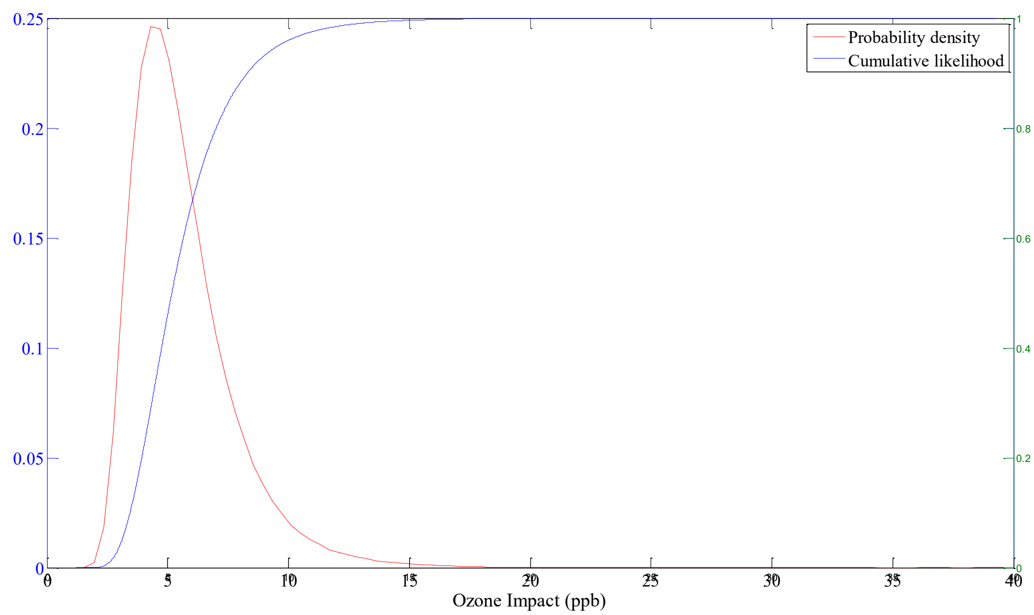

Figure 6.6 Probability Distribution of O_3 Impact Under 50% NO_x Reduction Considering All Parametric Uncertainties

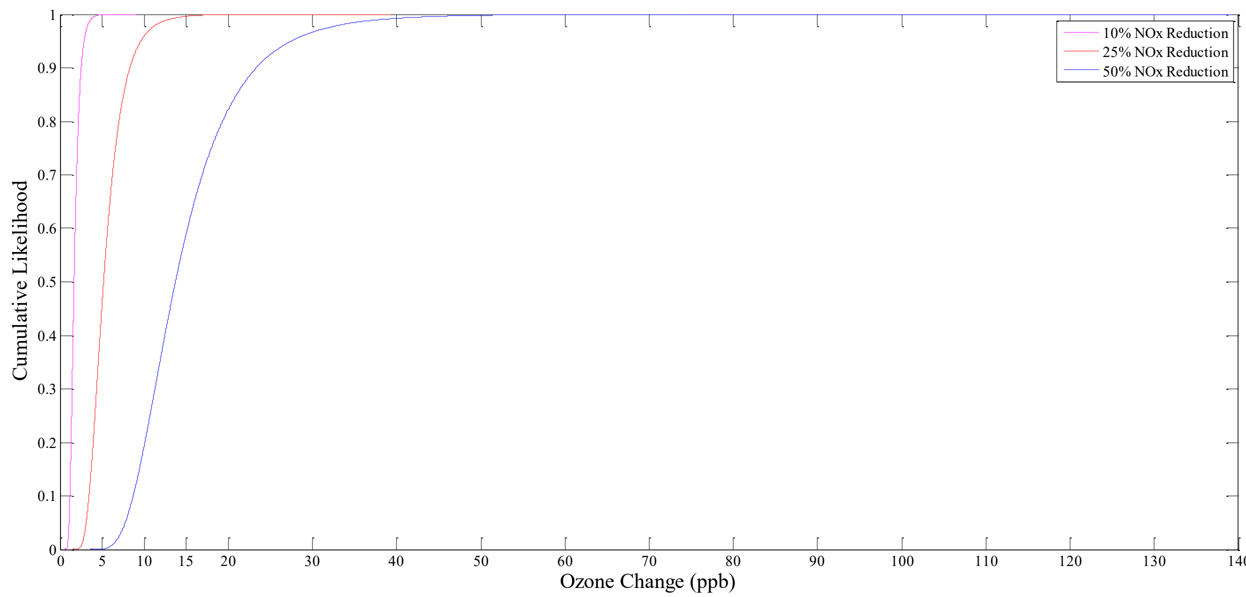

Figure 6.7 Cumulative Distribution Plots of O_3 Impact Considering All Parametric Uncertainties under Various NO_x Reduction Scenarios

6.3.3 Likelihood of Impact on O_3 due to Increase of Aerosol Emissions

For the aerosol increment scenarios, the analysis was done by including all the uncertainties, U7, for simplicity. Table 6.12 presents the results of the deterministic and probabilistic runs of RFM by increasing the aerosol emissions from 10% to 500%. Similar to NO_x results, there is a good correlation between deterministic runs and probabilistic runs. The last column in the table shows the impact of increasing aerosols emissions on O_3 concentrations with a likelihood of 50%. The cumulative density plots for various aerosol increases are shown in Figure 6.8. From Table 6.12 and Figure 6.8, it can be inferred that there is a 50% possibility that the O_3 increases by 2.5 ppb, 4.5 ppb, 7.0 ppb, and 11.0 ppb for 100%, 200%, 300%, and 500% increase in aerosols in the atmosphere respectively.

Table 6.12 Likelihood to Achieve a Fixed Target under Aerosol-Emission Increase Scenarios Considering Parametric Uncertainties

Change in aerosol emissions	Uncertain Input Parameters	Deterministic O_3 impact*	O_3 impact under parametric uncertainty			Increase in O_3 Conc.**
			mean	5th pctl	95th pctl	
10%	E_{AER}; J_{PHOT}; Reactions (U7)	0.1232	0.235	0.168	0.329	0.23
20%	E_{AER}; J_{PHOT}; Reactions (U7)	0.0980	0.470	0.336	0.657	0.45
30%	E_{AER}; J_{PHOT}; Reactions (U7)	0.0728	0.705	0.550	0.988	0.65
50%	E_{AER}; J_{PHOT}; Reactions (U7)	0.1034	1.175	0.8418	1.648	1.20
100%	E_{AER}; J_{PHOT}; Reactions (U7)	0.1632	2.350	1.682	3.293	2.50
200%	E_{AER}; J_{PHOT}; Reactions (U7)	0.2635	4.669	3.367	6.590	4.50
300%	E_{AER}; J_{PHOT}; Reactions (U7)	0.2835	7.022	5.049	9.890	7.00
500%	E_{AER}; J_{PHOT}; Reactions (U7)	1.2031	11.752	8.4177	16.483	11.00

* BFD of CMAQ runs at selected receptors ** Values at 50% likelihood

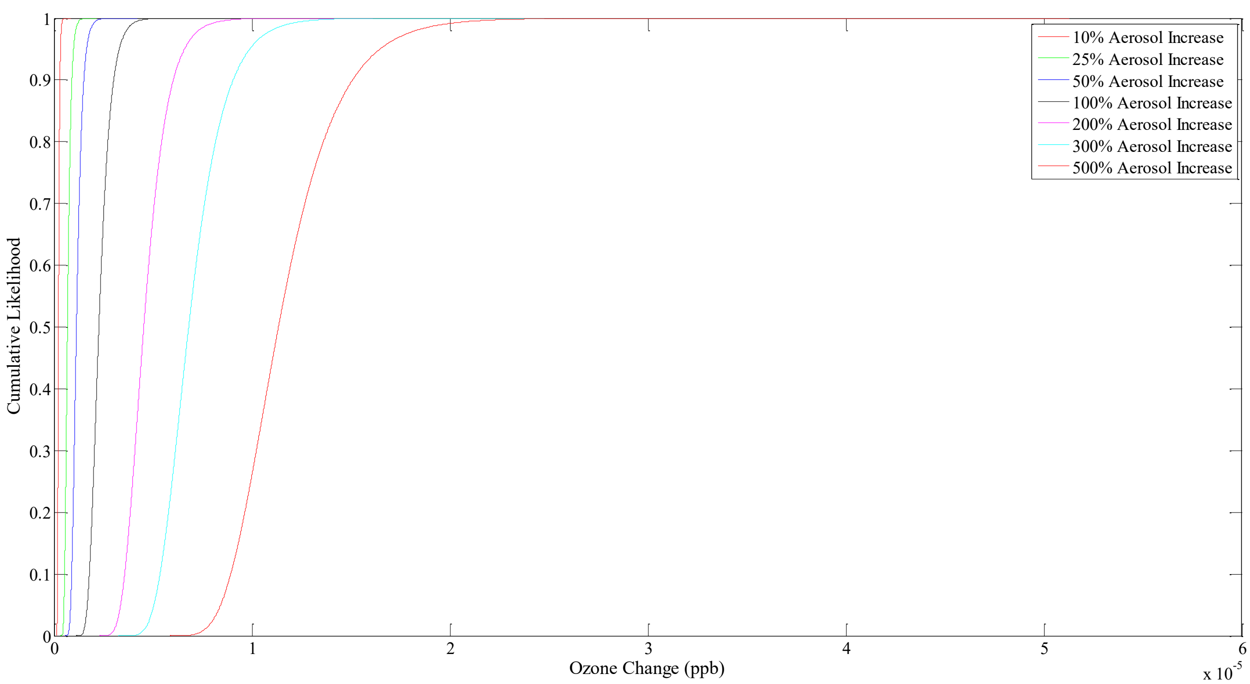

Figure 6.8 Cumulative Distribution Plots of O_3 Impact Considering all Parametric Uncertainties under Various Aerosol Increase Scenarios

6.4 Summary

Development and validation of an RFM is the key theme of this chapter. The purpose of developing an RFM in the current context, is to establish a relationship between O_3 formation and its precursors (this relationship is well known to be nonlinear and complex) and minimizing the need to run the computing intensive CMAQ. RFM depends on uncertain parameters, therefore identifying the uncertain parameters to the formation of O_3 and computing the corresponding sensitivity coefficients is pivotal. In addition to developing an RFM for the first time in this region, the role of mineral dust has also been considered. Heterogonous reactions of the minerals in the dust particles or aerosols influence the formation of O_3, but this factor has not been incorporated in CMAQ.

The first order, second order, and cross sensitivity coefficients were defined and computed by running CMAQ simulations. Cross sensitivity coefficients were also calculated for both NO_x and aerosol emissions. The newly identified parameter, called impact factor, has been used to rate the significance of the uncertain parameter. The cross sensitivities for the photolysis frequencies were computed for each of the reactions. The first order, second order, and cross sensitivities for the combined photolysis were observed to be high as solar radiation is generally high in this region. Disassociations of O_3 into O1D was observed to be predominant when compared to O, indicating the presence of solar radiations of 315 nm and above. O1D is known to be more reactive than O, hence it triggers several reactions including ones with H_2O, NO_2, NO, and OH forming intermediate radicals known to promote O_3 formation. Analysis of sensitivity coefficients for various chemical reactions revealed that the coefficients were more sensitive with NO_x reactions than VOCs, indicating the region is NO_x sensitive. These coefficients were found to be higher than other studies.

During the analysis of cross sensitivity coefficients with aerosols, it was observed that the species in the ANO3J, fine mode nitrate, is the only species that was sensitive with the parameters. Earlier, it was proved that during dust storms this species increases significantly. The aerosol emissions seem to be highly sensitive with the compounds HNO_3, NO_3, and NO. This presents an evidence of heterogeneous reactions occurring between these compounds and the species in aerosols.

An RFM was developed incorporating the uncertainties in the model. The RFM equations were created to estimate the change in O_3 concentration for any amount of NO_x emission perturbations and or aerosol emission perturbations. The RFM was evaluated against NO_x reduction, aerosol emissions (dust storm condition), and a combined NO_x reduction and aerosols increments scenarios. The RFM correlated well with the BFD for all scenarios. It was observed that the performance was better at lower reduction levels of NO_x and a higher number of uncertainties. For aerosols increase scenarios, the impact on O_3 did not follow a linear pattern. O_3 concentration decreased initially, up to aerosol increase of about 50%, and then the concentration started to increase. The primary reason for this nonlinear increase in O_3 concentration is the heterogeneous reactions of dust with HNO_3, NO_3, and NO that suppress the NO_x cycle resulting in less production of O_3. However, this phenomenon only occurs at lower levels of aerosol concentrations. At higher aerosol concentrations, ANO3J promotes the NO_x cycle rather than suppressing it. This explains the disparity in reporting the relationship of aerosols and O_3 formation in other studies.

RFM was also analyzed against the probabilistic framework by performing the Monte Carlo sampling of uncertain input parameters. Higher uncertainties were observed with respect to chemical reactions parameters. There is a 50% likelihood that a 5 ppb O_3 formation can be reduced by reducing 25% of NO_x emissions. It was also observed that there is 50% likelihood that the formation of O_3 could increase as much as 10 ppb with an increase of 500% aerosols in the atmosphere; these high aerosol concentrations are not uncommon during dust storms in this region.

CONCLUSIONS AND RECOMMENDATIONS

The overarching goal of this research was twofold. Firstly, it was to investigate the chemical mechanisms in the formation of O_3 under arid conditions (particularly the role of dust). Secondly, it was to develop an RFM and characterize uncertainties to enable decision makers to devise effective mitigation strategies to control O_3 precursors. The study area was the Riyadh region in Saudi Arabia due to its deteriorating air quality and frequent dust storm events. CMAQ (an advance photochemical model) was configured for the study area. Necessary data was collected and analyzed for the purpose of developing and validating the objectives of this research. Several runs of CMAQ were made to generate uncertainty coefficients to validate the RFM. The key conclusions from this research are presented below.

7.1 Conclusions

7.1.1 Chemical Mechanisms and Kinetic Terms in Arid Regions

The investigation of the effect of chemical mechanisms in CMAQ on the production of various secondary pollutants (oxidants, nitrogen species, and O_3) revealed that RACM2 is the most suitable for arid regions. RACM2 produced higher OH concentrations compared to others, but the overall production of OH was less due to the shortage of moisture (OH is primarily formed by the reaction: $O1D + H_2O = 2OH$). The rate constant in CMAQ for this reaction is lower than the others which is suitable for arid regions. Higher temperatures of arid regions might trigger reactions of O_3 with alkenes and other organic compounds forming H_2O_2 radicals; these reactions exist only in RACM2. SAPRC07 produced the highest concentration of surface O_3 followed by RACM2 and CB05 representing the rates of the O_3 formation reaction ($O3P + O_2 + M = O_3$) in the respective mechanisms. The RACM2 predicted values of O_3 closely correlated with the observed values indicating that the reaction rate of O_3 formation in this mechanism is also suitable for the region. This finding will assist regulatory agencies in designing effective O_3 control strategies. Moreover, it will also serve as a benchmark for any future implementation of PAQM in this region as well as similar regions.

7.1.2 Key Factors Influencing the O_3 Precursor Responsiveness

This research characterized the parametric uncertainty influencing the prediction of O_3 to both NO_x and aerosols emissions perturbations. The simulations performed in the study-domain revealed that the model input parameters: NO_x, biogenic and aerosol emission rates, photolysis frequencies, and the reaction rate constants were key factors in O_3 formation. Among the photolysis reactions, disassociation of O_3 into O1D was observed to be more sensitive when compared to disassociation of O_3 into O. This can be explained by the high frequency solar radiations of 315 nm and above. Analysis of sensitivity coefficients for the various chemical reactions revealed that the main reactions that were sensitive to NO_x and aerosol emissions were $O1D + H_2O = 2OH$, $O1D + M = O + M$, $OH + CH_4 = MEO_2$, and $OH + HNO_3 = NO_3$. The reactions were more sensitive with NO_x emissions than VOCs, indicating that the region is NO_x limited. This finding will better understand the formation of O_3 in the region and subsequently help in its control.

7.1.3 Computationally Efficient RFM

Controlling O_3 and other secondary pollutants requires running PAQM for several scenarios to characterize model uncertainties, which is computationally challenging. To overcome the computational burden, this thesis contributes an efficient RFM that characterizes the impact of uncertainties in model input parameters on O_3 response to not only precursor emissions (NO_x and VOCs) but also to the dust emissions. The RFM was validated for accuracy against the underlying PAQM. It correlated mostly well with the BFD for all scenarios. The performance was better when more number of uncertainties were included and when the reduction levels of NO_x were lower. In most of the test cases reasonable regression coefficients (>85%) and low bias and error (<15%) were observed. This shows a high confidence in the developed RFM in reproducing similar results to that of the PAQM run. This RFM can be used by regulatory authorities to evaluate various mitigation scenarios without the need for immense computational burden.

7.1.4 Probabilistic Framework

The developed RFM allowed performing numerous Monte Carlo simulations of uncertain input parameters with greater efficiency. Higher uncertainties were observed with respect to chemical reactions. In order to reduce 5 ppb of O_3, a reduction of 50% NO_x is necessary. The newly incorporated aerosol parameter in the RFM revealed that if aerosols increased fivefold (due to dust storm conditions), the O_3 concentration in the atmosphere is likely to increase by 10 ppb. This finding will help relevant authorities to take necessary measures in an incoming dust storm.

7.2 Originality and Contributions

Employing the state-of-the-art PAQM in arid regions, this research focussed on understanding the formation of secondary pollutants, particularly O_3. The summary of the author's contribution and originality of this study are outlined as follows:

- Identified key kinetic terms in PAQM in the formation of secondary pollutants for arid regions.
- Developed and validated a computationally efficient RFM to capture the responsiveness of pollutants to emissions reduction in the underlying CMAQ runs.
- Identified and computed sensitivity coefficients for parameters uncertain to the formation of O_3 in arid regions.
- Used the developed RFM to study the impact of mineral dust on O_3 formation.
- Developed a probabilistic model to study the impact on O_3 concentrations under various emissions reduction strategies as well as under dust storm conditions.

This research resulted in several publications in conferences and journals as a contribution to the scientific platform. The following is the list of publications including papers accepted and under review:

- Shareef, M. M., Husain, T., Alharbi, B (2016). Identifying appropriate chemical mechanisms for photochemical air quality modelling in arid regions. A&WMA's 109th Annual Conference & Exhibition, June 20-23, New Orleans, USA

- Shareef, M. M., Husain, T., Alharbi, B. (2016). Optimization of Air Quality Monitoring Network Using GIS Based Interpolation Techniques. Journal of Environmental Protection, 7(06), 895.
- Alharbi, B., Shareef, M. M., Husain, T. (2015). Study of chemical characteristics of particulate matter concentrations in Riyadh, Saudi Arabia. Atmospheric Pollution Research, 6(1), 88-98.
- Shareef, M. M., Alharbi, B., Husain, T., (2014). Study of Spatial and Temporal Variation and Development of Appropriate Indicators of Ionic Components in PM in Riyadh, Saudi Arabia, A&WMA's 107th Annual Conference & Exhibition, June 24-27, Long Beach, USA. (Conference)
- Shareef, M. M., and Husain, T., (2014). Air quality impacts due to oil spills. The 2014 International Conference on Marine and Freshwater Environments, At St. Johns, NL, Canada.
- Shareef, M. M., Husain, T., Alharbi, B (2017). Analysis of relationship between O_3, NO and NO_2 in Riyadh, Saudi Arabia (Accepted).
- Alharbi, B., Shareef, M. M., Bian, Q., Husain, T., Kreidenweis, S., Collett, J., Pasha, M (2017). Summertime organic and elemental carbon in $PM_{2.5}$ in Riyadh, Saudi Arabia (Under review).
- Shareef, M. M., Husain, T., Alharbi, B., (2017). A comparison of ozone formation in central Saudi Arabia under different gas-phase chemical kinetic mechanism. (Under review).

7.3 Recommendations

The research undertaken in this thesis was to advance the scientific understanding of the implementation of PAQM in arid regions. This leads to several potential avenues for further research as suggested below.

7.3.1 Enhancements to RFM

This thesis made considerable effort to develop an RFM that would incorporate various uncertainties, particularly dust emissions. A number of uncertainty coefficients were computed; however, further research is needed to refine these coefficients. This could be accomplished by running additional PAQM simulations to enhance the accuracy of the coefficients.

The type of RFM contributed by this research is continuum based; meaning emission perturbations are uniform in the domain. However, for cases in which the targeted amount of emission reduction is known in advance, development of a discrete RFM is possible, such as in the application of certain control technologies that would result in emission reduction at a major point source.

The RFM model primarily incorporates only parametric uncertainties, so it would be highly recommended to extend this to include structural uncertainties such as using different meteorological models as well as considering uncertainties in meteorological inputs (wind speed, temperature, cloud cover etc.).

The performance of the RFM was good near the sources and in the proximity of populated areas, however, considerable deviations were observed near the domain boundaries. The reason for this deviation needs further investigating.

Probabilistic framework of the RFM model could be extended to incorporate economic aspects by including cost factor to various control measures. Similarly, the RFM could be integrated with health risk assessment (e.g. epidemiological uncertainty) to evaluate the health benefits of any control measure.

7.3.2 Observed and Emissions Data

The research used limited ground-based measurements of O_3, NO_x and other pollutants to constrain the model simulations. The model predictions could be improved by enriching it with more observed data including from higher altitudes. Enhancing the emissions input with more comprehensive data will improve the research findings. There were limited O_3 measurements during and after dust storms, so it will be useful to collect such data and compare it with simulated ones.

As summer is accompanied by high O_3 formation and dust storm conditions, all the model simulations were performed in this period. However, it would be interesting to investigate the chemical mechanisms and RFM uncertainty coefficients of various parameters in other seasons. This will reveal the difference in chemical mechanisms between summer and winter. Although this research primarily focussed on ground-based O_3 pollution and the central region of Saudi Arabia, this could be extended to other pollutants and to other similar regions.

7.3.3 Air Chamber Studies

This research investigated the chemical kinetics in the formation of secondary pollutants in arid conditions using observed data and PAQM. The key chemical reactions and corresponding reaction constants were identified. However, in order to have an accurate understanding of the chemical mechanisms, an experimental study involving air chambers is necessary. Therefore, it is recommended to setup an air chamber with arid conditions (including dust storms conditions) in order to get full insight into the chemistry of O_3 and other secondary pollutant formations particularly the heterogeneous reactions of NO_x and dust particles under such conditions. The findings could be incorporated into the CMAQ model.

REFERENCES

ACENET, 2016. ACENT [Online] Available at. https://www.ace-net.ca/ [Accessed 7 9 2016]

Al Katheeri, E., Al Jallad, F. & Al Omar, M., 2012. Assessment of Gaseous and Particulate Pollutants in the Ambient Air in Al Mirfa City, United Arab Emirates. *Journal of Environmental Protection,* Volume 3, pp. 640-647.

Alharbi, B. H., Maghrabi, A. & Tapper, N., 2013. The March 2009 dust event in Saudi Arabia: Precursor and supportive environment. *Bulletin of the American Meteorological Society,* 94(4), pp. 515-528.

Alharbi, B. h., Pasha, M. J. & Tapper, N., 2014. Assessment of Ambient Air Quality in Riyadh City, Saudi Arabia. *Current Work Environment,* 9(2), pp. 227-239.

Alharbi, B., Shareef, M. M. & Husain, T., 2015. Study of chemical characteristics of particulate matter concentrations in Riyadh, Saudi Arabia. *Atmospheric Pollution Research,* 6(1), pp. 88-98.

Alharbi, B., Shareef, M. M. & Husain, T., 2015. Study of chemical characteristics of particulate matter concentrations in Riyadh, Saudi Arabia. *Atmospheric Pollution Research,* pp. 88-98.

Al-Jeelani, H. A., 2014. Diurnal and Seasonal Variations of Surface Ozone and Its Precursors in the Atmosphere of Yanbu, Saudi Arabia. *J Environ Prot.,* Volume 5, pp. 408-422.

Appel, K. W., Roselle, S. J., Gilliam, R. C. & Pleim, J. E., 2010. Sensitivity of the community multiscale air quality (CMAQ) model v4.7 results for the eastern United States to MM5 and WRF meteorological drivers. *Geosci. Model Dev. 3,* pp. 169-188.

Arimoto, R. et al., 1996. Relationships among aerosol constituents from Asia and the North Pacific during Pem-West.. *Journal of Geophysical Research,* Volume 101, pp. 2011-2023.

Arnold, J. R. & Dennis, R. L., 2006. Testing CMAQ chemistry sensitivities in base case and emissions control runs at SEARCH and SOS99 surface sites in the southeastern US. *Atmospheric Environment,* 40(26), pp. 5027-5040.

Arunachalam, S. et al., 2011. Effect of chemistry-transport model scale and resolution on population exposure to PM2. *Atmos. Environ. 45,* p. 3294–3300.

Atkinson, R., 2000. Atmospheric chemistry of VOCs and NOx. *Atmospheric Environment,* Volume 34, p. 2063–2101.

Atkinson, R. W. et al., 2013. Long-term exposure to outdoor air pollution and incidence of cardiovascular diseases. *Epidemiology 24,* pp. 44-53.

Baker, K. R. & Kelly, J. T., 2014. Single source impacts estimated with photochemical model source sensitivity and apportionment approaches. *Atmospheric Environment 96 ,* pp. 266-274.

Baro, R. et al., 2015. Sensitivity analysis of the microphysics scheme in WRF-Chem contributions to AQMEII phase 2. *Atmospheric Environment,* Volume 115, pp. 620-629.

Bell, M. L., Dominici, F. & Samet, J. M., 2005. A metaanalysis of time-series studies of ozone and mortality with comparison to the National Morbidity, Mortality, and Air Pollution Study. *Epidemiology 16,* pp. 436-45.

Bergin, M. et al., 1999. Formal uncertainty analysis of a Lagrangian photochemical air pollution model. *Environ. Sci. Technol.,* pp. 1116-1126.

Bonasoni, P. et al., 2004. Aerosol-ozone correlations during dust transport episodes. *Atmospheric Chemistry and Physics,* 4(5), pp. 1201-1215.

Brown, K. W. et al., 2008. Characterization of Particulate Matter for Three Sites in Kuwait. *Journal of Air & Waste Management Association,* Volume 58, p. 994–1003.

Brunekreef, B. & Forsberg, B., 2005. Epidemiological evidence of effects of coarse airborne particles on health. *European Respiratory Journal,* 26(2), pp. 309-318.

Burr, M. & Zhang, Y., 2011. Source apportionment of PM2. *Atmos. Pollut. Res. 2,* pp. 300-317.

Byun, D. & Schere, K., 2006. Review of the governing equations, computational algorithms, and other components of the Models-3 Community Multiscale Air Quality (CMAQ) modeling system. *Applied Mechanics Reviews 55,* Volume 55, p. 51–77.

Carter, W., 2010. Development of the SAPRC-07 chemical mechanism. *Atmos. Environ,* Volume 44, pp. 5324-5335.

Carter, W. P. & Atkinson, R., 1996. Development and evaluation of a detailed mechanism for the atmospheric reactions of isoprene and NOx. *International Journal of Chemical Kinetics,* 28(7), pp. 497-530.

Carter, W. P. L., 1996. Condensed atmospheric photooxidation mechanisms for isoprene. *Atmos. Environ. 30,* pp. 4275-4290.

Carter, W. P. L., 1999. *"Documentation of the SAPRC-99 Chemical Mechanism for VOC Reactivity Assessment,",* s.l.: s.n.

Carter, W. P. L., 2000. *"Implementation of the SAPRC-99 Chemical Mechanism Into the Models-3 Framework," Final Report to U.S. EPA,* s.l.: s.n.

Choi, K. et al., 2014. Assessment of trans-boundary ozone contribution toward South Korea using multiple source receptor modeling techniques. *Atmospheric Environment ,* Volume 92, pp. 118-129.

Clapp, L. J. & Jenkin, M., 2001. Analysis of the relationship between ambient levels of O3, NO2 and NO as a function of NOx in UK. *Atmos. Environ.,* Volume 35, p. 6391–6405.

CMAQv5.0.2 Documentation, 2014. *CMAQv5.0.2 Readme file.* [Online] Available at: http://www.airqualitymodeling.org/cmaqwiki/index.php?title=CMAQv5.0.2_Readme_file
[Accessed 10 9 2016].

Cohan, D., Hakami, A., Hu, Y. & Russell, A., 2005. Nonlinear response of ozone to emissions: Source apportionment and sensitivity analysis. *Environ. Sci. Technol. 39,* p. 6739–6748.

Cohan, D., Koo, B. & Yarwood, G., 2010. Influence of uncertain reaction rates on ozone sensitivity to emissions. *Atmos. Environ. 44,* p. 3101–3109.

Cohan, D. S. & and Napelenok, S. L., 2011. Air quality response modeling for decision support. *Atmosphere, 2,* pp. 407-425.

Cohan, D. S., Tian, D., Hu, Y. T. & Russell, A., 2006. Control strategy optimization for attainment and exposure mitigation: Case study for ozone in Macon, Georgia. *Georgia. Environ. Manag. 38,* p. 451–462.

Collins, W. J., Stevenson, D. S., E, J. C. & Derwent, R. G., 1997. Tropospheric ozone in a global-scale three-dimensional Lagrangian model and its response to NOx emission controls. *Journal of Atmospheric Chemistry, 3,* pp. 223-274.

Community Modeling and Analysis System (CMAS), 2016. [Online] Available at: https://www.cmascenter.org/cmaq/
[Accessed 7 9 2016].

Contini, D. et al., 2010. Characterisation and source apportionment of PM10 in an urban background site in Lecce. *Atmospheric Research,* Volume 95, p. 40–54.

Debaje, S. B. & Kakade, A. D., 2006. Weekend Ozone Effect over Rural and Urban Site in India. *Aerosol Air Qual. Res.,* 6(3), pp. 322-333.

Deguillaume, L., Beekmann, M. & Menut, L., 2007. ayesian Monte Carlo analysis applied to regional-scale inverse emission modeling for reactive trace gases. *Journal of Geophysical Research: Atmospheres,* 112(D2).

Dennis, R. et al., 2010. A framework for evaluating regional-scale numerical photochemical modeling systems. *Environ. Fluid Mech. 10,* p. 471–489.

DeReus, M. et al., 2000. Airborne observations of dust aerosol over the North Atlantic Ocean during ACE 2- Indications for heterogeneous ozone destruction. *Journal of Geophysical Research,* 105(D12), pp. 15263-15275.

Derwent, R. G. & Davies, T. J., 1994. Modelling the impact of NOx or hydrocarbon control on photochemical ozone in Europe, Atmospheric Environment, 28(12. *Atmospheric Environment, 28(12),* pp. 2039-2052.

Digar, A. & Cohan, D. S., 2010. Efficient characterization of pollutant-emission response under parametric uncertainty. *Environ. Sci. Technol. 44,* pp. 6724-6730.

Digar, A. et al., 2011. Likelihood of achieving air quality target under model uncertainties. *Environ. Sci. Technol, 45,* pp. 189-196.

Dockery, D. W., 2001. Epidemiological evidence of cardiovascular effects of particulate air pollution. *Environmental Health Perspectives 109,* pp. 483-486.

Dunker, A., 1984. The decoupled direct method for calculating sensitivity coefficients in chemical kinetics. *J. Chem. Phys. 81,* p. 2385–2393.

Dunker, A. M., Koo, B. & Yarwood, G., 2014. Sensitivity of atmospheric models to rate terms within complex chemical mechanisms. *Atmospheric Environment,* Volume 98, pp. 224-230.

Dunker, A., Yarwood, G., Ortmann, J. & Wilson, G., 2002. The decoupled direct method for sensitivity analysis in a three-dimensional air quality model—Implementation, accuracy, and efficiency. *Environ. Sci. Technol. 36,* p. 2965–2976.

DW, 2015. *Pollution, Top 10 worst cities for smog.* [Online] Available at: http://www.dw.de/top-10-worst-cities-forsmog/g-17469135

Elani, U. A., 2007. Distribution of ultraviolet solar radiation at Riyadh regions, Saudi Arabia. *Environ. Mon. Assess.,* Volume 124, pp. 235-241.

Elbern, H., Schmidt, H. & Ebel, A., 1997. Variational data assimilation for tropospheric chemistry modeling. *J. Geophys. Res. Atmos,* Volume 102, p. 15967–15985.

El-Harbawi, M., 2013. Air quality modelling, simulation, and computational methods: a review. *Environ. Rev,* Volume 21, pp. 149-179.

EMEP, 2016. *Convention on long-range transboundary air pollution.* [Online] Available at: http://www.ceip.at/
[Accessed 8 9 2016].

Fairlie, T. D. et al., 2010. Impact of mineral dust on nitrate, sulfate, and ozone in transpacific Asian pollution plumes. *Atmospheric Chemistry and Physics,* 10(8), pp. 3999-4012.

Faraji, M., Kimura, Y., McDonald-Buller, E. & and Allen, D., 2008. Comparison of the Carbon Bond and SAPRC photochemical mechanisms under conditions relevant to southeast Texas. *Atmos. Environ.,* Volume 42, p. 5821–5836.

Feng, Z. & Kobayashi, a. K., 2009. Assessing the impacts of current and future concentrations of surface ozone on crop yield with meta-analysis. *Atmospheric Environment,* 43(8), pp. 1510-1519.

Foley, K. M. et al., 2015. Dynamic evaluation of CMAQ part I: Separating the effects of changing emissions and changing meteorology on ozone levels between 2002 and 2005 in the eastern US. *Atmospheric Environment,* Volume 103, pp. 247-255.

Foley, K. M. et al., 2014. Two reduced form air quality modeling techniques for rapidly calculating pollutant mitigation potential across many sources, locations and precursor emission types. *Atmospheric Environmen,* Volume 98, pp. 283-289.

Furuta, N. et al., 2005. Concentrations, enrichment and predominant sources of Sb and other trace elements in size classified airborne particulate matter collected in Tokyo from 1995 to 2004. *Journal of Environmental Monitoring,* Volume 7, pp. 1155-1161.

Gao, D., Stockwell, W. & Milford, J., 1996. Global uncertainty analysis of a regional-scale gas-phase chemical mechanism. *Global uncertainty analysis of a regional-scale gas-phase chemical mechanism,* Volume 101, p. 9107–9119.

General Authority of Statistics, Kingdom of Saudi Arabia, 2012. *Statistical year book for 2012.* [Online]
Available at: http://www.cdsi.gov.sa/en/1157

Geng, F. et al., 2008. Characterizations of ozone, NOx, and VOCs measured in Shanghai, China. *Atmos. Environ.,* Volume 42, pp. 6873-6883.

Gery, M. W., Whitten, G. Z., Killus, J. P. & and Dodge, M. C., 1989. A Photochemical Kinetics Mechanism for Urban and Regional Scale Computer Modeling. *J. Geophys. Res,* Volume 94, pp. 12,925–12,956.

Givehchi, R., Arhami, M. & Tajrishy, M., 2013. Contribution of the Middle Eastern dust source areas to PM10 levels in urban receptors: Case study of Tehran, Iran. *Atmospheric Environment,* Volume 75, pp. 287-295.

Godowitch, J. M., Gilliland, A. B., Draxler, R. R. & Rao, S., 2008. Modeling assessment of point source NOx emission reductions on ozone air quality in the eastern United States. *Atmospheric Environmen,* Volume 42, pp. 87-100.

Goliff, W. S., Stockwell, W. R. & and Lawson, C. V., 2013. The Regional Atmospheric Chemistry Mechanism, Version 2. *Atmos. Environ,* Volume 68, p. 174–185.

Grantz, D. A., Garner, J. H. & Johnson, D. W., 2003. Ecological effects of particulate matter. *Environment International,* 29(2), pp. 213-239.

Grivas, G., Cheristanidis, S. & Chaloulakou, A., 2012. Elemental and organic carbon in the urban environment of Athens. Seasonal and diurnal variations and estimates of secondary organic carbon.. *Science of the Total Environment,* Issue 414, pp. 535-545.

Gross, A. & Stockwell, W., 2003. Comparison of the EMEP, RADM2 and RACM mechanisms. *Journal of Atmospheric Chemistry,* Volume 44, p. 151–170.

Guenther, A. et al., 2006. Estimates of Global Terrestrial Isoprene Emissions Using MEGAN (Model of Emissions of Gases and Aerosols from Nature). *Atmos. Chem. Phys.,* Volume 6, pp. 3181-3210.

Hakami, A. et al., 2007. The adjoint of CMAQ. *Environ. Sci. Technol,* Volume 41, p. 7807–7817.

Hakami, A., Odman, M. & Russell, A., 2003. High-order, direct sensitivity analysis of multidimensional air quality models. *Environ. Sci. Technol,* Volume 37, p. 2442–2452.

Hakami, A., Odman, M. & Russell, A., 2004. Nonlinearity in atmospheric response: A direct sensitivity analysis approach. *J. Geophys. Res. Atmos.,* 109(D15).

Hanna, S. et al., 2001. Uncertainties in predicted ozone concentrations due to input uncertainties for the UAM-V photochemical grid model applied to the July 1995 OTAGdomain. *Atmos. Environ,* 35(5), pp. 891-903.

Han, S. et al., 2011. Analysis of the Relationship between O3, NO and NO2 in Tianjin, China. *Aerosol Air Qual. Res.,* Volume 11, pp. 128-139.

Han, S. et al., 2009. Impact of nocturnal planetary boundary layer on air pollutants: measurements from a 250 m tower over Tianjin, China. *J Hazard Mater.,* Volume 162, pp. 264-269.

Han, S. et al., 2013. Differences in ozone photochemical characteristics between the megacity Tianjin and its rural surroundings. *Atmos. Environ.,* Volume 79, pp. 209-216.

Harley, R. A., Sawyer, R. F. & Milford, J. B., 1997. Updated photochemical modeling for California's South Coast Air Basin: comparison of chemical mechanism and motor vehicle emission inventories. *Environmental Science and Technology,* Volume 31, pp. 2829-2839.

Hart, J. E. et al., 2011. Long-term ambient multipollutant exposures and mortality. *American Journal of Respiratory and Critical Care Medicine,* Volume 183, pp. 73-78.

Henze, D., Hakami, A. & Seinfeld, J. H., 2007. Development of the adjoint of GEOS-Chem. *Atmos.Chem. Phys,* Volume 7, p. 2413–2433.

Hill, J. et al., 2009. Climate change and health costs of air emissions from biofuels and gasoline. *Proc. Natl. Acad. Sci.,* Volume 106, p. 2077–2082.

Ho, K. F. et al., 2006. Variability of organic and elemental carbon, water soluble organic carbon, and isotopes in Hong Kong. *Atmospheric Chemistry and Physics,* 6(12), pp. 4569-4579.

Huang, K. et al., 2013. Impact assessment of biomass burning on air quality in Southeast and East Asia during BASE-ASIA. *Atmospheric Environment,* Volume 78, pp. 291-302.

Hu, Y., Odman, M. & Russell, A., 2009. Top-down analysis of the elemental carbon emissions inventory in the United States by inverse modeling using Community Multiscale Air Quality model with decoupled direct method (CMAQ-DDM).. *J. Geophys. Res. Atmos.,* 114(D14).

IARC, 2013. *Outdoor air pollution a leading environmental cause of deaths.* [Online] Available at: http://www.iarc.fr/en/media-centre/iarcnews/pdf/pr221_E.pdf [Accessed 1 6 2014].

Ito, K., De Leon, S. F. & M, L., 2005. Associations between ozone and daily mortality: analysis and meta-analysis. *Epidemiology,* Volume 16, pp. 446-457.

Jenkin, M. E. & Clemitshaw, K. C., 2000. Ozone and other secondary photochemical pollutants: chemical processes governing their formation in the planetary boundary layer. *Atmospheric Environment,* Volume 34, pp. 2499-2527.

Jerrett, M. et al., 2009. Long-term ozone exposure and mortality. *The New England Journal of Medicine,* Volume 360, pp. 1085-95.

Jimenez, P., Baldasano, J. & Dabdub, D., 2003. Comparison of photochemical mechanisms for air quality modeling. *Atmospheric Environment,* Volume 37, p. 4179–4194.

Jin, L. et al., 2008. Sensitivity analysis of ozone formation and transport for a central California air pollution episode. *Environ. Sci. Technol.,* Volume 42, p. 3683–3689.

Khodeir, M. et al., 2012. Source apportionment and elemental composition of PM 2.5 and PM 10 in Jeddah City, Saudi Arabia. *Atmospheric pollution research,* 3(3), p. 331.

Khoder, M. I., 2009. iurnal, seasonal and weekdays–weekends variations of ground level ozone concentrations in an urban area in greater Cairo. *Environ Monit Assess.,* Volume 149, pp. 349-362.

Kim, S., Cohan, D. & Byun, D. W., 2009. Contributions of inter- and intra-state emissions to ozone over Dallas-Fort Worth, Texas. *Civ. Eng. Environ. Syst.,* Volume 26, p. 103–116.

Kleinman, L. et al., 2002. Ozone production efficiency in an urban area. *Journal of Geophysical Research: Atmospheres,* 107(D23).

Koo, B., Dunker, A. & Yarwood, G., 2007. Implementing the decoupled direct method for sensitivity analysis in a particulate matter air quality model. *Environ. Sci. Technol.,* Volume 41, p. 2847–2854.

Lelieveld, J., Evans, J. S., Fnais, M. & Giannadaki, D., 2015. The contribution of outdoor air pollution sources to premature mortality on a global scale. *Nature,* Volume 525, pp. 367-371.

Lepeule, J., Laden, F., Dockery, D. & Schwartz, J., 2012. Chronic exposure to fine particles and mortality: An extended follow-up of the Harvard six cities study from 1974 to 2009. *Environmental Health Perspectives,* Volume 120, pp. 965-970.

Liao, K. J. et al., 2007. Sensitivities of ozone and fine particulate matter formation to emissions under the impact of potential future climate change. *Environ. Sci. Technol.,* Volume 41, p. 8355–8361.

Li, L. et al., 2011. Ozone sensitivity analysis with the MM5-CMAQ modeling system for Shanghai. *Journal of Environmental Sciences,* 23(7), p. 1150–1157.

Lim, J. & Turpin, B. J., 2002. Origins of primary and secondary organic aerosol in Atlanta: results of time-resolved measurements during the Atlanta supersite experiment. *Environmental Science and Technology,* 36(21), p. 4489–4496.

Lin, X., Trainer, M. & Liu, S. C., 1998. On the nonlinearity of the tropospheric ozone production. *Journal of Geophysical Research: Atmospheres,* 93(D12), pp. 15879-15888.

Lonati, G., Ozgen, S. & Giugliano, M., 2007. Primary and secondary carbonaceous species in PM2. 5 samples in Milan (Italy). *Atmospheric Environment,* 41(21), pp. 4599-4610.

Luecken, D. J., Phillips, S., Sarwar, G. & Jang, C., 2008. Effects of using the CB05 vs. SAPRC99 vs. CB4 chemical mechanism on model predictions: ozone and gas-phase photochemical precursor concentrations. *Atmospheric Environment,* 42(23), pp. 5805-5820.

Lu, K. D. et al., 2013. Missing OH source in a suburban environment near Beijing: observed and modelled OH and HO2 concentrations in summer 2006. *Atmos. Chem. Phys.,* Volume 13, p. 1057–1080.

Maghrabi, A., Alharbi, B. & Tapper, N., 2011. Impact of the March 2009 dust event in Saudi Arabia on aerosol optical properties, meteorological parameters, sky temperature and emissivity. *Atmospheric Environment,* Volume 45, pp. 2164-2173.

Malm, W. C. et al., 1994. Spatial and seasonal trends in particle concentration and optical extinction in the United States.. *Journal of Geophysical Research: Atmospheres,* 99(D1), pp. 1347-1370.

Mao, J. et al., 2010. Atmospheric oxidation capacity in the summer of Houston 2006: comparison with summer measurements in other metropolitan studies. *Atmos. Environ,* Volume 44, p. 4107–4115.

Mazzeo, N. & Venegas, L. a. C. H., 2005. Analysis of NO, NO2, O3 and NOx concentrations measured at a green area of Buenos Aires City during wintertime. *Atmos. Environ.,* Volume 39, p. 3055–3068.

Mcrae, G., Goodin, W. & Seinfeld, J. H., 1982. Development of a 2nd-generation mathematical model for urban air pollution 1. Model formulation. *Atmos. Environ.,* Volume 16, p. 679–696.

Mendoza-Dominguez, A. & Russell, A., 2000. Iterative inverse modeling and direct sensitivity analysis of a photochemical air quality model. *Environ. Sci. Technol.,* Volume 34, p. 4974–4981.

Meo, S. A. et al., 2013. Respiratory and general health complaints in subjects exposed to sandstorm at Riyadh, Saudi Arabia. *Pakistan Journal of Medical Sciences,* 29(2), p. 642.

Moore, G. & Londergan, R., 2001. Sampled monte carlo uncertainty analysis for photochemical grid models. *Atmospheric Environment,* Volume 35, p. 4863–4876.

Morawska, L. et al., 2002. Differences in airborne particle and gaseous concentrations in urban air between weekdays and weekends. *Atmospheric Environment,* Volume 36, p. 4375–4383.

Napelenok, S., Cohan, D., Hu, Y. & Russell, A. G., 2006. Decoupled direct 3D sensitivity analysis for particulate matter (DDM-3D/PM). *Atmospheric Environment,* 40(32), pp. 6112-6121.

Napelenok, S. L., Cohan, D. S., Odman, M. T. & Tonse, S., 2008. Extension and evaluation of sensitivity analysis capabilities in a photochemical model. *Environ. Model. Softw.,,* Volume 23, p. 994–999.

Napelenok, S. L. & D. S. Cohan, M. T. O. a. S. T., 2008. Extension and evaluation of sensitivity analysis capabilities in a photochemical model. *Environ. Model. Softw.,,* Volume 23, p. 994–999.

National Science Foundation, 2016. *UCAR Community Data Portal.* [Online] Available at: http://cdp.ucar.edu/

Notario, A. et al., 2012. Analysis of NO, NO2, NOx, O3 and oxidant (OX=O3+NO2) levels measured in a metropolitan area in the southwest of Iberian Peninsula. *Atmos. Res.,* Volume 104, pp. 217-226.

NRC, 2008. *Estimating Mortality Risk Reduction and Economic Benefits from Controlling Ozone Air Pollution,* Washington, DC: National Research Council (NRC) of the National Academies.

Office of Transportation and Air Quality, USEPA, 2008. *Average Annual Emissions and Fuel Consumption for Gasoline-Fueled Passenger Cars and Light Trucks,* s.l.: United States Environmental Protection Agency.

Pinder, R. W. et al., 2009. Efficient Probabilistic Estimates of Surface Ozone Concentration Using an Ensemble of Model Configurations and Direct Sensitivity Calculations. *Environ. Sci. Technol.,* 43(7), p. 2388–2393.

Porter, W. C. et al., 2014. nnual and weekly patterns of ozone and particulate matter in Jeddah, Saudi Arabia. *J Air Waste Manag Assoc.,* 64(7), pp. 817-826.

Pun, B. et al., 2008. Response of atmospheric particulate matter to changes in precursor emissions: a comparison of three air quality models. *Environ. Sci. Technol.,* Volume 42, pp. 831-837.

Querol, X. et al., 2004. Speciation and origin of PM10 and PM2.5 in Spain. *Aerosol Science,* Volume 35, p. 1151–1172.

Renaut, J. et al., 2009. The impacts of atmospheric composition on plants: a case study of ozone and poplar. *Mass Spectrometry Reviews,* Volume 28, pp. 495-516.

RTI International, 2015. *Emissions Estimation Protocol for Petroleum Refineries,* Research Triangle Park, NC 27709-2194: RTI International .

Rushdi, A. I. et al., 2013. Air quality and elemental enrichment factors of aerosol particulate matter in Riyadh City, Saudi Arabia. *Arab Journal of Geoscience,* Volume 6, pp. 585-599.

Rushdi, A. I. et al., 2013. Air quality and elemental enrichment factors of aerosol particulate matter in Riyadh City, Saudi Arabia. *Arabian Journal of Geosciences,* 6(2), pp. 585-599.

Saliba, N. A. & Massoud, R., 2010. A comparative review of PM levels, sources, and their likely fates in the Eastern Mediterranean Region. In: *In Urban Airborne Particulate Matter.* s.l.:Springer Berlin Heidelberg, pp. 3-17.

Sandu, A. et al., 1997. Benchmarking stiff ODE solvers for atmospheric chemistry problems II: Rosenbrock solvers. *Atmospheric Environment,* pp. 3459-3472.

Sarwar, G. et al., 2013. A comparison of atmospheric composition using the Carbon Bond and Regional Atmospheric Chemistry Mechanisms. *Atmospheric Chemistry and Physics,* 13(19), pp. 9695-9712.

Sarwar, G. et al., 2013. A comparison of atmospheric composition using the Carbon Bond and Regional Atmospheric Chemistry Mechanisms. *Atmos. Chem. Phys.,,* Volume 13, p. 9695–9712.

Sarwar, G. et al., 2008. Impact of an Updated Carbon Bond Mechanism on Predictions from the CMAQ Modeling System: Preliminary Assessment. *Journal of Applied Meteorology and Climatology,* Volume 47, pp. 3-14.

Saudi Geological Survey, 2016. *Spatial Data.* [Online] Available at: https://www.sgs.org.sa/English/Products/DigitalData/Pages/SpatialData.aspx

Seinfeld, J. H. & Pandi, S. N., 2006. *Atmospheric Chemistry and Physics.* s.l.:John Wiley & Sons, Inc.

Shahsavani, A. et al., 2012. Characterization of ionic composition of TSP and PM10 during the Middle Eastern Dust (MED) storms in Ahvaz, Iran. *Environmental Monitoring and Assessment,* Volume 184, p. 6683–6692.

Shareef, M. M., Husain, T. & Badr, A., 2016. *Identifying appropriate chemical mechanisms for photochemical air quality modeling in arid regions.* New Orleans, Air & Waste Management Association.

Shen, Z. et al., 2009. Ionic composition of TSP and PM2.5 during dust storms and air pollution episodes at Xi'an, China. *Atmospheric Environment,* Volume 43, p. 2911–2918.

Sillman, S. & He, D., 2002. Some theoretical results concerning O3-NOx-VOC chemistry and NOx-VOC indicators. *J. Geophys. Res. Atmos,* p. 107.

Simon, H. et al., 2013. A Direct sensitivity approach to predict hourly ozone resulting from compliance with the National Ambient Air Quality Standard. *Environ. Sci. Technol,* Volume 47, p. 2304–2313.

Stockwell, W. R., 1986. A homogenous gas phase mechanism for use in a regional acid deposition model. *Atmospheric Environment,* Volume 20, pp. 1615-1632.

Stockwell, W. R., Kirchner, F., Kuhn, M. & Seefeld, S., 1997. A new mechanism for regional atmospheric chemistry modeling. *ournal of geophysical research: Atmospheres,* 102(D22), pp. 25847-25879.

Stockwell, W. R., Middleton, P. & and Chang, J. S., 1990. The Second Generation Regional Acid Deposition Model Chemical Mechanism for Regional Air Quality Modeling. *J. Geophys.Res., ,* p. 16343–16367.

Sulaiman, N., Abdullah, M. & Chieu, P. L. P., 2005. Concentration and composition of PM10 in outdoor and indoor air in industrial area of Balakong Selangor, Malaysia. *Sains Malaysiana,* Volume 34, pp. 43-47.

Tagaris, E. et al., 2010. Sensitivity of Air Pollution-Induced Premature Mortality to Precursor Emissions under the Influence of Climate Change. *Int. J. Environ. Res. Public Health,* Volume 7, p. 2222–2237.

The institute for the Environment - The University of North Carolina at Chapel Hill, 2015. *SMOKE v3.6.5 User's Manual.* [Online] Available at: https://www.cmascenter.org/smoke/documentation/3.6.5/html/

The Research Division, California Air Resources Board, 2003. *The ozone weekend effect in California,* Sacramento: California Air Resources Board.

The Weather Research and Forecasting Model, 2016. [Online] Available at: http://www.wrf-model.org

Tian, D. et al., 2010. Uncertainty analysis of ozone formation and response to emission controls using higher-order sensitivities. *J. Air Waste Manage. Assoc.,* Volume 60, p. 797–804.

Tonnesen, G. S. & Luecken, D., 2001. Intercomparison of photochemical mechanisms using response surfaces and process analysis. In: Gryning, S.-E., Schiermeier, F.A. (Eds.),. In: *Air Pollution and its Application.* s.l.:Kluwer, New York.

Umann, B. et al., 2005. Interaction of mineral dust with gas phase nitric acid and sulfur dioxide during the MINATROC II field campaign: First estimate of the uptake coefficient. *J. Geophys.,* 110(D22306).

Underwood, G. M. et al., 2001. Heterogeneous reactions of NO2 and HNO3 on oxides and mineral dust: A combined laboratory and modeling study. *Journal of Geophysical Research,* Volume 106, pp. 18055-18066.

US Environmental Protection Agency, 1995. *AP 42 Section 11.6 Portland Cement Manufacturing,* s.l.: USEPA.

US EPA, 2006. *Technical Support Document for the proposed PM NAAQS Rule: Response Surface Modeling,* s.l.: s.n.

Vautard, R., Honore, C., Beekmann, M. & Rouil, L., 2005. Simulation of ozone during the August 2003 heat wave and emission control scenarios. *Atmos. Environ.,* Volume 39, pp. 2957-2967.

Wang, J. et al., 2013. Contamination characteristics and possible sources of PM10 and PM2.5 in different functional areas of Shanghai, China.. *Atmospheric Environment,* Volume 68, pp. 221-229.

Wang, L. et al., 2012. Understanding haze pollution over the southern Hebei area of China using the CMAQ model. *Atmos. Environ,* Volume 56, pp. 69-79.

Wang, Y. et al., 2005. The ion chemistry and the source of PM2.5 aerosol in Beijing. *Atmospheric Environment,* Volume 39, pp. 3771-3784.

Whitten, G. Z. et al., 2010. A new condensed toluene mechanism for carbon bond: CB05-TU. *Atmos. Environ,* Volume 44, pp. 5346-5355.

Xiao, H. & Liu, C., 2004. Chemical characteristics of water soluble components in TSP over Guiyang, SW China. *Atmospheric Environment,* Volume 38, pp. 6297-6306.

Xiao, X., Cohan, D., Byun, D. & Ngan, F., 2010. Highly nonlinear ozone formation in the Houston region and implications for emission controls. *J. Geophys. Res. Atmos.,* 115(D15).

Xing, J. et al., 2011. Nonlinear response of ozone to precursor emission changes in China: A modeling study using response surface methodology.. *Atmos. Chem. Phys.,* Volume 11, p. 5027–5044.

Yamama Cement Company, 2012. *Cement Statistic - Year 2012,* Riyadh : Yamama Cement Company.

Yang, Y. J., Wilkinson, J. G. & Russell, A., 1997. Fast, direct sensitivity analysis of multidimensional photochemical models. *Environ. Sci. Technol.,* Volume 31, p. 2859–2868.

Yao, X. et al., 2002. The water-soluble ionic composition of PM2.5 in Shanghai and Beijing, China. *Atmospheric Environment ,* Volume 36, pp. 4223-4234.

Yarwood, G. et al., 2013. A method to represent ozone response to large changes in precursor emissions using high-order sensitivity analysis in photochemical models. *Geosci. Model Dev,* Volume 6, pp. 1601-1608.

Yarwood, G., Rao, S., Yocke, M. & Whitten, G., 2005. *Updates to the Carbon Bond Chemical Mechanism: CB05. Final report to the US EPA, RT-0400675.* [Online] Available at: http://www.camx.com http://www.camx.com/publ/pdfs/cb05final report 120805.aspx
[Accessed 9 9 2016].

Yu, S., Dennis, R. L., Bhave, P. V. & and Eder, B. K., 2004. Primary and secondary organic aerosols over the United States: estimates on the basis of observed organic carbon (OC) and elemental carbon (EC), and air quality modeled primary OC/EC ratios. *Atmos. Environ,* 38(31).

Zhang, B. et al., 2015. Heterogeneous chemistry: a mechanism missing in current models to explain secondary inorganic aerosol formation during the January 2013 haze episode in North China. *Atmos. Chem. Phys.,* Volume 15, p. 2031–2049.

Zhang, W. & Russell, A., 2010. *The Decoupled Direct Method for Higher-Order Sensitivity Analysis for Particulate Matter in Multidimensional Air Quality Models.* Atlanta, GA, USA, s.n., pp. 17-21.

Zhang, Y. et al., 2014. Impacts of updated emission inventories on source apportionment of fine particle and ozone over the southeastern U.S.. *Atmospheric Environment,* Volume 88, pp. 133-154.

Zimmermann, J. & and Poppe, D., 1996. A supplement for the RADM2 chemical mechanism: The photooxidation of isoprene. *Atmospheric Environment,* pp. 1255-1269.